Title
A Theoretical and Numerical Study of Nanoscale Heat Transfer

Author
Ghafari Zeydabadi, Amin

Publication Date
2020

A Theoretical and Numerical Study of Nanoscale Heat Transfer

by

Amin Ghafari Zeydabadi

A dissertation submitted in partial satisfaction of the

requirements for the degree of

Doctor of Philosophy

in

Mechanical Engineering

in the

Graduate Division

of the

University of California, Berkeley

Committee in charge:

Professor David B. Bogy, Chair
Professor Tarek I. Zohdi
Professor Lin Lin

Fall 2020

A Theoretical and Numerical Study of Nanoscale Heat Transfer

Abstract

A Theoretical and Numerical Study of Nanoscale Heat Transfer

by

Amin Ghafari Zeydabadi

Doctor of Philosophy in Mechanical Engineering

University of California, Berkeley

Professor David B. Bogy, Chair

In order to continue the progress of nanotechnology in producing effective and efficient mechanical, electrical, and optical nanostructure devices, the physics of the devices in micro and nanoscale need to be understood and accurately modeled. For instance, the demand for high areal density data storage devices such as hard disk drives (HDDs) has led to heat-assisted magnetic recording (HAMR) and microwave-assisted magnetic recording (MAMR) technologies. These technologies require layered nanostructures with thicknesses of a few nanometers and a high temperature difference across the layers. These technologies introduce thermo-mechanical design challenges since the nanoscale heat transfer mechanics do not follow the classical heat transfer theories. In this work, the mechanisms of heat transfer in the nanoscale are studied.

A typical nanostructure is composed of several conductive and thin insulating layers (a few microns to a few nanometers) with a temperature difference between the layers where some insulating layers maintain the temperature gradient in such small spacings. In these structures, the dominant heat transfer mechanisms are radiation due to high temperature gradient and phonon conduction due to thin conductive layers. First, we review the fundamentals of electromagnetism and lattice vibrations and derive the classical heat transfer theories, and discuss the assumptions that lead to them. We show that the classical theories do not consider the wave nature of the heat transfer mechanisms (heat carriers) and are derived based on equilibrium thermodynamics. These assumptions make the obtained results inapplicable to our problems. Next, we study the recent theories and methods used to solve steady-state nanoscale heat transfer problems, and we further develop more accurate models of calculations.

In this work, we study the mechanisms of heat transfer in nanostructures and present simulations for the thermal analysis of various multilayered structures. We show how the radiative and phonon conduction heat fluxes across a nanoscale vacuum gap vary as a function of the gap spacing, and focus on the problems with large heat flux across nanostructures. Next,

we consider the effect of the interference of the heat carriers, due to their wave nature, on radiation and phonon conduction. The heat transfer coefficient (HTC) for various structures used in the current HDD technology is characterized by different temperature differences and conditions. The presented results are also used in collaboration with other researchers in simulations of HDI of HAMR HDDs.

Next, the presented algorithms are used to simulate radiation in multilayered structures with absorbing materials, where the speed of propagation for absorbing materials is based on a recent model in literature that predicts the depth-dependent speed of electromagnet waves inside materials. We also present a novel way to describe the distribution of the thermal emission inside a multilayered structure using one distribution function instead of using multiple distributions for layers with different temperatures, which we call the unified field. This model is more accurate than the models in the preceding chapters at predicting the HTC for the phonon conduction in materials under some conditions.

To my beloved parents and siblings.

Acknowledgments

The past six years at Berkeley has been a transformative period in my life. UC Berkeley community made me a wiser, stronger, and more capable person. There have been many people who helped me in developing my research interests and character. Here I would like to recognize and thank them.

First and foremost, I want to immensely thank my adviser, Prof. David B. Bogy, for providing me with the opportunity to work and learn in his research group, and for supporting and guiding me throughout my doctoral study at UC Berkeley. I am grateful for his trust in my abilities, and for empowering me even at times I was doubting myself. I genuinely appreciate his openness to research ideas, keen eyes, and tactful critiques in order to realize the best course of action to take in completing a research project. I have learned a lot from our interesting and joy-provoking discussions about research, academic life, and personal life. He is simply the best adviser that anyone can wish for.

I would like to thank Dr. Bair V. Budaev for his unwavering mentorship and guidance throughout my research studies. My discussions with him have been the most fruitful ones in pushing and overcoming my research challenges. His mastery in the field and his insight on my work have contributed significantly to shaping this dissertation. He has always been open to providing his honest feedback on my thought processes and research work. He always made me aware of my blind spots in research, and for which I am very thankful.

I would like to thank Prof. Tarek Zhodi and Prof. Lin Lin for serving on my qualifying exam committee and reviewing my dissertation. I also thank Prof. David Steigmann and Prof. Van Carey for serving on my qualifying exam committee. Taking classes in Berkeley has been enjoyable, challenging, and instructive, for which I am very thankful to all my teachers, including but not limited to Profs. David Steigmann, Per-Olf Persson, Martin White, Panayiotis Papadopoulos.

I want to thank all my colleagues and labmates at Computer Mechanics Laboratory (CML) for sharing their knowledge and helping me in any way they could. My research has benefited from my informative discussions with Tholfaqar "Dolf" Mardan, Yung-Kan Chan, Alejandro Rodriguez Mendez, Soroush Sarabi, Yuan Ma, Haoyu Wu, Siddhesh Sakhalkar, Qilong Cheng, Yuying Wu. I was fortunate to work with Yuan Ma on several research projects, and I have learned and enjoyed discussing ideas with Yuan, writing papers together, going to conferences together. For the last two years, Siddhesh, Qilong, and I have worked on research projects as a team with Qilong working on experiments, Siddhesh doing the thermo-mechanical simulations, and me working on the heat transfer models and computations. This teamwork has been a unique experience, and I have enjoyed working with Siddhesh and Qilong.

I am grateful for the friends I made in Berkeley. They made this experience particularly meaningful and fun. In particular, I want to thank Behrooz Shahsavari and Sayna Ebrahimi for their continued support and encouragement. At the time of uncertainty and distress, I have always resorted to them for their advice. They have treated me like a family, and they

are like siblings to me. I also immensely thank Shahin Tabrizi, a father figure to me, for his selfless mentorship, which significantly improved my academic and personal life.

Finally, this accomplishment would not be possible without the unconditional love, support, and encouragement of my family. My parents have never had the chance to pursue their dreams as students. However, their endless encouragement and support always fueled my passion and resilience in pursuing my dreams. Their kind attitude and care for the family and me have taught me how to be selfless while aiming and striving for the best. Growing up, my beloved brother and sister have always been there for me, and they taught me how to be a better and kinder person.

Contents

List of Figures

List of Tables

Acronyms

DOS	density of states. 15
EM	electromagnetic. 1, 2, 4, 5, 9, 10, 12, 13, 16, 17, 19, 26, 27, 30, 33, 35, 46, 51, 57, 58, 59, 72
HAMR	heat-assisted magnetic recording. 4, 7, 8, 33, 79, 80
HDD	hard disk drive. 4, 6, 7, 52, 80
HDI	head-disk interface. 6, 7, 8, 80
HTC	heat transfer coefficient. 3, 4, 24, 26, 27, 28, 47, 49, 52, 53, 54, 69, 70, 72, 74, 76, 79, 80
NFT	near field transducer. 8
PMR	perpendicular magnetic recording. 6, 7
TFC	thermal flying-height control. 6
vdW	van der Waals. 46, 47
ZPE	zero-point energy. 12, 13

Chapter 1

Introduction

1.1 Introduction

Nanoscale heat transfer has been of high interest over the past few decades, and research on this topic has significantly increased. The experimental and theoretical advancements in nanoscale heat transfer enabled thermal management and design of nanostructures used in optical, electrical, and electromagnetic (EM) technologies [1]. Experiments have shown that the heat transfer in nanoscale is significantly different from classical predictions [1–15]. The continuous theoretical efforts in predicting this behavior have revealed that radiation and conduction, two primary modes of heat transfer in nanostructures, fundamentally change as the dimensions of the structures get smaller [16–28] and different physical interpretations are required to study them.

The classical law of radiation, known as the Stefan-Boltzmann law [29], states that the emitted heat flux per unit area from the surface of a body with temperature T is

$$Q = \sigma T^4 \quad \left[\mathrm{J} \cdot \mathrm{s}^{-1} \cdot \mathrm{m}^{-2}\right], \tag{1.1}$$

where $\sigma = 5.67 \times 10^{-8}\ \mathrm{W} \cdot \mathrm{m}^{-2} \cdot \mathrm{K}^{-4}$ is the Stefan-Boltzmann constant. Using this the heat flux between two surfaces with temperatures T_A and T_B which are facing each other is

$$Q_{\mathrm{net}} = Q_{A \to B} - Q_{B \to A} = \sigma (T_A^4 - T_B^4) \quad \left[\mathrm{J} \cdot \mathrm{s}^{-1} \cdot \mathrm{m}^{-2}\right]. \tag{1.2}$$

Later, Planck proposed that EM waves consist of bundles or packets of energy known as photons and developed the concept of black body radiation in order to describe the radiative heat flux from the surfaces of materials [30]. This is known as Planck's law of radiation, which reproduced the Stefan-Boltzmann law. This work led to the development of quantum theory [31, 32].

The result produced by (1.1) is a reasonable prediction at macroscale. As this equation shows, the predicted radiation between materials does not depend on the length scale. This prediction comes from not taking into consideration the wave nature of EM waves with respect to the dimensions of the problem, which are responsible for radiation. It has been observed that if the length scale of the heat transfer problem is of the same order as the EM waves wavelength (a few microns), then the heat flux is enhanced beyond the predictions of (1.2), as Hargreaves observed in his paper on radiative heat transfer between two closely-spaced metal plates [5]. After this, several improvements have been suggested to overcome this inconsistency, as briefly reviewed in the following chapters.

On the other hand, the classical conduction heat transfer theory is described by Fourier's law, which depends on the thermal conductivity of materials and the temperature gradient.

$$Q = -k\nabla T, \tag{1.3}$$

where k is the thermal conductivity, and ∇T is the temperature gradient. This mode of heat transfer in solids is due to free electrons and vibration of particles. The free electrons only exist in electrical conductors, while the vibration of particles exists in all materials and are the primary heat transfer medium for thermally conductive crystals such as diamond. The vibrational energy propagating in materials produces waves with the wavelength of a few nanometers; hence, in macroscale the wave nature of this mode of heat transfer is not important, and equation (1.3) predicts the heat conduction correctly. However, as for EM waves, if the length scale of the problem is of the order of a few nanometers the wave nature of the vibrations affects the heat transfer [10, 33]. Some of the improvements applied to EM waves are also applicable to vibrational conduction, and they are discussed in the following chapters.

When these modifications are included, the obtained formulations for radiation and conduction become relatively complex. This is because the distributions of heat carriers in two closely spaced bodies with different temperatures depend on both temperatures and the heat flux between them. The result is a system of nonlinear and implicit integral equations to solve for a defined geometry. In the rare situations of small temperature differences between bodies, it has been shown that the formulation can be linearized to a system of linear and explicit equations [34]. However, in most cases, the temperature difference precludes the linearization. One of the main topics of the present work is concerned with the development of fast and efficient computational models and algorithms for solving these nanoscale problems.

1.2 Problem Statement

Many of the structures used in nanotechnology are composed of multilayered plates. These layered structures have a thickness ranging from a few nanometers to a few microns. The temperatures between these thin layers can be quite different. As a result of the thinness of the layers and the temperature difference, they present thermal management challenges. In addition, these multilayered structures can be separated by only a few nanometers, which makes the physics of the heat transfer problem challenging to understand. Here, we investigate the thermal behavior of such structures using the most recent physical models and computational algorithms.

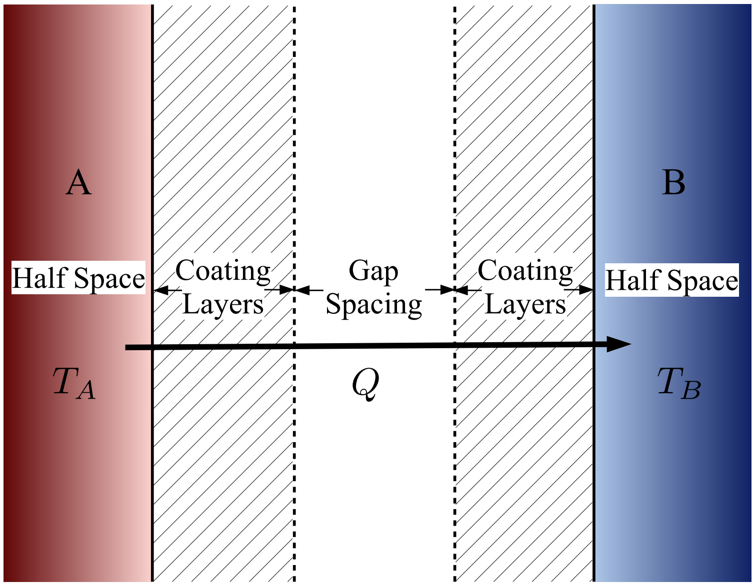

Figure 1.1: Two half-spaces separated by a series of material coating layers and vacuum gaps

We consider first a simple multilayered structure, which is composed of two half-spaces with different temperatures, which are acting as a heat source and a heat sink. This can represent bodies that are relatively large compared to the thickness of the layers of the multilayered structure or bodies that are in contact with a heat source. These two half-spaces are connected through a number of thin layers of materials or vacuum gaps that are too thin to supply significant heat. Hence, the physics of the problem is composed of two half-spaces with temperatures that influence the heat generation and the distributions of heat carriers in both half-spaces. Moreover, the thin layers and gaps affect the way the energy transfers through the layers into the other domain. One such example of a multilayered structure is shown in Fig. 1.1.

One of the critical parameters in the structure is the spacing between the half-spaces. The important parameter that captures the thermal behavior of the structures under various spacings is the heat transfer coefficient (HTC). Hence, we are interested in determining this parameter under multiple conditions, the geometry of the multilayered structure, and the range of the gap spacing. Two types of system conditions are considered; the temperatures of the half-spaces (T_A for the left half-space and T_B for the right half-space) and the heat flux between the half-spaces (Q). Based on the formulation presented in chapter 4, we assume two of these three parameters are known and seek to determine the third parameter and hence find the HTC.

So we divide the problem into two cases: 1. when we know the temperatures T_A and T_B and want to determine the heat flux, 2. and when we know the heat flux and the temperature of one half-space (e.g. when the half-space is in contact with the ambient environment and its temperature is the same as the ambient temperature). This is necessary in order to predict the HTC corresponding to different experimental setups, and to compare it with the experimental results.

1.3 Contribution per Chapter

In this dissertation, the work is separated into two parts. The first part develops the formulation and solves the radiation in nanoscale. The second part applies the developed theory to phonon conduction heat transfer.

- **Chapter 2:** Among various applications of nanoscale heat transfer theories discussed and developed in this work, we are interested in the heat transfer problems in hard disk drive (HDD) technologies such as heat-assisted magnetic recording (HAMR) [35–37]. In this chapter the current HDD technology and the corresponding thermal problems in nanoscale are briefly reviewed.

- **Chapter 3:** We outline the underlying physics of radiation and its heat carriers, which can be viewed as EM waves propagating in media or quantized packets of energy known as photons. Planck's law of radiation in equilibrium is reviewed and the conditions under which this model is valid are investigated. We discuss how an extension of this model, known as the Extended Planck's law, pertains to the thermal analyses of systems with small or large steady state heat flux in materials.

- **Chapter 4:** The thermal radiation heat fluxes across a multilayered structure in the presence of small and large heat fluxes are computed. It is shown that, depending on the gap length scale of the problem, the radiative heat flux can be enhanced with respect to what the classical predict predicts.

  Next, we discuss how the wave nature of these heat carriers affects the heat transfer process in nanoscale, which is different from macroscale heat transfer phenomena. The waves interference effect are considered in the physics of the radiation problem and the simulation results are presented.

- **Chapter 5:** We study the conduction due to vibrational waves or the quantized packets of energy known as phonons, similar to photons. Phonons are introduced using the Debye model, which is a modified interpretation of Planck's law. We compare this to the classical models of conduction and investigate the applicability of this model for heat transfer problems. First we consider the phonons as heat carriers for conduction for cases when there is no net heat flux. The extension of this model for heat flux under steady state conditions for nanoscale problems is discussed. We then present numerical results for phonon conduction heat flux in nanoscale.

  Then, the interference of the thermally excited waves generated in two material bodies are considered in the calculation of heat flux in a multilayered structure. We use this method to calculate the HTC corresponding to any given structure and boundary conditions and tabulate the result for thermo-mechanical simulation of more complex systems. The calculations are compared to recent experimental work on hard disk drive components.

- **Chapter 6:** In this chapter we compute the thermal radiation from real materials, i.e. absorbing materials, where the speed of EM waves is a function of the frequency and the depth at which they are generated inside the material. The results are compared with the grey body interpretation for some materials.
- **Chapter 7:** The thermal radiation and conduction are described using a unified field. The unified field for radiation is used to determine the thermal radiation for structures containing absorbing material. We then apply the concept of the unified field to phonon conduction. This reveals that the phonon conduction across a nanoscale gap is only important when the spacing is less than about 4nm.
- **Chapter 8:** A summary of the dissertation and potential future research works are presented.

Chapter 2

Heat Transfer in Hard Disk Drives

2.1 HDD Technology

A modern HDD, as shown in Fig. 2.1a, is composed of several disks assembled on a spindle that typically rotates at speeds of 3600-7200 rpm, an actuator arm to which a suspension is attached, which supports a head that contains the read-write elements and sensors. The read-write process happens at the trailing tip of the head where the distance between the head and the disk varies between a few nanometers to contact when the disk is rotating; this is known as the head-disk interface (HDI), Fig. 2.1b. HDD technology currently utilizes perpendicular magnetic recording (PMR) [38] for the recording process.

The PMR head floats above the disk at a closest distance of 2-20nm. This distance is also known as the 'flyheight'. The disk is a multilayered structure with a magnetic layer on which the small data bits are recorded. The read-write coils are placed at the tip of the head, while the actuator control system moves the head around and navigates the disk area in order to read-write data on bit locations while the disk is rotating. The read-write process, which is the process of switching the magnetic moment of the bits up and down, occurs in about 1ns. The rotation of the disk pressurizes the air between the head and disk and helps maintain the required distance between them. The block that contains the head structure is also known as a "slider". The pressurized air mechanics is known as the airbearing system, which is a very important aspect of a successful HDI design. One important element for a stable HDI is the shape and structure of the slider's surface facing the disk (airbearing design).

Increasing the areal density requires smaller bit sizes and consequently smaller head components. Moreover, the read-write elements need to be closer to the disk so that their magnetic field only affects the area of the target bit location. But bringing the entire slider closer to the disk causes an air bearing instability of the HDI. To address this issue, another element has been integrated into the head, which is called thermal flying-height control (TFC). The TFC component utilizes a heater element, shown in Fig. 2.1b, that relies on thermal expansion to bring the read-write element closer to the disk (<5nm) for recording on smaller bits size while keeping the rest of the head at a distance greater than 20nm.

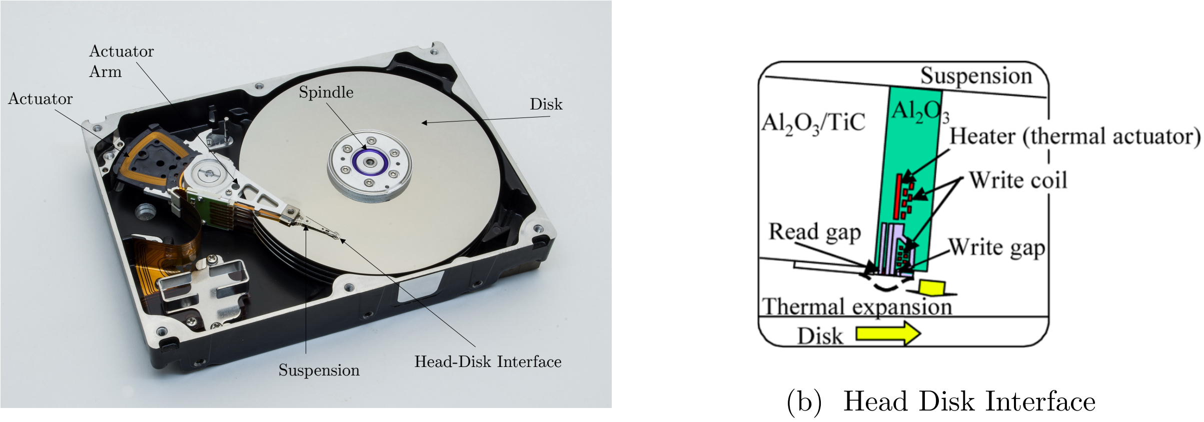

(a) HDD Components

(b) Head Disk Interface

Figure 2.1: Structure of the modern HDD

While the PMR systems with some modifications have been utilized in the continuous growth of the areal density, they have limitations that hinder them from continuing the same areal density growth rate. This is essentially due to the fact that as the bit size is reduced below a certain threshold the data bits become thermally unstable because the size approaches the thermal energy fluctuation limit for the disk material, known as the superparamagnetic limit [39].

In order to have smaller bits without thermal instability of the bit, one solution is to use a material with higher coercivity for the magnetic layer on the disk. Coercivity is a measure of the ability of a ferromagnetic material to withstand an external magnetic field without becoming demagnetized. A material with higher coercivity is thermally stable at room temperature for smaller bit sizes. Although this is a desirable property, it makes the data writing more difficult as the normal magnetic field of a write element is not able to switch the bit magnetic moment. The key idea is to heat up the magnetic media to some critical temperature (known as the Curie temperature) so that the coercivity of the material drops below a threshold where the write element can switch the magnetic moment of the bits and record the data.

In HAMR technology this issue is resolved by temporarily and locally heating the targeted bits, recording the data (switching the bits magnet moment), and letting the bits cool abruptly so the data can be ‘frozen in’ stably. For this purpose, a laser beam is applied in front of the magnetic writer. The size of the heated spot is confined to the tiny volume of the bit size in order to avoid corrupting the adjacent bits. A schematic of a HAMR HDI concept is shown in Fig. 2.2 [1] from [40].

---

[1] License is obtained from Springer Nature and Copyright Clearance Center.

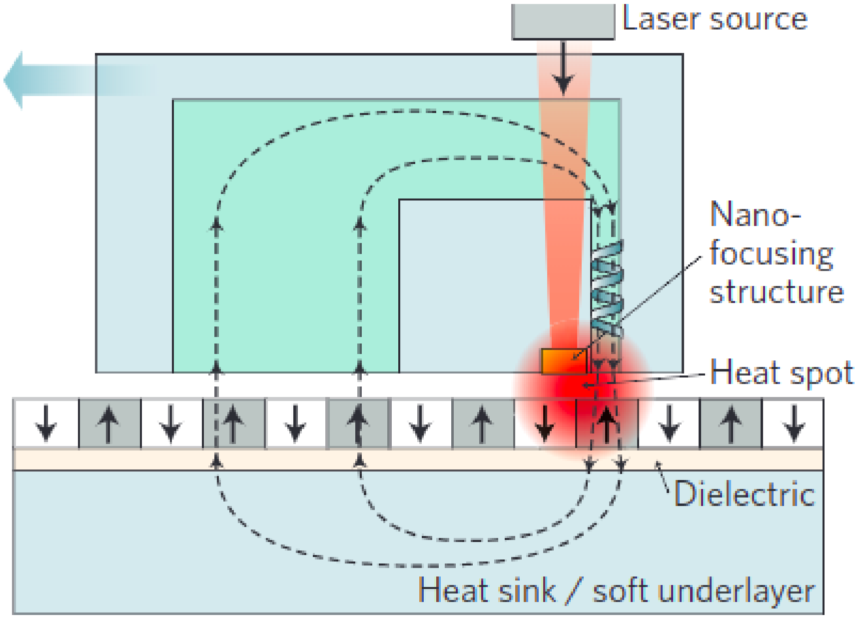

Figure 2.2: The HAMR HDI schematic [40]

2.2 Challenges in HAMR

In HAMR Technology a waveguide is embedded in the head. The waveguide transmits laser beams and delivers a focused optical beam of energy that is required for the small bit size. However, the bit size is much smaller than the diffraction limits of optical beams. So the optical beam is delivered by the waveguide to a metallic nano-antenna known as a near field transducer (NFT) located at the surface of the head facing the disk. The delivered energy excites the NFT, and then the NFT generates a very strong field intensity over a spot size of a few tens of nanometers on the disk.

Part of the energy delivered through the waveguide to the NFT is dissipated in those structures and the surrounding head. The absorbed energy increases the temperature of the NFT, deforms it, and changes its structure, such that the NFT may no longer be functional for the recording task. This is one of the reported failure modes of HAMR HDIs [41].

The absorbed energy by the disk increases the temperature of the disk to its Curie temperature, at least 500°C, which leads to some deformation of the disk layers. This effect is exacerbated since the thermal expansions of the various interior layers may be different. Moreover the disk lubricant can be evaporated, depleted, and decomposed due to the high temperature. The deformation of the NFT also affects how the waveguide delivers the light to it as the material properties of NFT may change.

Here, the goal is to study the heat transfer problems that arises in the HDI components by taking into consideration its multilayered nanostructure, variable spacing between the head and the disk, and the presence of high temperature gradients.

Chapter 3

Radiation in Zero and Steady Net Heat Flux Systems

3.1 Planck's Law

Planck's law describes the spectrum of EM radiation from a black body in thermal equilibrium with zero net heat flux. The main part of this work is based on the generalization of Planck's law to systems with steady net heat flux. In order to make this generalization more transparent, we outline the origin of Planck's law.

3.1.1 Classical Electromagnetism

All materials are made of elementary particles most of which carry electric charges, which generate EM fields. A stationary particle carrying a charge q, generates an electric field

$$\mathbf{E}(\mathbf{r}) = \frac{1}{4\pi\varepsilon_0}\frac{q}{|\mathbf{r}|^2}\mathbf{e}_{\mathbf{r}}, \tag{3.1}$$

where $\mathbf{r}$ is a vector from the position of the particle to the point where the electric field is measured, $\varepsilon_0 = 8.85418782 \times 10^{-12}\ \mathrm{F} \cdot \mathrm{m}^{-1}$ is the permittivity of vacuum, and $\mathbf{e}_{\mathbf{r}} = \dfrac{\mathbf{r}}{|\mathbf{r}|}$. A moving charge generates a more complex electric field,

$$\mathbf{E}(\mathbf{r}') = \frac{q}{4\pi\varepsilon_0}\left[\frac{1}{|\mathbf{r}'|^2}\mathbf{e}_{\mathbf{r}'} + \frac{|\mathbf{r}'|}{c}\frac{d}{dt}\left(\frac{\mathbf{e}_{\mathbf{r}'}}{|\mathbf{r}'|^2}\right) + \frac{1}{c^2}\frac{d^2}{dt^2}\left(\mathbf{e}_{\mathbf{r}'}\right)\right], \tag{3.2}$$

where $\mathbf{r}'$ is the vector from the particle's position at the time when the field was generated to the point where the electric field is measured, $\mathbf{e}_{\mathbf{r}'} = \dfrac{\mathbf{r}'}{|\mathbf{r}'|}$, and c is the speed of light in vacuum. The last term in (3.2) decays slower than $1/|\mathbf{r}'|^2$ as $|\mathbf{r}'| \to \infty$ and it makes possible the long-distance propagation of EM waves.

Additionally, a moving charge produces a magnetic field **B** at $\mathbf{r}'$ that is perpendicular to the direction of its motion and to its electric field **E** at $\mathbf{r}'$, [42] Vol. 1, Eq. (28.3).

$$\mathbf{B}(\mathbf{r}') = -\mathbf{e}_{\mathbf{r}'} \times \frac{\mathbf{E}(\mathbf{r}')}{c}. \tag{3.3}$$

From (3.2) and (3.3) it is clear that an accelerating charge generates time-varying electric and magnetic fields, which form EM waves.

The power passing through a shell G that surrounds the source is determined by

$$P(r) = \frac{1}{\mu} \oint_{\partial G} (\mathbf{E} \times \mathbf{B}) \cdot d\mathbf{a}, \tag{3.4}$$

where $d\mathbf{a}$ is an outward-oriented surface element of the shell, and μ is the permeability of the medium. The integration in (3.4) with **E** and **B** from (3.2) and (3.3) shows that only the contribution of the third term does not vanish as $|\mathbf{r}| \to \infty$. The third term appears only when the charged particles accelerate. This leads to EM radiation.

It is clear from (3.2) and (3.4) that a greater acceleration leads to a greater radiative power. On the other hand, according to thermodynamics, higher speeds of charged particles of a material correspond to a higher temperature in the material. Hence, a higher temperature causes more radiation.

Since EM waves can propagate in vacuum, the radiated EM field from the material can propagate into the surroundings for long distances. As an example, the radiation from the Sun reaches the Earth through a mostly vacuum space. The EM field radiated by molecules of one body exert forces on molecules of another body. These forces affect the motion of molecules in the other body, resulting in the change of its temperature.

Two separated material bodies A and B radiate EM fields. The radiative field from A pushes the charges in B and causes them to accelerate while the field from B pushes charges in A. So bodies A and B exchange thermal energy. Assume A's temperature is higher than that in B. This causes B to receive more radiation from A than it radiates to A; consequently, there is a net radiative energy flux from A with a higher temperature to B with a lower temperature. This intuitively explains heat transfer due to radiation.

In many studies of radiation, the coupling of different materials through EM radiation is neglected. If material bodies are separated by a sufficiently large distance, the field radiated from A does not significantly affect that radiation from B, which justifies calculations of the heat flux without consideration of the coupling effect. However, when bodies are closer than the dominant wavelength of radiation (around 10μm at 298 K), the radiation from them cannot be considered independently. This subject will be discussed in more detail in the following sections.

An EM field is composed of an electric field **E** and a magnetic field **B**. These fields exert a force on any particle with a charge q

$$\mathbf{F} = q(\mathbf{E} + \mathbf{v} \times \mathbf{B}), \tag{3.5}$$

where $\mathbf{v}$ is velocity of the charge.

In addition to $\mathbf{E}$ and $\mathbf{B}$, the electric displacement field $\mathbf{D}$ and magnetic intensity field $\mathbf{H}$ are defined. In materials, in addition to free charges, there are bound charges. An electric field causes displacements of the bound charges, which induce an electric field $\mathbf{P}$, which determines the electric displacement field $\mathbf{D} = \varepsilon_0\mathbf{E} + \mathbf{P}$. Similarly, the magnetic field $\mathbf{B}$ induces a magnetized field $\mathbf{M}$, which defines the magnetic intensity by $\mathbf{H} = \frac{\mathbf{B}}{\mu_0} - \mathbf{M}$. For uniform isotropic linear media $\mathbf{D} = \varepsilon\mathbf{E}$ and $\mathbf{B} = \mu\mathbf{H}$, where ε and μ are the permittivity and permeability of the material, respectively.

The electric and magnetic fields in materials are related through the Maxwell equations:

$$\begin{aligned} \nabla \cdot \mathbf{D} = \rho, \qquad & \nabla \times \mathbf{E} + \frac{\partial \mathbf{B}}{\partial t} = 0, \\ \nabla \cdot \mathbf{B} = 0, \qquad & \nabla \times \mathbf{H} = \mathbf{J} + \frac{\partial \mathbf{D}}{\partial t}, \end{aligned} \tag{3.6}$$

where ρ is the density of free charge, and $\mathbf{J}$ is the current of free electric charges. Using the relation between $\mathbf{E}$ and $\mathbf{D}$ as well as $\mathbf{B}$ and $\mathbf{H}$, Maxwell's equations can be written in terms of the two field vectors $\mathbf{E}$ and $\mathbf{B}$ [43, 44].

Maxwell's equations with boundary and initial conditions corresponding to a considered system determine the energy density and the energy flow. According to Poynting's theorem the energy flux at the point $\mathbf{x}$ transported by the fields $(\mathbf{E}(\mathbf{x}), \mathbf{B}(\mathbf{x}))$ is given by the Poynting vector

$$\mathbf{S}(\mathbf{x}) = \frac{1}{\mu}(\mathbf{E}(\mathbf{x}) \times \mathbf{B}(\mathbf{x})). \tag{3.7}$$

Therefore, the total energy flow carried by the field $(\mathbf{E}, \mathbf{B})$ out of domain G has the value

$$P = \frac{1}{\mu}\oint_{\partial G} (\mathbf{E}(\mathbf{x}) \times \mathbf{B}(\mathbf{x})) \cdot d\mathbf{a}(\mathbf{x}). \tag{3.8}$$

3.1.2 Solution of Maxwell Equations

In the absence of free electric charges ($\rho = 0$, $\mathbf{J} = 0$), assuming that in a uniform isotropic linear medium the ε and μ are constant, the Maxwell's equations (3.6) reduce to the following waves equations:

$$\begin{aligned} \nabla \cdot \mathbf{E} = 0, \qquad & \nabla^2\mathbf{E} - \mu\varepsilon\frac{\partial^2 \mathbf{E}}{\partial t^2} = 0, \\ \nabla \cdot \mathbf{B} = 0, \qquad & \nabla^2\mathbf{B} - \mu\varepsilon\frac{\partial^2 \mathbf{B}}{\partial t^2} = 0. \end{aligned} \tag{3.9}$$

Consider an infinite medium with no boundary conditions. Since the equations for the electric and magnetic fields are the same, we only focus on the electric field equations. The equation can be solved using separation of variables. Assuming $\mathbf{E}(x, y, z, t) = \mathbf{E}^{(s)}(x, y, z)T(t)$, we get

$$\nabla^2\mathbf{E}^{(s)} + k^2\mathbf{E}^{(s)} = 0, \tag{3.10}$$

$$\nabla \cdot \mathbf{E}^{(s)} = 0, \tag{3.11}$$

$$\ddot{T} + \frac{1}{\mu\varepsilon} k^2 T = 0, \tag{3.12}$$

where (3.10) is the Helmholtz equation for a function of spatial variables, and (3.12) is the equation of a harmonic oscillator. The solutions of (3.12) are defined by,

$$T(t) = d e^{i\omega t}. \tag{3.13}$$

with the frequency

$$\omega = k/\sqrt{\mu\varepsilon}, \tag{3.14}$$

which is the dispersion relation, and the amplitude d in (3.13) may take any value. However, the classical theory of radiation based on (3.10)-(3.14) leads to the so called "Ultraviolet Catastrophe", which contradicts experiments [45, 46]. This difficulty is resolved by a hypothesis that (3.12) should be treated in terms of quantum mechanics. Planck suggested that the energy of an oscillator has levels.

$$\epsilon_n(\omega) = \hbar\omega \left(n + \frac{1}{2}\right), \qquad n = 0, 1, 2, \ldots, \tag{3.15}$$

where $\hbar = 6.62607015 \times 10^{-34}\mathrm{J} \cdot \mathrm{s}$ is the reduced Planck constant [47], and $n \geq 0$. An EM wave-packet with frequency ω and the discrete energy $\hbar\omega$, propagating with speed c, is called a photon. So n is also the number of photons for frequency ω. The value $\frac{\hbar\omega}{2}$, called the zero-point energy (ZPE), is the lowest energy level of a harmonic oscillator. A harmonic oscillator with frequency ω can have any energy level (3.15).

There can be many oscillators (assume N) with a frequency ω in this system. The oscillators can interact with each other and change their energy level. Even for a system in thermal equilibrium the energy is distributed differently among the oscillators. Since, in thermal equilibrium, the system has a constant energy, the average energy of the oscillators is constant. Since there are many oscillators in the systems, in the thermodynamic limit the average energy of these oscillators in the system can be determined by the statistical ensemble average [48, 49].

Boltzmann found that a system in thermal equilibrium with temperature T has the energy ϵ_n with the probability

$$\mathbb{P}(\epsilon_n, T) \propto e^{-\dfrac{\epsilon_n}{\kappa T}}, \tag{3.16}$$

where $\kappa = 1.380649 \times 10^{-23}$ J$\cdot$K^{-1} is the Boltzmann constant. Given this, the average energy of the ensemble of quantum harmonic oscillators, $\mathcal{P}^2(\omega, T)$, at frequency ω and temperature T has the value

$$\mathcal{P}^2(\omega, T) = \frac{\sum_{s=0}^{\infty} \epsilon_n(\omega) e^{-\frac{\epsilon_n(\omega)}{\kappa T}}}{\sum_{s=0}^{\infty} e^{-\frac{\epsilon_n(\omega)}{\kappa T}}}. \tag{3.17}$$

This can be simplified by substituting from (3.15),

$$\mathcal{P}^2(\omega, T) = \frac{\sum_{s=0}^{\infty} \hbar\omega \left(n + \frac{1}{2}\right) e^{-\frac{\hbar\omega\left(n+\frac{1}{2}\right)}{\kappa T}}}{\sum_{s=0}^{\infty} e^{-\frac{\hbar\omega\left(n+\frac{1}{2}\right)}{\kappa T}}} = \frac{\hbar\omega}{2} + \frac{\hbar\omega}{e^{\frac{\hbar\omega}{\kappa T}} - 1}. \tag{3.18}$$

Since the ZPE is not due to a thermal process it can often be neglected. Then, the average thermal energy of an equilibrium ensemble at temperature T is

$$\langle \epsilon(\omega, T) \rangle = \hbar\omega p^2(\omega, T), \tag{3.19}$$

where

$$p^2(\omega, T) = \frac{1}{e^{\frac{\hbar\omega}{\kappa T}} - 1}. \tag{3.20}$$

Going back to the Helmholtz equation (3.13), solutions $\mathbf{E}_m^{(s)}$ and $\mathbf{B}_m^{(s)}$ are plane waves

$$\mathbf{E}_m^{(s)} = \mathcal{E}_m \mathbf{p}_m e^{i(k_{x,m}x + k_{y,m}y + k_{z,m}z)} = \mathcal{E}_m \mathbf{p}_m e^{(k_m \mathbf{n}_m \cdot \mathbf{x})}, \tag{3.21}$$

$$\mathbf{B}_m^{(s)} = \mathcal{B}_m \mathbf{p}'_m e^{i(k_m \mathbf{n}_m \cdot \mathbf{x})}, \tag{3.22}$$

where

$$\mathbf{n}_m = (n_{x,m}, n_{y,m}, n_{z,m}), \tag{3.23}$$

is the unit vector parallel to the direction of wave propagation, $\mathcal{E}_m$ and $\mathcal{B}_m$ are the amplitudes of the solution, $\mathbf{p}_m = (p_{x,m}, p_{y,m}, p_{z,m})$ and $\mathbf{p}'_m = (p'_{x,m}, p'_{y,m}, p'_{z,m})$ are unit vectors, and $k_m > 0$ is the wave number.

The divergence equations in (3.9) and (3.11) enforce the conditions

$$\mathbf{p}_m \cdot \mathbf{n}_m = 0, \qquad \mathbf{p}'_m \cdot \mathbf{n}_m = 0, \tag{3.24}$$

which imply that the electric and magnetic fields are oriented perpendicular to the direction of propagation.

Equations (3.6) lead to the relationship

$$\mathbf{B}_m^{(s)} = \sqrt{\mu\varepsilon}\mathbf{n}_m \times \mathbf{E}_m^{(s)}, \tag{3.25}$$

which shows that the fields $\mathbf{B}_m^{(s)}$ and $\mathbf{E}_m^{(s)}$ are proportional and are orthogonal to each other, and to the direction of propagation $\mathbf{n}$. So the unit vectors $\mathbf{n}$, $\mathbf{p}$ and $\mathbf{p}'$ construct an orthonormal basis. The fields $\mathbf{E}_m^{(s)}$ in the direction $\mathbf{p}$ and $\mathbf{B}_m^{(s)}$ in the direction $\mathbf{p}'$ is one polarization of the EM field. Another polarization can exist for $\mathbf{E}_m^{(s)}$ in the direction $\mathbf{p}'$ and $\mathbf{B}_m^{(s)}$ in the direction $\mathbf{p}$.

The time-averaged energy density of the EM field for plane waves is computed as

$$E = \frac{1}{2}\left(\varepsilon|\mathbf{E}|^2 + \frac{1}{\mu}|\mathbf{B}|^2\right). \tag{3.26}$$

So the average energy density of each of the two polarizations of the waves in view of (3.25) is

$$E_m = \frac{1}{2}\left(\varepsilon\mathcal{E}_m^2 + \frac{1}{\mu}\mathcal{B}_m^2\right) = \frac{1}{2}\left(\varepsilon\mathcal{E}_m^2 + \frac{1}{\mu}\mu\varepsilon\mathcal{E}_m^2\right) = \varepsilon\mathcal{E}_m^2. \tag{3.27}$$

The radiative flux is

$$\mathbf{S}_m = \frac{1}{\mu}(\mathbf{E}_m \times \mathbf{B}_m) = \frac{1}{\mu}\sqrt{\mu\varepsilon}\mathcal{E}_m^2\mathbf{n}_m = \sqrt{\frac{\varepsilon}{\mu}}\mathcal{E}_m^2\mathbf{n}_m. \tag{3.28}$$

The ratio of the magnitude of the Poynting vector to the energy density gives the speed of the radiative flux as $c = 1/\sqrt{\mu\varepsilon}$.

$\mathbf{E}_m^{(s)}$ is one of many solutions of the wave equations in (3.9). The solution depends on the specified value for the wavenumber k_m, which is determined by the boundary conditions of the problem. In the case of an infinite medium, there are no boundary conditions, and there exist many solutions corresponding to any k_m. Since the equation (3.10) is linear, a linear combination of its solutions

$$\mathbf{E}(\mathbf{x}, t) = \sum_m \mathcal{E}_m\mathbf{p}_m e^{i(\omega_m\mathbf{n}_m\cdot\mathbf{x}/c)} d_m e^{-i\omega_m t}, \tag{3.29}$$

is also a solution of (3.10) and (3.11).

The radiation confined within a perfectly conducting cavity in the form of a cube $\{0 < x < L, 0 < y < L, 0 < z < L\}$ which has boundary conditions

$$\begin{cases} B_x = 0, & E_y = E_z = 0, \qquad x = 0, L, \\ B_y = 0, & E_x = E_z = 0, \qquad y = 0, L, \\ B_z = 0, & E_x = E_y = 0, \qquad z = 0, L. \end{cases} \tag{3.30}$$

is possible at discrete frequencies $\omega_m = \dfrac{m\pi c}{L}$, $m \in \mathbb{Z}^+$, which are called eigenfrequencies. The spatial part of the solution for one polarization is

$$\begin{aligned} \mathbf{E}_m^{(s)} &= \mathcal{E}_{x,m}\cos(k_{x,m}x)\sin(k_{y,m}y)\sin(k_{z,m}z)\hat{\boldsymbol{x}} \\ &+ \mathcal{E}_{y,m}\sin(k_{x,m}x)\cos(k_{y,m}y)\sin(k_{z,m}z)\hat{\mathbf{y}} \\ &+ \mathcal{E}_{z,m}\sin(k_{x,m}x)\sin(k_{y,m}y)\cos(k_{z,m}z)\hat{\mathbf{z}}, \end{aligned} \tag{3.31}$$

where $k_{x,m} = \dfrac{\pi N_{x,m}}{L}$, $k_{y,m} = \dfrac{\pi N_{y,m}}{L}$, $k_{z,m} = \dfrac{\pi N_{z,m}}{L}$ are the components of the wave vector in the x, y, and z directions. $N_{x,m}, N_{y,m}$, and $N_{z,m}$ are integers that satisfy the following expression resulted from wave equation (3.10)

$$N_{x,m}^2 + N_{y,m}^2 + N_{z,m}^2 = \frac{L^2k_m^2}{\pi^2} = \frac{L^2\omega_m^2}{c^2\pi^2}, \tag{3.32}$$

where k_m is the wave number or the magnitude of the wave vector. Also the equation (3.11) imposes that

$$\nabla \cdot \mathbf{E}_m^{(s)} = 0, \quad \Rightarrow \quad \mathcal{E}_{x,m} N_{x,m} + \mathcal{E}_{y,m} N_{y,m} + \mathcal{E}_{z,m} N_{z,m} = 0. \tag{3.33}$$

From (3.6), we also have $\nabla \times \mathbf{E} = -\dfrac{\partial \mathbf{B}}{\partial t}$, so we can obtain $\mathbf{B}_m^{(s)}$

$$\begin{aligned} \mathbf{B}_m^{(s)} = & \frac{i}{\omega} \left(\mathcal{E}_{y,m} k_{z,m} - \mathcal{E}_{z,m} k_{y,m}\right) \sin\left(k_{x,m} x\right) \cos\left(k_{y,m} y\right) \cos\left(k_{z,m} z\right) \hat{\boldsymbol{x}} \\ & + \frac{i}{\omega} \left(\mathcal{E}_{z,m} k_{x,m} - \mathcal{E}_{x,m} k_{z,m}\right) \cos\left(k_{x,m} x\right) \sin\left(k_{y,m} y\right) \cos\left(k_{z,m} z\right) \hat{\mathbf{y}} \\ & + \frac{i}{\omega} \left(\mathcal{E}_{x,m} k_{y,m} - \mathcal{E}_{y,m} k_{x,m}\right) \cos\left(k_{x,m} x\right) \cos\left(k_{y,m} y\right) \sin\left(k_{z,m} z\right) \hat{\mathbf{z}}, \end{aligned} \tag{3.34}$$

which also satisfies the boundary conditions imposed on $\mathbf{B}$ (3.30).

As (3.32) shows, there are multiple combinations of $N_{x,m}, N_{y,m}, N_{z,m}$ corresponds the same eigenfrequency; correspondingly, any solution of the wave equation (3.9) can be represented as the superposition of the normal modes.

$$\mathbf{E}(\mathbf{x}, t) = \sum_{\text{pol}} \sum_{m} \sum_{\{N_{x,m}, N_{y,m} N_{z,m}\}} \mathbf{E}_m^{(s)}(\mathbf{x}) d_m e^{-i\omega_m t}. \tag{3.35}$$

The total number of normal modes with the frequency in the interval $[\omega, \omega + d\omega]$ per unit volume of the domain is called the density of states (DOS) and is determined by Weyl's formula [50, 51]. Let $N(\omega)$ be the total number of normal modes with frequency less than ω. The theorem states that under any considered boundary conditions for equation

$$\nabla^2 u + k^2(\omega) u = 0, \tag{3.36}$$

for a space domain of large (compared to wavelength of EM waves) volume V,

$$N(\omega) \cong V \frac{k^3(\omega)}{6\pi^2}. \tag{3.37}$$

Then, the number of normal modes with the frequency from ω to $\omega + d\omega$, knowing the dispersion relation $k(\omega) = \omega/c$, is determined by

$$dN(\omega) = V \frac{k^2(\omega)}{2\pi^2} dk(\omega) = V \frac{\omega^2}{2\pi^2 c^3} d\omega = V D(\omega) d\omega, \tag{3.38}$$

where

$$D(\omega) = \frac{\omega^2}{2\pi^2 c^3}, \tag{3.39}$$

is the DOS. Since equation (3.37) describes only one polarization, the density of states of the entire field is equal to $2D(\omega)$.

3.1.3 Planck Distribution Function and Black Body Radiation

Planck's law describes the spectrum of EM waves in a large cavity inside a black body in thermal equilibrium. A black body is an idealistic body that absorbs all incident EM waves. Any body at fixed temperature which exchanges energy only through radiation, radiates the same amount of energy as it absorbs.

In order to obtain the energy spectrum of EM waves radiated by a black body into a cavity, the normal modes of the EM field in this cavity are considered. As shown above, a normal mode with frequency in the interval $[\omega, \omega + d\omega)$ has the average energy density (3.19) and there are $D(\omega)d\omega$ normal modes of each polarization in this frequency interval. So the energy density in the interval $[\omega, \omega + d\omega)$ for two polarizations of the EM field is

$$dE = \mathscr{E}(\omega, T)d\omega = 2\frac{\hbar\omega}{e^{\frac{\hbar\omega}{\kappa T}} - 1}\frac{\omega^2}{2\pi^2 c^3}d\omega, \tag{3.40}$$

where $\mathscr{E}(\omega, T)$ is the spectral energy density (Planck distribution function). The integration of (3.40) over all frequencies determines the total energy density.

$$E(T) = \int_0^\infty \mathscr{E}(\omega, T)d\omega = \int_0^\infty \frac{\hbar\omega}{e^{\frac{\hbar\omega}{\kappa T}} - 1}\frac{\omega^2}{\pi^2 c^3}d\omega. \tag{3.41}$$

Substituting $x = \dfrac{\hbar\omega}{\kappa T}$, we convert (3.41) to the form

$$E(T) = \frac{\kappa^4}{\pi^2\hbar^3 c^3}T^4 \int_0^\infty \frac{x^3}{e^x - 1}dx = \frac{\pi^2\kappa^4}{15\hbar^3 c^3}T^4. \tag{3.42}$$

where the integral is known to have the value $\pi^4/15$ [33].

A similar procedure can be used for the computation of the heat flux radiated by a black body half-space at temperature T as shown in Fig. 3.1. The flux of energy that passes through a plate $x = L$ is obtained by integration of the flux

$$dQ = dE \times c\cos\theta = \frac{\hbar\omega}{e^{\frac{\hbar\omega}{\kappa T}} - 1} \times \frac{\omega^2}{c^3}\sin\theta d\phi d\theta d\omega \times \frac{1}{(2\pi)^3} \times c\cos\theta. \tag{3.43}$$

carried by waves with frequency $[\omega, \omega + d\omega)$ and the angles $[\theta, \theta + d\theta)$ and $[\phi, \phi + d\phi)$. Then for the total heat flux we get

$$Q_{\text{out}} = \sum_{\text{pol}} \int_0^\infty \int_0^{\frac{\pi}{2}} \int_0^{2\pi} \frac{\hbar\omega^3}{e^{\frac{\hbar\omega}{\kappa T}} - 1} \times \frac{1}{8\pi^3 c^2}\sin\theta\cos\theta d\phi d\theta d\omega = \sigma T^4, \tag{3.44}$$

where

$$\sigma = \frac{\pi^2\kappa^4}{60\hbar^3 c^2}, \tag{3.45}$$

is the Stefan-Boltzmann constant, and (3.44) is the Stefan-Boltzmann law.

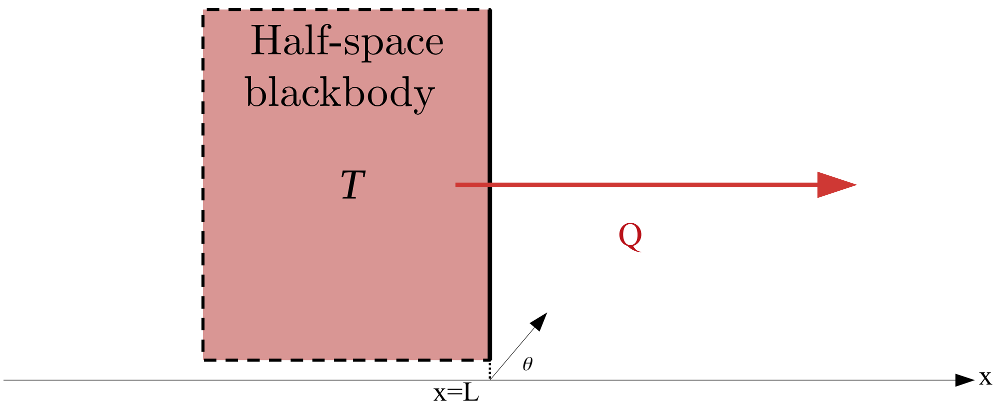

Figure 3.1: The radiative flux from a black body half-space to a vacuum half-space

3.2 Extension of Planck's Law to Systems with Steady State Heat Fluxes

Planck's law can be derived from the principle of maximum entropy, which indicates that a system in thermal equilibrium exists in its most probable configurations [48]. In statistical thermodynamics the entropy of a system is defined by

$$S = -\kappa \sum_{l} p_l \ln p_l, \tag{3.46}$$

where p_l is the probability that a system is in the l^{th} state and the summation includes all states. The sum of all probabilities must be $\sum_l p_l = 1$, and the principle of maximum entropy states that the most probable distribution of probabilities p_l maximizes the entropy (3.46).

Assume that the average energy (E) of normal modes of EM waves is characterized by a frequency ω and spherical angles (θ, ϕ), which characterize the direction of the waves. Then the normal modes can be treated as harmonic oscillators with energy states $\epsilon_l = \hbar\omega\left(l + \frac{1}{2}\right)$ from (3.15). Assume that $p_l(\omega, \theta, \phi)$ is the probability that the harmonic oscillator is in the state ϵ_l. Then, the problem is to maximize

$$S = -\kappa \sum_{r,s,t} \sum_{l} p_l(\omega_r, \theta_s, \phi_t) \ln p_l(\omega_r, \theta_s, \phi_t), \tag{3.47}$$

with the constraints

$$\begin{gathered} \sum_{l} p_l(\omega_r, \theta_s, \phi_t) = 1, \quad \forall \quad r, s, t, \\ \sum_{r,s,t} \sum_{l} p_l(\omega_r, \theta_s, \phi_t) \hbar\omega_r \left(l + \frac{1}{2}\right) = E, \end{gathered} \tag{3.48}$$

where the summation for the entropy and energy is over all normal modes and the p_l's are the parameters to choose such that S is maximized. This problem can be solved using the method of Lagrange's multipliers [52]. First we rewrite the equations in the form

$$\begin{aligned} S &= -\kappa \sum_{r,s,t} \sum_{l} p_l(\omega_r, \theta_s, \phi_t) \ln p_l(\omega_r, \theta_s, \phi_t), \\ f_{r,s,t}(p_1, \cdots, p_n, \cdots) &= 1 - \sum_{l} p_l(\omega_r, \theta_s, \phi_t) = 0, \quad \forall \quad r,s,t, \\ f_1(p_1, \cdots, p_n, \cdots) &= E - \sum_{r,s,t} \left(\frac{\hbar\omega_r}{2} + \sum_{l} p_l(\omega_r, \theta_s, \phi_t) l\hbar\omega_r \right) = 0. \end{aligned} \tag{3.49}$$

Then we maximize

$$\begin{aligned} F(p_1, \cdots, p_n, \cdots, \lambda_1, \lambda_{r,s,t}) = &- \kappa \sum_{r,s,t} \sum_{l} p_l(\omega_r, \theta_s, \phi_t) \ln p_l(\omega_r, \theta_s, \phi_t) \\ &+ \lambda_1 f_1 + \sum_{r,s,t} \lambda_{r,s,t} f_{r,s,t}, \end{aligned} \tag{3.50}$$

where $(\lambda_1, \{\lambda_{r,s,t}\})$ are as yet unknown parameters subject to

$$\frac{\partial F}{\partial p_l(\omega_r, \theta_s, \phi_t)} = 0, \qquad l = 1, \ldots, n, \quad \forall \quad r,s,t. \tag{3.51}$$

Then, solving for p_l we get

$$p_l(\omega_r, \theta_s, \phi_t) = e^{-\lambda_1 l \hbar\omega_r/\kappa} \left(1 - e^{-\lambda_1 \hbar\omega_r/\kappa}\right). \tag{3.52}$$

Then the average energy for each normal mode from the second equation in (3.47) is

$$\begin{aligned} E_{r,s,t}(\omega_r, \theta_s, \phi_t) &= \frac{\hbar\omega_r}{2} + \hbar\omega_r \left(1 - e^{-\lambda_1 \hbar\omega_r/\kappa}\right) \sum_{l} l e^{-\lambda_1 l \hbar\omega_r/\kappa} \\ &= \frac{\hbar\omega_r}{2} + \frac{\hbar\omega_r}{e^{\lambda_1 \hbar\omega_r/\kappa} - 1} = \frac{\hbar\omega_r}{2} + \hbar\omega_r p^2(\omega_r, 1/\lambda_1), \end{aligned} \tag{3.53}$$

In the above expression, the exponential term only accepts dimensionless arguments. For this to be satisfied λ_1 must have the inverse dimension of temperature $\lambda_1 = \frac{1}{T}$, where T is the temperature of the system in equilibrium, so that the average total energy is

$$E = \sum_{r,s,t} \left(\frac{\hbar\omega_r}{2} + \frac{\hbar\omega_r}{e^{\hbar\omega_r/\kappa T} - 1} \right). \tag{3.54}$$

The same method is applicable to a system with a steady heat flux [53]. The only additional assumption is that the average heat flux in the system is predefined.

Assume that normal modes of EM waves are characterized by their frequencies ω and spherical angles (θ, ϕ). These modes can be treated as harmonic oscillators with the energy states $\epsilon_l = \hbar\omega\left(l + \frac{1}{2}\right)$ from (3.15). Assume the probability that a normal mode is in the state ϵ_l is $p_l(\omega, \theta, \phi)$. Let the normal modes have the average energy density E and carry the flux Q in the x-direction. Then, we maximize entropy.

$$S = -\kappa \sum_{r,s,t} \sum_{l} p_l(\omega_r, \theta_s, \phi_t) \ln p_l(\omega_r, \theta_s, \phi_t), \tag{3.55}$$

with the constraints

$$\begin{aligned} \sum_{l} p_l(\omega_r, \theta_s, \phi_t) &= 1, \quad \forall \quad r, s, t, \\ \sum_{r,s,t} \sum_{l} p_l(\omega_r, \theta_s, \phi_t) l\hbar\omega_r &= E, \\ \sum_{r,s,t} \sum_{l} p_l(\omega_r, \theta_s, \phi_t) l\hbar\omega_r \cdot c_l \cos\theta_s &= Q, \end{aligned} \tag{3.56}$$

where $c_l(\omega_r, \theta_s, \phi_t)$ is the wave speed. The problem (3.55)-(3.56) can be solved in a similar way as that for the case in thermal equilibrium. We use λ_1, λ_2 and $\{\lambda_{r,s,t}\}$ as Lagrange multipliers, and we rewrite the equations as

$$\begin{aligned} S &= -\kappa \sum_{r,s,t} \sum_{l} p_l(\omega_r, \theta_s, \phi_t) \ln p_l(\omega_r, \theta_s, \phi_t), \\ f_{r,s,t} &= 1 - \sum_{l} p_l(\omega_r, \theta_s, \phi_t) = 0, \quad \forall \quad r, s, t, \\ \text{for: } f_1 &= E - \sum_{r,s,t} \left(\frac{\hbar\omega_r}{2} + \sum_{l} p_l(\omega_r, \theta_s, \phi_t) l\hbar\omega_r \right) = 0, \\ f_2 &= \sum_{r,s,t} \sum_{l} p_l(\omega_r, \theta_s, \phi_t) l\hbar\omega_r \cdot c_l \cos\theta_s - Q = 0. \end{aligned} \tag{3.57}$$

Assume $\lambda_1 = 1/T$, and $\lambda_2 = \mu/T$. Then we maximize

$$\begin{aligned} F(p_1, \ldots, p_n, \ldots, T, \mu, \lambda_{r,s,t}) = &-\kappa \sum_{r,s,t} \sum_{l} p_l(\omega_r, \theta_s, \phi_t) \ln p_l(\omega_r, \theta_s, \phi_t) \\ &+ \frac{1}{T} f_1 + \frac{\mu}{T} f_2 + \sum_{r,s,t} \lambda_{r,s,t} f_{r,s,t}. \end{aligned} \tag{3.58}$$

So

$$\frac{\partial F}{\partial p_l(\omega_r, \theta_s, \phi_t)} = 0, \qquad l = 1, \ldots, n, \quad \forall \quad r, s, t. \tag{3.59}$$

Solving for p_l we get

$$\begin{aligned} \frac{\partial F}{\partial p_l} &= -\kappa - \kappa \ln p_l - l\hbar\omega_r[1 - \mu \cdot c_l \cos\theta_s]/T - \lambda_{r,s,t} = 0, \\ &\Rightarrow \ln p_l = -1 - \lambda_{r,s,t}/\kappa - l\hbar\omega_r[1 - \mu \cdot c_l \cos\theta_s]/\kappa T, \end{aligned} \tag{3.60}$$

which gives

$$p_l = e^{-1-\lambda_{r,s,t}/\kappa - l\hbar\omega[1-\mu\cdot c_l\cos\theta_s]/\kappa T}. \tag{3.61}$$

Assume $c_l(\omega_r, \theta_s, \phi_t)$ is constant for all l's when $\omega_r, \theta_s, \phi_t$ are fixed, then we get

$$\begin{aligned} \sum_l p_l = \sum_l e^{-1-\lambda_{r,s,t}/\kappa - l\hbar\omega_R[1-\mu\cdot c\cos\theta_s]/\kappa T} &= 1, \\ \Rightarrow e^{-1-\lambda_{r,s,t}/\kappa} \sum_l e^{-l\hbar\omega_r[1-\mu\cdot c\cos\theta_s]/\kappa T} &= 1, \\ \Rightarrow \frac{e^{-1-\lambda_{r,s,t}/\kappa}}{1-e^{-\hbar\omega_r[1-\mu\cdot c\cos\theta_s]/\kappa T}} = 1 \Rightarrow e^{-1-\lambda_{r,s,t}/\kappa} &= 1 - e^{-\hbar\omega_r[1-\mu\cdot c\cos\theta_s]/\kappa T}. \end{aligned} \tag{3.62}$$

This simplifies p_l to

$$p_l(\omega_r, \theta_s, \phi_t) = e^{-l\hbar\omega_r[1-\mu\cdot c\cos\theta_s]/\kappa T}\left(1 - e^{-\hbar\omega_r[1-\mu\cdot c\cos\theta_s]/\kappa T}\right). \tag{3.63}$$

Then, the result for E is

$$\begin{aligned} E &= \sum_{r,s,t}\sum_l p_l(\omega_r, \theta_s, \phi_t) l\hbar\omega_r \\ &= \int_0^{2\pi} d\phi \sum_{r,s}\left(\hbar\omega_r\left(1 - e^{-\hbar\omega_r[1-\mu\cdot c\cos\theta_s]/\kappa T}\right)\sum_l l e^{-l\hbar\omega[1-\mu\cdot c\cos\theta_s]/\kappa T}\right) \\ &= \int_0^{2\pi} d\phi \sum_{r,s} \frac{\hbar\omega_r}{e^{\hbar\omega_r[1-\mu\cdot c\cos\theta_s]/\kappa T}-1} = \int_0^{2\pi} d\phi \sum_{r,s} \hbar\omega_r p^2(\omega_r[1-\mu c\cos\theta_s], T). \end{aligned} \tag{3.64}$$

Similarly for Q we get

$$\begin{aligned} Q &= \int_0^{2\pi} d\phi \sum_{r,s}\sum_l p_l(\omega_r, \theta, \phi) l\hbar\omega_r \cdot c\cos\theta_s \\ &= \int_0^{2\pi} d\phi \sum_{r,s} \hbar\omega_r p^2(\omega_r[1-\mu c\cos\theta_s], T)\cdot c\cos\theta_s. \end{aligned} \tag{3.65}$$

To summarize the results

$$\begin{aligned} E &= \int_0^{2\pi} d\phi \sum_{r,s} \hbar\omega_r p^2(\omega_r[1-\mu c\cos\theta_s], T), \\ Q &= \int_0^{2\pi} d\phi \sum_{r,s} \hbar\omega_r p^2(\omega_r[1-\mu c\cos\theta_s], T)\cdot c\cos\theta_s. \end{aligned} \tag{3.66}$$

In the above equations, the expression $p^2(\omega[1-\mu c\cos\theta], T)$ is the Planck's function with a modified argument that takes into account steady heat flux. The expression $\hbar\omega p^2(\omega[1 -$

$\mu c\cos\theta], T)$ gives the average energy of the normal mode in the direction (θ, ϕ) where $\theta \in [0, \pi]$ and $\phi \in [0, 2\pi]$. The parameter $q = \mu c$ is a coefficient with $0 \le q \le 1$ which determines how much the system is deviated from the equilibrium condition. The case $q = 0$ represents thermal equilibrium where $Q = 0$, and as $|q|$ becomes greater, the system moves more away from equilibrium.

The total energy density and the net heat flux from all angles and frequencies are determined from the following equations by summing over all normal modes

$$\begin{aligned}
E(T,q) &= \sum_{\text{pol}} \int_0^\infty \int_0^\pi \int_0^{2\pi} \left[p^2(\omega[1-q\cos\theta],T)\right] \frac{\hbar\omega^3}{8\pi^3 c^3} \sin\theta d\phi d\theta d\omega, \\
Q(T,q) &= \sum_{\text{pol}} \int_0^\infty \int_0^\pi \int_0^{2\pi} \left[p^2(\omega[1-q\cos\theta],T)\right] \frac{\hbar\omega^3}{8\pi^3 c^2} \sin\theta\cos\theta d\phi d\theta d\omega.
\end{aligned} \tag{3.67}$$

It is convenient to separate the waves with $\theta \in [0, \pi/2]$ and $\theta \in [\pi/2, \pi]$ since they carry energy in the opposite directions $x \to +\infty$ and $x \to -\infty$. This gives

$$\begin{aligned}
E(T,q) = \sum_{\text{pol}} \int_0^\infty \int_0^{\frac{\pi}{2}} \int_0^{2\pi} & \left[p^2(\omega[1-q\cos\theta],T) + p^2(\omega[1+q\cos\theta],T)\right] \\
& \times \frac{\hbar\omega^3}{8\pi^3 c^3} \sin\theta d\phi d\theta d\omega, \\
Q(T,q) = \sum_{\text{pol}} \int_0^\infty \int_0^{\frac{\pi}{2}} \int_0^{2\pi} & \left[p^2(\omega[1-q\cos\theta],T) - p^2(\omega[1+q\cos\theta],T)\right] \\
& \times \frac{\hbar\omega^3}{8\pi^3 c^2} \sin\theta\cos\theta d\phi d\theta d\omega.
\end{aligned} \tag{3.68}$$

For $d\Omega = \dfrac{\omega^2}{8\pi^3 c^3} \sin\theta d\phi d\theta d\omega$ and $\Omega \in [0, \infty] \times [0, \pi/2] \times [0, 2\pi]$,

$$\begin{aligned}
E_\Omega(T,q) &= \sum_{\text{pol}} \int_\Omega \hbar\omega \left[p^2(\omega[1-q\cos\theta],T) + p^2(\omega[1+q\cos\theta],T)\right] d\Omega, \\
Q_\Omega(T,q) &= \sum_{\text{pol}} \int_\Omega \hbar\omega \left[p^2(\omega[1-q\cos\theta],T) - p^2(\omega[1+q\cos\theta],T)\right] c\cos\theta d\Omega.
\end{aligned} \tag{3.69}$$

3.3 Extension of Planck's Law for Large heat fluxes

In section 3.2, the extension of Planck's law was obtained by the principle of maximum entropy for systems with a steady heat flux. It is also instructive to see that it can be derived by a different approach [54].

Assume that the radiation field is modeled by an ensemble of waves in a reference frame **O**, where it has a flux Q, as demonstrated in Fig. 3.2. Then, there exist an auxiliary frame

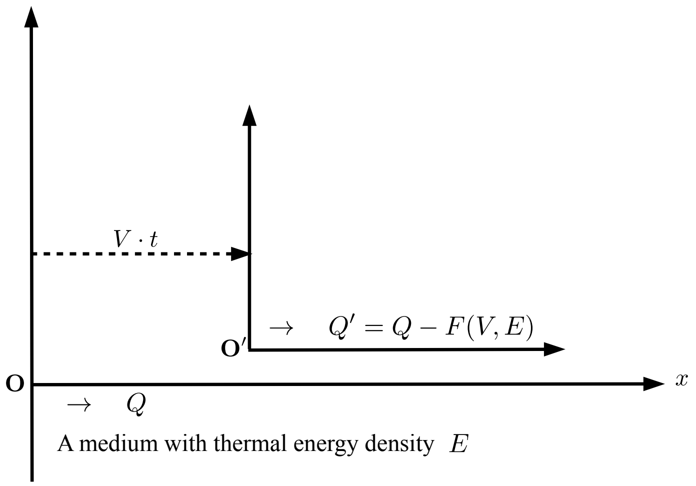

Figure 3.2: Heat flux in the reference frame and the auxiliary frame, in the auxiliary frame the heat flux is function of the energy density of the medium and the speed of the frame

O′ that moves along the direction of the x axis as shown in Fig. 3.2 that the heat flux in this frame is zero at a certain speed V. In the frame **O′** with no heat flux, the radiation appears to be in equilibrium, and thus, its energy levels can be described by the Planck law for thermal equilibrium.

$$p^2_{\mathbf{O}'} = \frac{1}{e^{\left(\dfrac{\hbar\omega'}{\kappa T'}\right)} - 1}, \tag{3.70}$$

which is identical to (3.20), except the frequency ω and the temperature T in the reference frame is replaced by the frequency ω' and the temperature T' in the moving frame **O′**. Since the energy levels cannot depend on the frame, the energy levels in the reference frame **O** is also given by (3.70). We just need to write the expression in terms of variables of the frame **O**. The variables to convert are the frequency ω' to ω and the temperature T' to T.

If the heat flux in the reference frame **O** is small, then the speed of the moving frame for a nonzero heat flux is relatively small to the speed of light. In this case, the frequency in the moving frame is converted to the frequency in the reference frame by Doppler shift formulation

$$\omega' = \omega \left[1 - V/c \cos\theta\right], \tag{3.71}$$

where V is the speed of moving frame **O′**, and c is the speed of the waves in the medium. The temperatures in the two frames will be the same $T' = T$. So the energy levels in the reference frame **O** are given by

$$p_{\mathbf{O}}^2 = \frac{1}{e^{\left(\frac{\hbar\omega\left[1 - V/c\cos\theta\right]}{\kappa T}\right)} - 1}, \tag{3.72}$$

This is similar to the derived equation from the maximum entropy method in section 3.2 assuming $q = V/c$. This suggests that, the results obtained in the previous sections are only applicable to small steady state net heat flux systems.

If the heat flux in the reference frame **O** is large, the speed of the moving frame, when the flux vanishes, increases considerably and may become comparable to the speed of light. Then, taking into account the special relativity we find

$$\omega' = \omega\gamma\left[1 - q\cos\theta\right], \tag{3.73}$$

where

$$\gamma = \frac{1}{\sqrt{1 - \left(\frac{V}{c_0}\right)^2}} = \frac{1}{\sqrt{1 - \left(\frac{c}{c_0}\right)^2 q^2}}, \tag{3.74}$$

is the Lorentz factor, and c_0 is the speed of light in vacuum. So the Planck's function under this transformation is

$$p_{\mathbf{O}}^2 = p^2(\omega\gamma\left[1 - q\cos\theta\right], T_{\mathbf{O}}) = \frac{1}{e^{\left(\frac{\hbar\omega\gamma\left[1 - q\cos\theta\right]}{\kappa T'}\right)} - 1}. \tag{3.75}$$

So when the heat fluxes are extremely large the equation (3.75), which has an extra γ factor, needs to be considered.

It should be noted that in the special relativity framework, the temperature in the two frames can also be different. The proper transformation between two frames has been a long discussion among physicists. There are at least three transformations suggested.

$$T' = \gamma^\nu T, \quad \text{where} \begin{cases} \nu = 2, & \text{Einstein transformation[55]}, \\ \nu = -2, & \text{Ott transformation[56]}, \\ \nu = 0, & \text{invariant temperature[57]}. \end{cases} \tag{3.76}$$

But none has been accepted in the literature for this transformation. The choice of transformation does not affect the analysis, and the results in the next chapter may provide a way to resolve this issue about the correct relativistic transformation of temperature. Given (3.75), we must replace this expression into (3.69) when working with large heat fluxes.

Chapter 4

Nanoscale Heat Transfer by Radiation

In this chapter the radiative heat flux in nanoscale multilayered structures is studied separately for small and larger heat fluxes.

4.1 Radiation for Small Heat Fluxes

In chapter 3, the expression for the radiative heat flux in a body at temperature T with factor q at steady state was derived.

$$Q_\Omega(T,q) = \sum_{\text{pol}} \int_\Omega \hbar\omega \left[p^2(\omega[1-q\cos\theta],T) - p^2(\omega[1+q\cos\theta],T)\right] c\cos\theta d\Omega. \tag{4.1}$$

In this chapter, we use this formula to calculate the heat flux in a multilayered structure with a given temperature difference between end-layers. First, we consider the radiation across a vacuum gap between two half-spaces A and B with temperatures T_A and T_B shown in Fig. 4.1 and characterize the HTC as a function of the gap spacing H.

According to (4.1) the heat flux in the system can be calculated in two different ways using the parameters of the two half-spaces as $Q = Q_{\Omega_A}(T_A, q_A)$ and $Q = Q_{\Omega_B}(T_B, q_B)$ where the parameters q_A and q_B are unknown, Ω_A and Ω_B are the domains of integration associated with A and B, respectively. The waves propagation directions (θ_A and θ_B) in the domains are related by Snell's law

$$c_A \sin\theta_B = c_B \sin\theta_A, \tag{4.2}$$

where c_A and c_B are the speeds of waves in A and B. So the domains of integration for A and B depend on each other as follows

$$\begin{aligned} \Omega_A &\in [0,\infty] \times [0,\theta_A^c] \times [0,2\pi], \\ \Omega_B &\in [0,\infty] \times [0,\theta_B^c] \times [0,2\pi], \end{aligned} \tag{4.3}$$

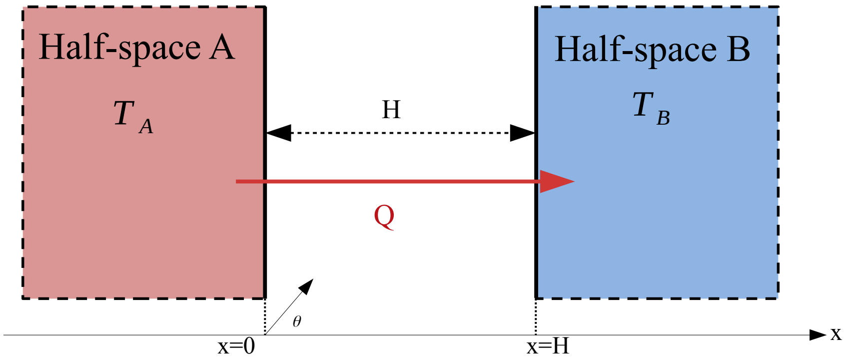

Figure 4.1: Two half-spaces A and B with temperatures T_A and T_B with a gap spacing of H

where θ_A^c and θ_B^c are the critical angles determined as

$$\theta_A^c = \begin{cases} \arcsin\left(\frac{c_A}{c_B}\right), & c_A \le c_B, \\ \frac{\pi}{2}, & c_A > c_B, \end{cases} \qquad \theta_B^c = \begin{cases} \arcsin\left(\frac{c_B}{c_A}\right), & c_B \le c_A, \\ \frac{\pi}{2}, & c_B > c_A. \end{cases} \tag{4.4}$$

Assume that the waves in different domains are not coupled as in the Landauer formalism [2, 58]. This approach is based on the following steps: 1. compute the heat flux $Q_{A\to B}(T_A, q_A)$ from A to B; 2. compute the heat flux $Q_{B\to A}(T_B, q_B)$ from B to A; 3. write the net heat flux Q as the difference between the two heat fluxes

$$Q = Q_{A\to B}(T_A, q_A) - Q_{B\to A}(T_B, q_B). \tag{4.5}$$

In order to calculate $Q_{A\to B}(T_A, q_A)$ we note that not all waves in A carry energy to B. Only the waves propagating to the right propagate towards B and carry energy to B. Similarly the waves propagating towards B do not transfer all of their energy to B since part is reflected back on the interface. Assume $R(\omega, \theta_A, H)$ is the reflection coefficient of waves in A with frequency ω and incident angle θ_A. Then, only a fraction $(1-|R_A|^2)$ of the energy of these waves is transmitted to B. Let $dE_A = \hbar\omega p^2(\omega[1-q\cos\theta], T)d\Omega_A$ be the energy density of such waves. Then the heat flux from A to the B along the x axis is $(1-|R_A|^2)\cdot dE_A \cdot c_A \cos\theta_A$. Then to find $Q_{A\to B}$ we integrate over all frequencies, angles and polarizations.

$$Q_{A\to B}(T_A, q_A) = \sum_{\text{pol}} \int_{\Omega_A} \hbar\omega p^2(\omega[1-q_A\cos\theta_A], T_A) c_A \cos\theta_A \left[1-|R_A|^2\right] d\Omega_A. \tag{4.6}$$

Similarly, for $Q_{B\to A}$ we can write an expression

$$Q_{B\to A}(T_B, q_B) = \sum_{\text{pol}} \int_{\Omega_B} \hbar\omega p^2(\omega[1+q_B\cos\theta_B], T_B) c_A \cos\theta_B \left[1-|R_B|^2\right] d\Omega_B. \tag{4.7}$$

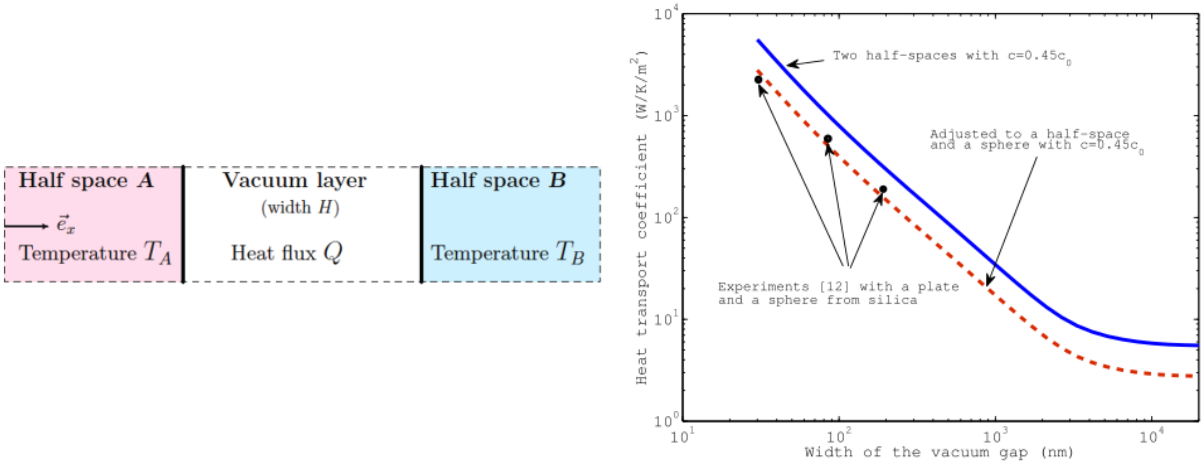

(a) Two half-spaces with a gap in between (b) Radiative HTC vs gap spacing

Figure 4.2: Radiative HTC using a linearized model for small heat fluxes vs the gap spacing [34]

We can combine (4.5), (4.6), and (4.7) and use Snell's law (4.2) to write

$$Q = \sum_{\text{pol}} \int_{\Omega_A} \hbar\omega \left\{ p^2(\omega[1 - q_A \cos\theta_A], T_A) - p^2(\omega[1 + q_B \cos\theta_B], T_B) \right\} \\ \times c_A \cos\theta_A \left|1 - \left|R_A^2\right|\right| d\Omega_A. \tag{4.8}$$

So we have the following system of nonlinear equations

$$\begin{cases} Q = Q_{\Omega_A}(T_A, q_A), \\ Q = Q_{\Omega_B}(T_B, q_B), \\ Q = Q_{A\to B}(T_A, q_A) - Q_{B\to A}(T_B, q_B), \end{cases} \tag{4.9}$$

with three unknowns (Q, q_A, q_B) to solve for. The reflection coefficients of EM waves involved into (5.30) is computed by the methods from [59].

When the temperature difference and heat flux between the half-spaces is small the obtained equations can be linearized. In this case, q_A and q_B are small and from the first two equations in (4.9) we get $q_A = \dfrac{Q}{c_A E_{\Omega_A}(T_A, 0)}$ and $q_B = \dfrac{Q}{c_B E_{\Omega_B}(T_B, 0)}$ whose substitution into the third equations of (4.9) results in a scalar equation

$$Q = Q_{A\to B}\left(T_A, \frac{Q}{c_A E_A}\right) - Q_{B\to A}\left(T_B, \frac{Q}{c_B E_B}\right). \tag{4.10}$$

If Q and ΔT are small, then (4.10) can be linearized, which give

$$\text{HTC} = \frac{Q}{\Delta T} = \frac{F_0}{1 + F_1}, \tag{4.11}$$

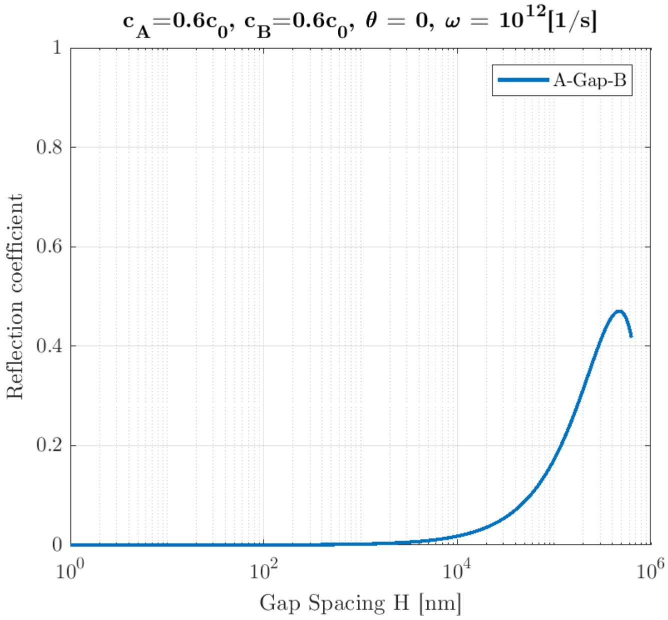

Figure 4.3: The reflection coefficient of radiative waves vs gap spacing for the structure in Fig. 4.2a with identical half-spaces with speed $c = 0.6c_0$

where

$$F_0 = \sum_{\text{pol}} \int_{\Omega_A} \hbar\omega \frac{\partial}{\partial T} \left\{p^2(\omega, T_B)\right\} c_A \cos\theta_A \left|1 - \left|R_A^2\right|\right| d\Omega_A, \tag{4.12}$$

$$F_1 = \sum_{\text{pol}} \int_{\Omega_A} \hbar\omega \frac{\partial}{\partial \omega} \left\{p^2(\omega, T_B)\right\} \left(\frac{\omega\cos\theta_A}{c_A E_A} + \frac{\omega\cos\theta_B}{c_B E_B}\right) c_A \cos\theta_A \left|1 - \left|R_A^2\right|\right| d\Omega_A. \tag{4.13}$$

In Fig. 4.2, we plot HTC as a function of gap spacing H due to EM waves in cases of a small heat flux between the half-spaces. When the spacing is greater than 10μm, the results agree with the Stefan-Boltzmann law (3.44). The HTC enhancement beyond blackbody radiation starts as the spacing between the two half-spaces drops below 10μm, which is approximately the dominant wavelength of the radiation spectrum at room temperature. This can be explained as follows: as the gap spacing decreases below the dominant wavelength of the radiation spectrum, the reflection coefficient starts decreasing, as shown in Fig. 4.3, and more energy passes through the gap resulting in the increase of HTC. This increase is proportional to $\frac{1}{H^2}$ when $H \to 0$. To get this estimate, we expand the three expressions for Q from (4.9) for q_A and q_B when H is small. For narrow spacing of $H \ll 1$ between identical materials, the reflection coefficient can be estimated by $R \sim H$. So

$$\begin{gathered} Q = q_A G(T_A) + o(q_A), \\ Q = q_A G(T_B) + o(q_B), \\ Q = \left[\frac{1}{2}\sigma\left(T_A^4 - T_B^4\right) + \frac{1}{2} q_A G(T_A) + \frac{1}{2} q_B G(T_B)\right]\left(1 - H^2\right) + o(q_A, q_B), \end{gathered} \tag{4.14}$$

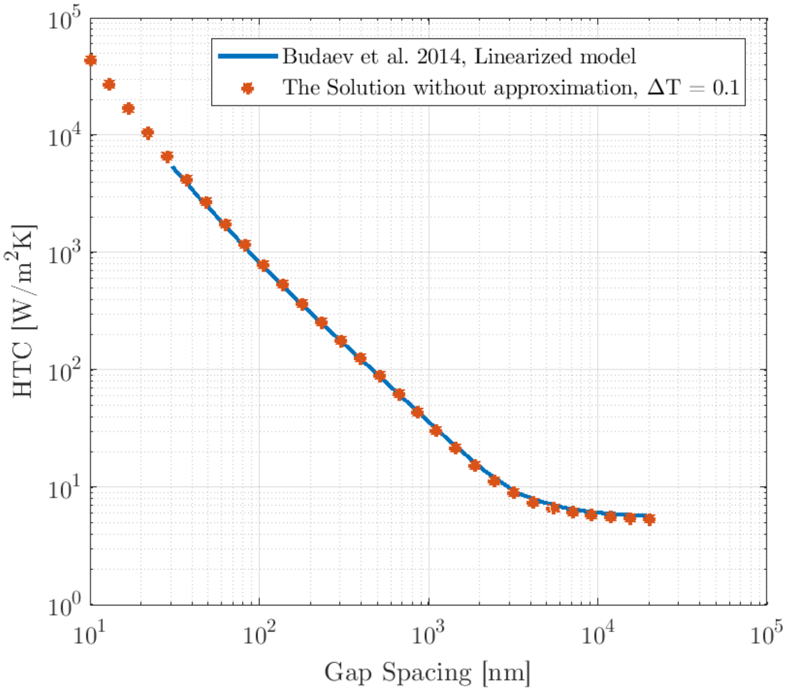

Figure 4.4: The radiative HTC from the linearized model for small heat fluxes in 4.2a is compared with our computations for the same structure with a small temperature difference

where

$$G(T) = \sum_{\text{pol}} \int_{\Omega_A} \hbar\omega \frac{\partial}{\partial\omega} \left\{p^2(\omega, T)\right\} (2\omega\cos\theta_A)\, c_A \cos\theta_A d\Omega_A. \tag{4.15}$$

Then by substituting q_A and q_B in the third equation of (4.14) we get

$$Q \equiv \frac{\frac{1}{2}\sigma\left(T_A^4 - T_B^4\right)}{H^2} + o(q_A, q_B), \tag{4.16}$$

so that the HTC of the narrow spacing is proportional to $\frac{1}{H^2}$.

In the shown results, the two half-spaces A and B are considered to be identical, which means that at zero spacing, the thermal resistance between them is zero. Hence, there can be a heat flux across the two half-spaces even if there is no temperature difference between A and B which leads to an infinite HTC. This is correctly predicted in Fig. 4.2.

Since the above results in Fig. 4.2b are obtained for small temperature differences and heat fluxes, we should be able to obtain the same result using the original equations in (4.9) when we specify a small ΔT. This is shown in Fig. 4.4 where the HTC from [34] are compared with the HTC for the same structure with a temperature difference $\Delta T = 0.1$ by solving (4.9). The numerical method to solve this is explained in subsection 4.2.1.

4.2 Intense Radiative Heat Flux

4.2.1 Heat Flux Formulations

In the case of a large heat flux between two half-spaces, the expressions in (3.69) and (4.8) change as follows

$$\begin{aligned}
Q = \sum_{\text{pol}} \int_{\Omega_A} & \hbar\omega \left[p^2(\omega\gamma_A[1 - q_A\cos\theta_A], T'_A) - p^2(\omega\gamma_A[1 + q_A\cos\theta_A], T'_A)\right] \\
& \times c_A \cos\theta_A d\Omega_A = F_1(q_A), \\
Q = \sum_{\text{pol}} \int_{\Omega_B} & \hbar\omega \left[p^2(\omega\gamma_B[1 - q_B\cos\theta_B], T'_B) - p^2(\omega\gamma_B[1 + q_B\cos\theta_A], T'_B)\right] \\
& \times c_B \cos\theta_B d\Omega_B = F_2(q_B), \\
Q = \sum_{\text{pol}} \int_{\Omega_A} & \hbar\omega \left\{p^2(\omega\gamma_A[1 - q_A\cos\theta_A], T'_A) - p^2(\omega\gamma_B[1 - q_B\cos\theta_B], T'_B)\right\} \\
& \times c_A \cos\theta_A \left|1 - R_A^2\right| d\Omega_A = F_3(q_A, q_B),
\end{aligned} \tag{4.17}$$

where q_A, q_B are the non-equilibrium coefficients in A and B, and γ_A and γ_B are the Lorentz factors (3.74) in A and B, and the temperature T'_A and T'_B are determined by (3.76). Since, according to (3.74), γ_A and γ_B are functions of q_A and q_B, the equations in (4.17) have three unknowns (Q, q_A, q_B). This can be summarized as a system of equations.

$$Q = F_1(q_A), \qquad Q = F_2(q_B), \qquad Q = F_3(q_A, q_B), \tag{4.18}$$

where this system of nonlinear equations can be rearranged and solved using an iterative method. A suitable method is the Fixed-Point Iteration Method, which is based on the Banach fixed-point theorem [60]. In (4.18), the equations can be rewritten as

$$Q - F_1(q_A) + q_A = G_1(q_A, Q), \tag{4.19}$$

$$Q - F_2(q_B) + q_B = G_2(q_B, Q), \tag{4.20}$$

$$Q = F_3(q_A(Q), q_B(Q)) = G_3(Q). \tag{4.21}$$

For given initial values ($q_{A_0} \in [-1, 1], q_{B_0} = [-1, 1], Q_0 = 0$) the equations can be solved using the algorithm in appendix A which is implemented in Matlab. In the following sections this method is used for all the calculations.

4.2.2 Temperature Transformation Choices

The above calculations depend on the assumption about the temperature transformation between frames (Einstein transformation, Ott transformation, or invariant temperature) from (3.76). Fig. 4.5 shows heat flux vs. gap spacing for two identical half-spaces with the speed

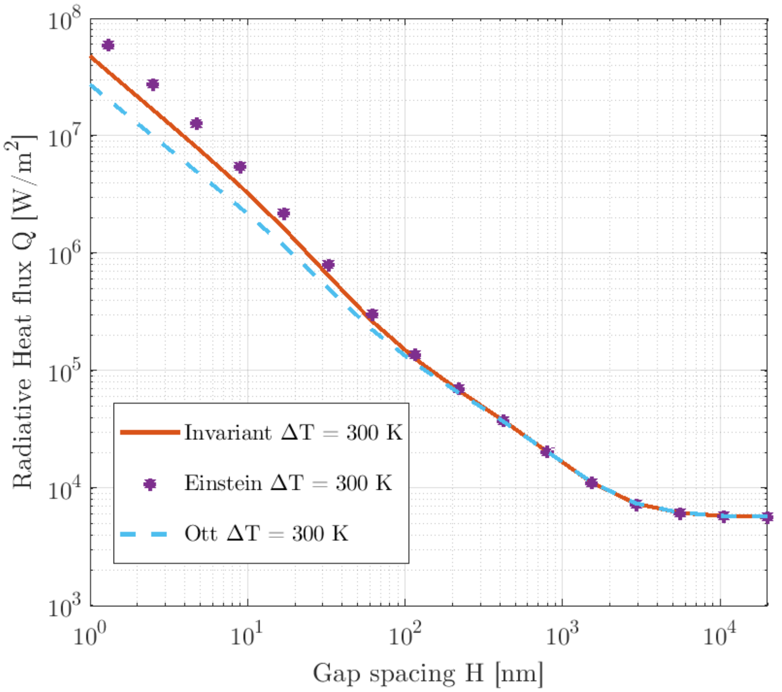

Figure 4.5: Radiative heat flux between two identical half-spaces with the light speeds $c_A = c_B = 0.45c_0$ for $\Delta T = 300$ K and $T_B = 298$ K, under different temperature transformations from (3.76)

$c = 0.45c_0$ for large temperature differences. The results for Einstein and Ott transformations of the temperature and the invariant temperature are shown by solid lines, dashed lines, and dotted lines respectively. For a small Q all three transformations give essentially the same results. On the other hand, for a large Q, the relativistic effect is observable. However, the differences among the various transformations is not very significant even for a large heat flux.

Next, two different materials with EM wave speeds $c_A = 0.6c_0$ and $c_B = 0.45c_0$ are considered and the results of computations are given in Fig. 4.6. In this case, various temperature transformations do not make a difference because the large reflection between the materials leads to a small heat flux. So the corresponding q values are small and the effect of γ is negligible.

The same simulations were preformed for two identical half-spaces covered by thin overcoats and separated by a vacuum gap, and the results are shown in Fig. 4.7. The results for this case are not very different from two identical half-spaces.

Therefore, we can conclude that the effects of the three proposed temperature transformations are negligible even for large heat fluxes. Hence, in the following sections, the invariant temperature assumption is used.

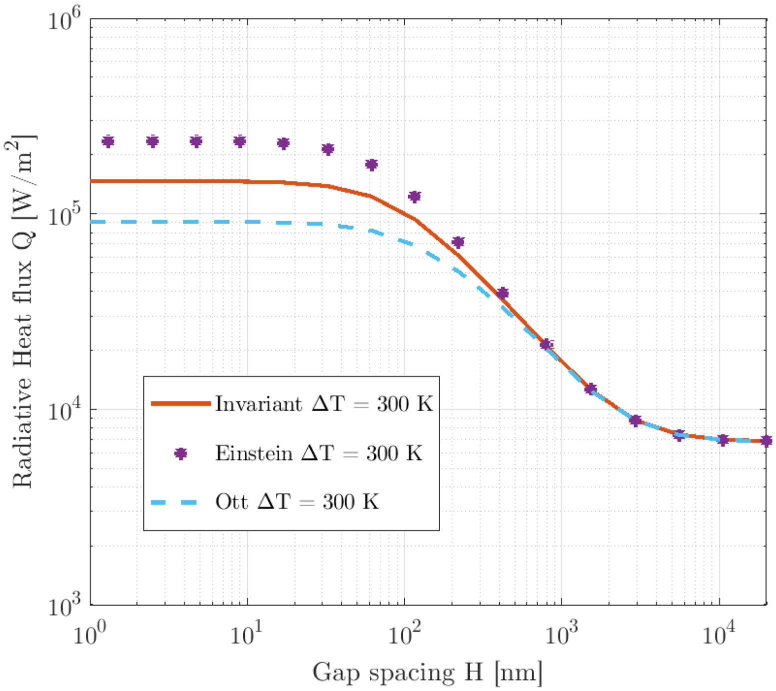

Figure 4.6: Radiative heat flux between two different half-spaces with the light speeds $c_A = 0.6c_0$ and $c_B = 0.45c_0$ for $\Delta T = 300$ K and $T_B = 298$ K, under different temperature transformations from (3.76)

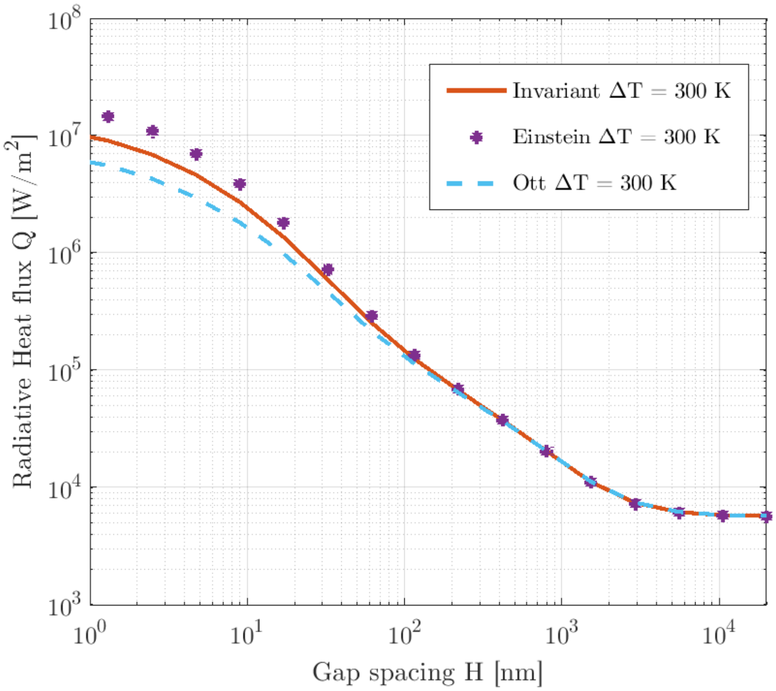

Figure 4.7: Radiative heat flux between two identical layered half-spaces with the light speeds $c_A = c_B = 0.45c_0$ for $\Delta T = 300$ K and $T_B = 298$ K, under different temperature transformations from (3.76)

4.2.3 Radiation in Multilayered Structures

Consider a structure where two identical half-spaces, A and B in Fig. 4.8a, are separated by a vacuum gap, whose width ranges from 0.1nm to 20μm. The right half-space (B) is fixed at room temperature $T_B = 298$ K. As for the temperature in A we consider three cases $T_A = T_B + \Delta T$, where $\Delta T = 4, 40, 400$. The wave speed in both half-spaces is set to $c_A = c_B = 0.45c_0$, which makes it possible to compare the results with [34]. The results of the calculations are shown in Fig. 4.8 by solid lines, which agree with the results from [34] and demonstrate the divergence of the heat flux as $H \to 0$ at the expected rate $\frac{1}{H^2}$. The start of the divergence for EM waves at room temperature is around 10μm.

Fig. 4.8 also shows heat flux between half-spaces with different material properties. The half-space B has the wave speed $c_B = 0.45c_0$ while the wave speed in A is $c_A = 0.6c_0$. The temperatures of the half-spaces are set as in the previous case: B is maintained at $T_B = 298$ K, while the temperatures of A is $T_A = T_B + \Delta T$ for three cases $\Delta T = 4, 40, 400$. The corresponding results are shown by lines with stars corresponding to different temperatures. All the lines with stars approach horizontal asymptotes in both cases of increasing and decreasing H. As the width of the gap increases, the lines corresponding to heat flux between different materials become very close to solid lines corresponding to structures with identical half-spaces. This result agrees with the Stefan-Boltzmann law. But for spacings noticeably lower than the dominant wavelength of thermal radiation, the heat flux approaches a constant value higher than the case with large spacings.

Fig. 4.8c confirms that as a gap between identical materials narrows below the dominant wavelength the thermal resistance of the gap approaches zero. However, if materials of the half-spaces are different, then the thermal resistance of a narrowing gap approaches the interface resistance limit at $H = 0$.

Next we consider more complicated structures shown in Fig. 4.9, in which the half-spaces have overcoats and are maintained at the temperatures $T_A = 698$ K and $T_B = 298$ K. The three solid lines in Fig. 4.9c show the heat fluxes between identical half-spaces coated with 0.5 nm, 1 nm, and 2 nm-thick layers of a material with the wave speed $0.7c_0$. These lines noticeably differ from each other only where the gap's width H is a few nanometers i.e. is comparable with the widths of the coating layers. The next three lines, all coinciding in this figure, show the heat fluxes between coated different half-spaces (with wave speeds $c_A = 0.6c_0$ and $c_B = 0.45c_0$) both of which are coated by 0.5 nm, 1 nm, and 2 nm-thick layers with the wave speed $0.7c_0$. As the separation H decreases below the dominant wavelength of the thermal radiation, these three lines approach the same constant level, which is independent of the thickness of the thin overcoat. This remarkable behavior agrees with the expectation that layers significantly thinner than the dominant wavelength of radiation cannot noticeably alter the radiative heat transport between the half-spaces.

The obtained results demonstrate that the radiative heat flux across a stack of layers with total thickness below 50 nm is practically independent of the layers. Therefore, for HAMR needs, the radiative heat flux across a stack of layers between non-identical half-spaces can

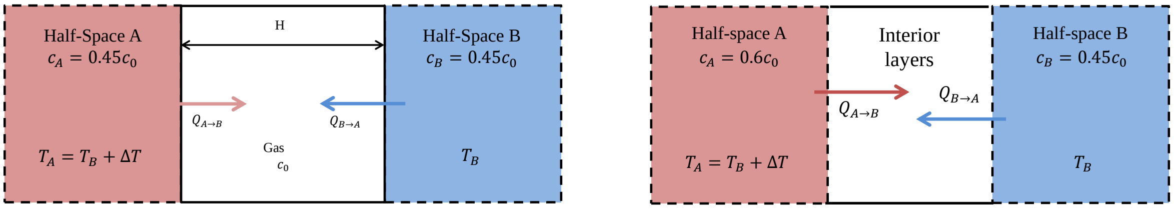

(a) Identical Half-spaces (b) Different Half-spaces

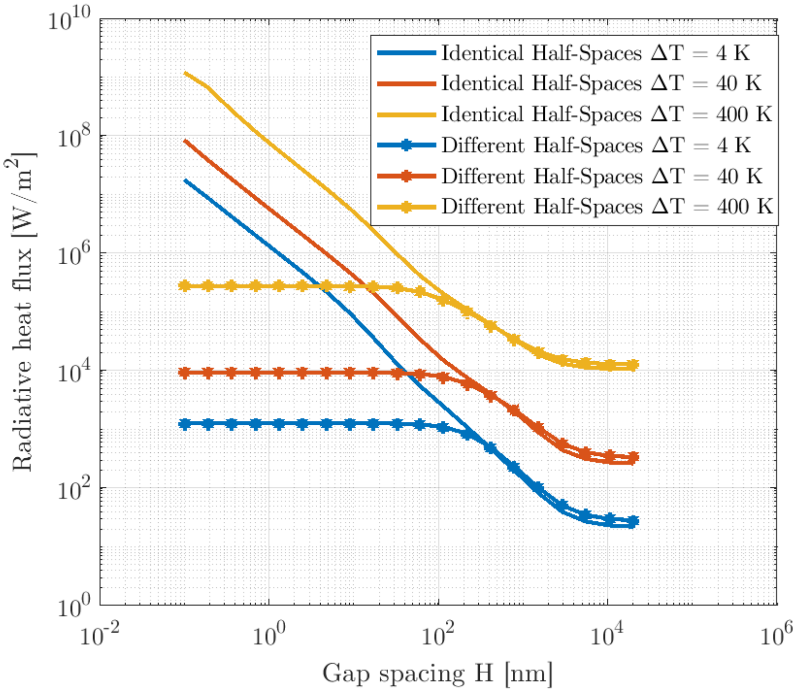

(c) Heat flux vs gap spacing

Figure 4.8: Radiative heat flux between two different and identical half-spaces at different temperatures differentials with $T_B = 298$ K

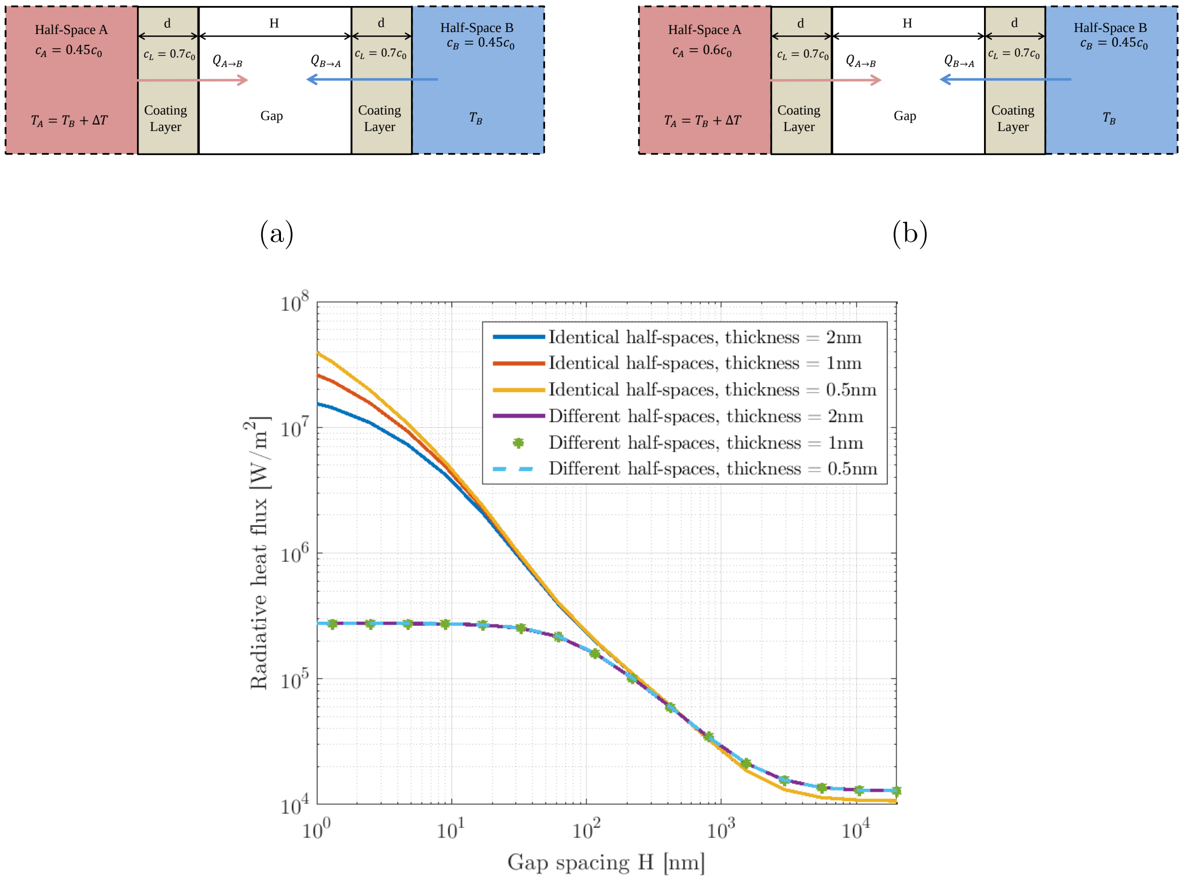

(a)

(b)

(c) Heat flux vs gap spacing

Figure 4.9: Radiative heat flux between coated and uncoated half-spaces with temperatures $T_A = 698$ K and $T_B = 298$ K

be estimated by ignoring the coating layers, which reduce the reflection coefficient of the structure to the value between the substrates without coatings.

4.3 Heat Transfer with Interference

The previous sections did not address the interference between waves generated from different half-spaces. This may compromise the accuracy of the model. We need to consider the wave nature of heat carriers. The important characteristics of waves are amplitudes, propagation directions, and phases. Consider the structure of two half-spaces A and B as in Fig. 4.1. The EM wave fields in A and B can be described by the real parts of complex-valued plane waves

$$V_\eta^\pm = \mathrm{v}_\eta^\pm e^{i(\pm x\cos\theta_\eta + y\sin\theta_\eta\cos\phi_\eta + x\sin\theta_\eta\sin\phi_\eta)\omega/c_\eta - i\omega t}, \qquad \eta = A, B, \tag{4.22}$$

where $\mathrm{v}_\eta^\pm$ are complex-valued amplitudes. According to (3.27), the amplitudes of the waves are related to their energy densities as

$$dE_\eta^\pm = \frac{1}{\mu_\eta c_\eta^2}\left(\mathrm{v}_\eta^\pm\right)^2, \tag{4.23}$$

where the energy densities for frequencies in range of $[\omega, \omega + d\omega)$, and angles in the ranges $[\theta, \theta + d\theta)$ and $[\phi, \phi + d\phi)$ are

$$dE_\eta^\pm = p^2(\omega[1 \mp q\cos\theta_\eta], T_\eta)\frac{\hbar\omega^3}{8\pi^3 c_\eta^3}\sin\theta_\eta d\phi_\eta d\theta_\eta d\omega. \tag{4.24}$$

So the amplitudes and Planck's functions are related

$$\begin{aligned} \mathrm{v}_A^\pm &= e^{i\alpha_\pm}p(\omega[1 \mp q_A\cos\theta_A], T_A)\sqrt{\frac{\mu_A\hbar\omega^3}{8\pi^3 c_A}\sin\theta_A d\phi_A d\theta_A d\omega} \\ \mathrm{v}_B^\pm &= e^{i\beta_\pm}p(\omega[1 \mp q_B\cos\theta_B], T_B)\sqrt{\frac{\mu_B\hbar\omega^3}{8\pi^3 c_B}\sin\theta_B d\phi_B d\theta_B d\omega}, \end{aligned} \tag{4.25}$$

where $\alpha_\pm$ and $\beta_\pm$ are random phase shifts. Equations (4.22) and (4.25) uniquely define the plane waves $V_A^\pm$ and $V_B^\pm$.

As shown in Fig. 4.10, a plane wave V_A^+ propagating in A towards B generates a reflected wave V_{ref}^- propagating in A and a transmitted wave V_{tran}^+ propagating in B. These waves are related to the parameters of V_A^+ as follows

$$\begin{aligned} \mathrm{v}_{\text{ref}}^- &= R_A(\omega,\theta_A)e^{i\alpha_R}\cdot\underbrace{e^{i\alpha_+}p(\omega[1 - q_A\cos\theta_A], T_A)\sqrt{\frac{\mu_A\hbar\omega^3}{8\pi^3 c_A}\sin\theta_A d\phi_A d\theta_A d\omega}}_{\mathrm{v}_A^+}, \\ \mathrm{v}_{\text{tran}}^+ &= W_A(\omega,\theta_A)e^{i\beta_W}\cdot\underbrace{e^{i\alpha_+}p(\omega[1 - q_A\cos\theta_A], T_A)\sqrt{\frac{\mu_A\hbar\omega^3}{8\pi^3 c_A}\sin\theta_A d\phi_A d\theta_A d\omega}}_{\mathrm{v}_A^+}, \end{aligned} \tag{4.26}$$

where R_A and α_R are the absolute value and the phase of the reflection coefficient from A back to A, and W_A and β_W are the absolute value and the phase of the transmission coefficient from A to B.

Similarly a plane wave V_B^- propagating in B towards A generates a reflected wave V_{ref}^+

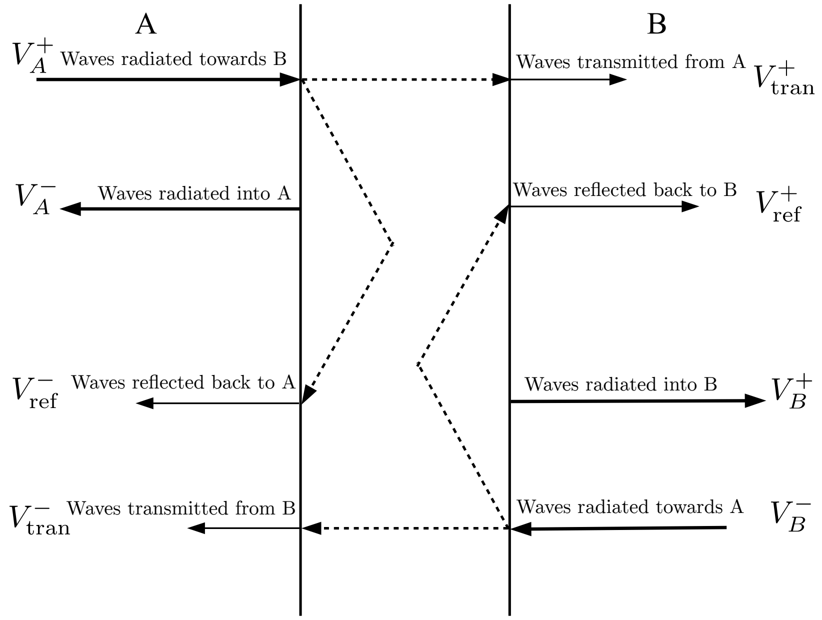

Figure 4.10: The connection between waves in A and B. Planck's law specifies waves $V_A^\pm$ and $V_B^\pm$ propagating in all directions. Also, waves V_A^+ and V_B^- radiated from A and B toward the interfaces determine fields V_A^- and V_B^+ propagating into the interiors. Therefore, V_A^- and V_B^+ are specified in two ways: directly by Planck's law, and indirectly, through V_A^+ and V_B^-. The comparison of the two specifications makes it possible to compute the compatibility conditions and the heat transport between A and B

propagating in B and a transmitted wave V_{tran}^- propagating in A:

$$\begin{aligned} \mathrm{v}_{\text{ref}}^+ &= R_B(\omega,\theta_B)e^{i\beta_R}\cdot\underbrace{e^{i\beta_-}p(\omega[1+q_B\cos\theta_B],T_B)\sqrt{\frac{\mu_B\hbar\omega^3}{8\pi^3c_B}\sin\theta_B d\phi_B d\theta_B d\omega}}_{\mathrm{v}_B^-}, \\ \mathrm{v}_{\text{tran}}^- &= W_B(\omega,\theta)e^{i\alpha_W}\cdot\underbrace{e^{i\beta_-}p(\omega[1+q_B\cos\theta_B],T_B)\sqrt{\frac{\mu_B\hbar\omega^3}{8\pi^3c_B}\sin\theta_B d\phi_B d\theta_B d\omega}}_{\mathrm{v}_B^-}, \end{aligned} \tag{4.27}$$

where R_B $(= R_A)$ and β_R are the absolute value and the phase of the reflection coefficient from B back to B, and W_B and α_W are the absolute value and the phase of the transmission coefficient from B to A. The absolute value of the reflection and transmission coefficient are related by

$$W_B^2 = \frac{c_A\cos\theta_B}{c_B\cos\theta_A}\left(1-R_A^2\right), \qquad W_A^2 = \frac{c_B\cos\theta_A}{c_A\cos\theta_B}\left(1-R_B^2\right). \tag{4.28}$$

This implies that the waves V_A^+ and V_B^- are uniquely define the waves V_A^- and V_B^+ which connects the thermodynamical parameters parameters (T_A, T_B, Q) to each other. Correspondingly, the waves propagating in A outward from B can be interpreted from two points of views: wave radiated into A, V_A^-, with amplitude (4.25), or as the superposition of V_{ref}^- and V_{tran}^-. In order for these two representations match, every such wave should satisfy the relation

$$\mathrm{v}_A^- = \mathrm{v}_{\text{ref}}^- + \mathrm{v}_{\text{tran}}^-. \tag{4.29}$$

Using (4.25)-(4.27), we can rewrite (4.29) as

$$\begin{aligned} &p(\omega[1 + q_A\cos\theta_A], T_A) + R_A e^{i\chi_-} p(\omega[1 - q_A\cos\theta_A], T_A) \\ &\qquad = W_B e^{i\psi_-} p(\omega[1 + q_B\cos\theta_B], T_B)\sqrt{\frac{\mu_B c_A}{\mu_A c_B}\frac{\sin\theta_B d\theta_B}{\sin\theta_A d\theta_A}}, \end{aligned} \tag{4.30}$$

where χ_- and ψ_- are indefinite phases. Using (4.28) and $d\left(\frac{\sin^2\theta_A}{c_A^2}\right) = d\left(\frac{\sin^2\theta_B}{c_B^2}\right)$ from Snell's law and assuming that $\mu_A = \mu_B$, we can simplify (4.30),

$$\begin{aligned} &p(\omega[1 + q_A\cos\theta_A], T_A) + R_A p(\omega[1 - q_A\cos\theta_A], T_A)e^{i\chi_-} \\ &\qquad = \sqrt{1 - R_A^2}\, p(\omega[1 + q_B\cos\theta_B], T_B)e^{i\psi_-}, \end{aligned} \tag{4.31}$$

where does not involve the differential of the frequency and angles. Hence, it must be correct for any given angle and frequency.

Equation (4.31) is obtained by assuming two representation of the waves propagating in A in the the direction outward from B. The same relation can be determined for the wave propagating in B in the direction outward of B.

$$\begin{aligned} &p(\omega[1 - q_B\cos\theta_B], T_B) + R_A p(\omega[1 + q_B\cos\theta_B], T_B)e^{i\chi_+} \\ &\qquad = \sqrt{1 - R_A^2}\, p(\omega[1 - q_A\cos\theta_A], T_A)e^{i\psi_+}, \end{aligned} \tag{4.32}$$

where χ_+ and ψ_+ are independent and indefinite phases. We see that (4.31) and (4.32) are in the form $X + Ye^{i\chi} = Ze^{i\psi}$. Then X, Y and Z in each case must satisfy the triangle inequality $|X - Y| \leq |Z| \leq |X + Y|$. So equations (4.31) and (4.32) are satisfied if and only if the pair (ω, θ_A) be in the set I_A which is defined by inequalities

$$I_A : \begin{cases} F_-(T_A, q_A; \omega, \theta_A) & \leq f(T_B, q_B; \omega, \theta_B) \leq F_+(T_A, q_A; \omega, \theta_A), \\ F_-(T_B, -q_B; \omega, \theta_B) & \leq f(T_A, -q_A; \omega, \theta_A) \leq F_+(T_B, -q_B; \omega, \theta_B) \\ \omega \in [0, \infty), & \theta_A \in [0, \theta_A^c], \end{cases} \tag{4.33}$$

where

$$F_\pm(T, q; \omega, \theta) = |p(\omega[1 + q\cos\theta], T) \pm R_A p(\omega[1 - q\cos\theta], T)|, \tag{4.34}$$

and

$$f_{\pm}(T, q; \omega, \theta) = \sqrt{1 - R_A^2} p(\omega[1 + q \cos\theta], T). \tag{4.35}$$

These conditions in (7.2) are called *compatibility conditions*. Only certain values of (ω, θ) are compatible. This means that for two half-spaces with temperatures T_A and T_B and specified q_A and q_B some waves with specific frequencies and angles are not compatible with each other, and hence are not able to transfer energy between half-spaces. Hence, the domain of integration for the first two equations in (4.9) switches from Ω_A and Ω_B to integration over sets I_A of compatible waves. Since the amplitudes of the generated waves in the A and B are related, we cannot use the third equation in (4.9) to compute the heat flux $Q_{A\to B}$ and $Q_{B\to A}$ independently by using the parameters of one domain. So we have only two equations

$$\begin{aligned} Q &= Q_{I_A}(T_A, q_A; T_B, q_B) \\ &= \sum_{\text{pol}} \int_{I_A} \hbar\omega [p^2(\omega[1 - q_A \cos\theta_A], T_A) - p^2(\omega[1 + q_A \cos\theta_A], T_A)] c_A \cos\theta_A d\Omega_A, \\ Q &= Q_{I_A}(T_B, q_B; T_A, q_A) \\ &= \sum_{\text{pol}} \int_{I_A} \hbar\omega [p^2(\omega[1 - q_B \cos\theta_B], T_B) - p^2(\omega[1 + q_B \cos\theta_B], T_B)] c_B \cos\theta_B d\Omega_B. \end{aligned} \tag{4.36}$$

If we assume that both temperatures T_A and T_B are known, then we have three unknowns parameters (q_A, q_B, Q), which determine both the integration and the domain of integration.

4.4 Solution for Radiation with Interference

We assume that T_A and T_B are known. If q_A and q_B have arbitrary values then the obtained heat flux from the two equations in (4.36) are not equal. So we need to determine q_A and q_B such that the heat flux Q is the same. So q_A and q_B are related and if we specify one, the other one can be determined. We assume that q_A is a fixed point in $[-1, 1]$ and let q_B vary. Then, the integrals in (4.36) and I_A are functions of q_B, so we compute the corresponding $q_B = q_B(q_A)$. Since in (4.36) both expressions give Q we consider

$$Q_{I_A}(T_A, q_A; T_B, q_B) - Q_{I_A}(T_B, q_B; T_A, q_A) = 0, \tag{4.37}$$

as an equation which determine q_B as function of q_A; $q_B = q_B(q_A)$. We solve this equation for q_B using an iterative algorithm explained in 4.2.1. Then we can compute the heat flux $Q = Q(q_A)$ which depends on q_A. If we apply this procedure to all q_A's in the $[-1, 1]$, we can determine the corresponding heat fluxes $Q(q_A)$ and determine the range of the admissible heat fluxes for the temperature T_A and T_B.

Since there are an interval of solutions for Q, we require some extra assumptions in order to find the heat flux for T_A and T_B. One assumption can be to choose the maximum possible Q.

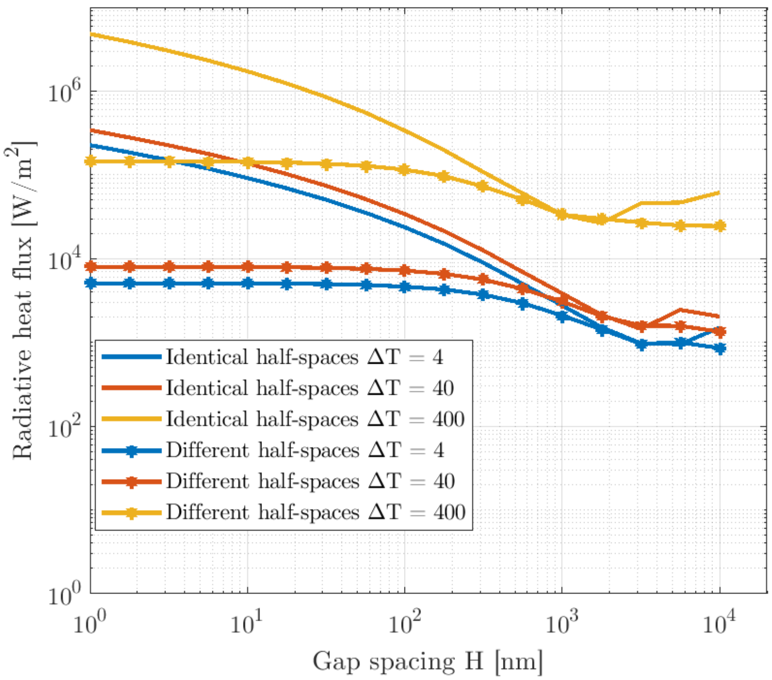

Figure 4.11: Radiative heat flux between two different and identical half-spaces at different temperatures differentials with the consideration of interference, $T_B = 298$ K

So the calculations follows procedure: 1. choose a mesh of values q_A in [-1,1], 2. solve (4.37) for $q_B = q_B(q_A)$ as a function of q_A, 3. obtain the heat flux $Q = Q(q_A)$ from any of the integral equations in (4.36), 4. choose the maximum value of Q.

For the structure Fig. 4.8a, we repeated the same simulations as the ones shown in 4.8c but this time with the consideration of the interference. In the simulations the right half-space (B) is at room temperature $T_B = 298$ K, while the temperature in A has values $4, 40, 400$ K higher. The wave speeds for identical half-spaces are set to $c_A = c_B = 0.45c_0$.

The results of the calculations are shown in Fig. 4.11 by solid lines for identical half-spaces. For spacing larger than 10μm the heat flux is constant. However, the predicted heat flux is greater than what predicted by Stefan-Boltzmann and the results from section 4.2. This indicates that for large spacings, where the interference is not important, the consideration of interference negatively affect the accuracy of our simulations. As we go to smaller spacings the curves demonstrate the divergence of the heat flux as $H \to 0$ at a rate smaller than $\dfrac{1}{H^2}$.

Fig. 4.8 also shows the results for heat flux between half-spaces with different material properties. One half-space has the wave speed $c_B = 0.45c_0$ while the wave speed of the other half-space (A) is $c_A = 0.6c_0$. The temperatures of the half-spaces are set as in the previous case: B is maintained at $T_B = 298$ K, while the temperatures of A are $4, 40, 400K$ higher.

It is observed that all the lines with stars approach horizontal asymptotes in both limiting cases of increasing and decreasing H. For small gap spacing the heat fluxes are comparable to the ones that are predicted in Fig. 4.8c. As the width of the gap increases, the lines corresponding to heat flux between the different materials does not drop significantly to lower values as predicted by the previous section (so it is not close to Stefan-Boltzmann law). These results suggest that for accurate predictions of radiative heat flux we need to combine the models with and without the interference, such that for spacings beyond the dominant wavelength of the radiation the model without the interference effect is applied while for smaller spacings the model with the interference effect applied.

Chapter 5

Phonon Conduction in Nanoscale

Here, we focus on models of heat transfer in dielectric solids caused by phonons. We first review Debye's model of phonons and then combine this model with the methods developed for the analysis of radiative heat transfer.

5.1 Debye's Model for Phonons

Solids can be modeled as systems of masses and springs where the springs simulate the interactions between molecules. Due to these interactions, molecules oscillate around their equilibrium positions.

Assume a solid consists of N molecules in a 3D space where each molecule has 3 degrees of freedom, i.e. molecules are treated as dimensionless objects without internal structures. Each molecule has the kinetic energy, and all interactions between molecules are described in terms of the potential energy.

Assume the positions of the molecules are given in Cartesian coordinates (x, y, z), and $\mathbf{x}_i \equiv (x_i, y_i, z_i)$ is the position of the i^{th} molecule. Let the potential energy of a solid with N molecules be represented by $V(\boldsymbol{\xi}_1, \ldots, \boldsymbol{\xi}_i, \ldots, \boldsymbol{\xi}_N)$, where $\boldsymbol{\xi}_i = (\xi_{i,x}, \xi_{i,y}, \xi_{i,z})$ is the displacement of the i^{th} molecule from its equilibrium position. If the displacements of molecules are small, the potential energy $V(\boldsymbol{\xi}_1, \ldots, \boldsymbol{\xi}_i, \ldots, \boldsymbol{\xi}_N)$ can be expanded in a Taylor series:

$$V = V_0 + \sum_{i=1}^{N} \sum_{\alpha \in \{x,y,z\}} \left(\frac{\partial V}{\partial \xi_{i,\alpha}}\right)_0 \xi_{i,\alpha} + \frac{1}{2} \sum_{i=1}^{N} \sum_{j=1}^{N} \sum_{\alpha,\beta \in \{x,y,z\}} \left(\frac{\partial^2 V}{\partial \xi_{i,\alpha} \partial \xi_{j,\beta}}\right)_0 \xi_{i,\alpha} \xi_{j,\beta} + \ldots, \tag{5.1}$$

where the derivatives are evaluated at the equilibrium positions $\boldsymbol{\xi}_i = (0, 0, 0)$, and V_0 is the potential energy in equilibrium. Since in equilibrium the potential V has a minimum, its first derivatives vanish as $\left(\dfrac{\partial V}{\partial \xi_{i,\alpha}}\right)_0 = 0$.

Let

$$K_{i,j,\alpha,\beta} = \left(\frac{\partial^2 V}{\partial \xi_{i,\alpha} \partial \xi_{j,\beta}}\right)_{\boldsymbol{\xi}_1 = \mathbf{0}, \cdots, \boldsymbol{\xi}_N = \mathbf{0}}, \tag{5.2}$$

be the spring constants, then by neglecting the higher order terms in (5.1) we get

$$V \approx V_0 + \frac{1}{2}\sum_{i=1}^{N}\sum_{j=1}^{N}\sum_{\alpha,\beta\in\{x,y,z\}} K_{i,j,\alpha,\beta}\xi_{i,\alpha}\xi_{j,\beta}, \tag{5.3}$$

and the corresponding Newton's equations of motion take the form

$$m_i\ddot{\xi}_{i,\alpha} + \sum_{j=1}^{N}\sum_{\beta\in\{x,y,z\}} K_{i,j,\alpha,\beta}\xi_{j,\beta} = 0, \qquad i = 1,\cdots,N, \quad \alpha = x,y,z, \tag{5.4}$$

where m_i is the mass of the i^{th} molecule.

Let (5.3) be a positive-definite quadratic form with respect to $\xi_{i,\alpha}$, then there exists new coordinates $\zeta_{i,\alpha}$ which are linearly connected with all $\{\xi_{i,\alpha}\}$, and diagonalize the potential energy as

$$V = V_0 + \frac{1}{2}\sum_{i=1}^{N}\sum_{\alpha\in\{x,y,z\}} K_{i,\alpha}\zeta_{i,\alpha}^2. \tag{5.5}$$

Consequently, the equations of motions reduce to $3N$ decoupled scalar equations.

$$m_i\ddot{\zeta}_{i,\alpha} + K_{i,\alpha}\zeta_{i,\alpha} = 0, \qquad i = 1,\cdots,N, \quad \alpha = x,y,z, \quad K_{i,\alpha} > 0. \tag{5.6}$$

Instead of using two indices, we combine them and use one index in order to enumerate the equations such that $\mathbf{u} = (u_1, u_2, u_3, \ldots, u_{3N}) = (\zeta_{1,x}, \zeta_{1,y}, \zeta_{1,z}, \ldots, \zeta_{N,x}, \zeta_{N,y}, \zeta_{N,z})$. Then we get

$$\begin{gathered} \ddot{u}_l + \omega_l^2 u_l = 0, \qquad l = 1,\ldots,3N, \\ (\omega_1, \omega_2, \ldots, \omega_{3N}) = \left(\sqrt{\frac{K_{1,x}}{m_1}}, \sqrt{\frac{K_{1,y}}{m_1}}, \sqrt{\frac{K_{1,z}}{m_1}}, \ldots, \sqrt{\frac{K_{N,x}}{m_N}}, \sqrt{\frac{K_{N,y}}{m_N}}, \sqrt{\frac{K_{N,z}}{m_N}}\right). \end{gathered} \tag{5.7}$$

The l^{th} equation describes an independent harmonic oscillator with frequency ω_l. These harmonic oscillators represent the normal modes of the collective motion of molecules. The overall motion of the system is described as a superposition of normal modes. A normal mode l can be represented as

$$q_{i,\alpha}^{(l)} = a_{i,\alpha}^{(l)} e^{-i\omega_l t}, \qquad \alpha = x,y,z, \tag{5.8}$$

in order to show the oscillation at the location of the i^{th} molecule, $\mathbf{x}_i$, due to the normal mode l, where $a_{i,\alpha}^{(l)}$ is a time independent scalar, and $q_{i,\alpha}^{(l)}$ is the displacement of the i^{th} molecule in the direction of α due to the l^{th} normal mode. Thus, this term represent the contribution of the normal mode with frequency ω_l to vibrations at the position of any molecule. If one molecule is vibrating in a certain manner due to this normal mode, then it is reasonable to assume all other molecules vibrate the same way with different phases due to the changes in their spatial position. Hence, if there is no damping in the vibrational motion of a normal mode we can use a continuous function such as a plane wave function with some wave vector $\mathbf{k}_l$, which gives the oscillations in the discrete position of the molecules, to show this phase difference. Then, we can write $a_{i,\alpha}^{(l)} = a_\alpha^{(l)} e^{\mathbf{k}_l \cdot \mathbf{x}_i}$ and have

$$q_{i,\alpha}^{(l)} = a_\alpha^{(l)} e^{\mathbf{k}_l \cdot \mathbf{x}_i - i\omega_l t}, \qquad \alpha = x, y, z, \tag{5.9}$$

where $k_l = |\mathbf{k}_l|$ is the wavenumber and it is proportional to the inverse of the wavelength $k_l = \dfrac{2\pi}{\lambda_l}$.

The displacement of the i^{th} molecule is represented as a vibrational wave by superposition of plane wave normal modes

$$\xi_{i,\alpha}(\mathbf{x}_i) = \sum_l C_\alpha^{(l)} q_{i,\alpha}^{(l)} = \sum_l C_\alpha^{(l)} a_\alpha^{(l)} e^{\mathbf{k}_l \cdot \mathbf{x}_i - i\omega_l t} = \sum_l b_\alpha^{(l)} e^{\mathbf{k}_l \cdot \mathbf{x}_i - i\omega_l t}, \tag{5.10}$$

where $C_\alpha^{(l)}$ are arbitrary constants. We can substitute (5.10) into (5.4) to get

$$-\omega_l^2 m_i \sum_l b_\alpha^{(l)} e^{\mathbf{k}_l \cdot \mathbf{x}_i - i\omega_l t} + \sum_{j=1}^{N} \sum_{\beta \in \{x,y,z\}} K_{i,j,\alpha,\beta} \sum_l b_\beta^{(l)} e^{\mathbf{k}_l \cdot \mathbf{x}_j - i\omega_l t} = 0, \tag{5.11}$$

If we have a isotropic solid where the molecules have the same mass, and the spring constants depend on the relative positions of the molecules then

$$\sum_l \left(-\omega_l^2 b_\alpha^{(l)} + \sum_{j=1}^{N} \sum_{\beta \in \{x,y,z\}} \frac{K_{i,j,\alpha,\beta}}{m} \cdot e^{\mathbf{k}_l \cdot (\mathbf{x}_j - \mathbf{x}_i)} \cdot b_\beta^{(l)} \right) e^{-i\omega_l t} = 0. \tag{5.12}$$

Let

$$\Gamma_{\alpha,\beta}(\mathbf{k}_l) = \sum_{j=1}^{N} K_{i,j,\alpha,\beta}/m e^{\mathbf{k}_l \cdot (\mathbf{x}_j - \mathbf{x}_i)}, \tag{5.13}$$

then we get

$$-\omega_l^2 b_\alpha^{(l)} + \sum_{\beta \in \{x,y,z\}} \Gamma_{\alpha,\beta}(\mathbf{k}_l) b_\beta^{(l)} = 0, \tag{5.14}$$

where in order to find ω we must solve the characteristic equation of the 3-by-3 matrix $\mathbf{\Gamma}$:

$$f(\mathbf{k}, \omega^2) = \left| \Gamma_{\alpha,\beta}(\mathbf{k}) - \omega^2 \delta_{\alpha,\beta} \right| = 0, \qquad \delta_{\alpha,\beta} = \begin{cases} 1 & \alpha = \beta, \\ 0 & \text{else,} \end{cases} \tag{5.15}$$

where we can extract the dispersion relation between the frequency and the wavenumber. For $\omega = 0$, where we have translational motion of the entire solid, the wavelength is infinite and consequently the wavenumber k is zero, which must be a solution of (5.15). So $f(\mathbf{k} =$

$\mathbf{0}, \omega^2 = 0) = 0$. Moreover, the wave vectors $\mathbf{k}$ and $-\mathbf{k}$ result in the same equation $f(\mathbf{k}, \omega^2) = f(-\mathbf{k}, \omega^2)$ as the summation in (5.13) takes into account all pairs of $(\mathbf{x}_i, \mathbf{x}_j)$. Hence

$$\frac{\partial f(\mathbf{k}, \omega^2)}{\partial \mathbf{k}}\Big|_{\mathbf{k}=\mathbf{0}} = 0. \tag{5.16}$$

Correspondingly, if we write the Taylor series around $(\mathbf{k} = \mathbf{0}, \omega^2 = 0)$, we get

$$0 = \omega^2 \frac{\partial f}{\partial\left(\omega^2\right)} - \frac{1}{2} k^2 \frac{\partial^2 f}{\partial \mathbf{k}^2}\Big|_0 . \tag{5.17}$$

From here we get

$$\omega = k \left(\frac{\frac{\partial^2 f}{\partial \mathbf{k}^2}\big|_0}{2 \frac{\partial f}{\partial(\omega^2)}} \right)^{\frac{1}{2}}, \tag{5.18}$$

which is the dispersion relation $\omega = kv$, where v is the speed of the propagation of the vibrational normal modes in the solid. The value of v depends on the direction of oscillations with respect to $\mathbf{k}$, and the frequency. There are three directions of oscillations with respect to the direction of $\mathbf{k}$ where each corresponds to a polarizations. Oscillations parallel to $\mathbf{k}$, form a wave with a longitudinal polarization with the speed v_l, and oscillations perpendicular to $\mathbf{k}$ form two transverse wave polarization with the speed v_t.

For small frequencies, v is independent of ω and the dispersion relation $\omega = kv$ becomes linear. Although the linear relation between ω and k is not valid for large frequencies, the Debye model assumes this linear relation to be true for all frequencies.

For any $\mathbf{k}$ in a 3D space we have $k^2 = k_x^2 + k_y^2 + k_z^2$; hence, there are a number of normal modes corresponding to $\mathbf{k}$. Since the plane wave from (5.9) is a solution to the equation

$$\nabla^2 u + k^2 u = 0, \tag{5.19}$$

hence based on the Weyl's asymptote, the number of normal modes for waves with the wavenumber in the interval $[k, k + dk)$ for a given polarization is $\frac{4\pi k^2 dk}{(2\pi/L)^3}$. Summing over the three polarizations of the vibrational waves and applying the dispersion relation we get

$$dN(\omega) = V \cdot \frac{\omega^2 d\omega}{2\pi^2} \left(\frac{1}{v_l^3} + \frac{2}{v_t^3} \right), \qquad V = L^3. \tag{5.20}$$

The average velocity of the waves is defined according to the equation

$$\frac{3}{v_D^3} = \frac{1}{v_l^3} + \frac{2}{v_t^3}, \tag{5.21}$$

which is the speed used in the Debye model. So we have

$$dN(\omega) = V \cdot 3 \frac{\omega^2 d\omega}{2\pi^2 v_D^3}. \tag{5.22}$$

In the Debye model, the number of modes are counted from the smallest frequency up to the frequency where the total number of vibrational modes becomes equal to the degrees of freedom of the unit volume of the considered solid. This gives the upper bound for the possible frequencies in the solid which is the Debye frequency ω_D

$$\int_0^{\omega_D} dN(\omega) = V \cdot 3 \int_0^{\omega_D} \frac{\omega^2 d\omega}{2\pi^2 v_D^3} = 3N \quad \Rightarrow \quad \omega_D = \left(6\pi^2 v_D^3 \frac{N}{V}\right)^{\frac{1}{3}}. \tag{5.23}$$

Each of the normal modes (5.7) can be treated as a quantum harmonic oscillator with the frequency ω_l which takes discrete values of energies $\epsilon_n(\omega_l) = \hbar\omega_l \left(n_l + \frac{1}{2}\right)$, where n_l is the occupation number. A vibrational wave-packet with the frequency ω_l and the energy $\hbar\omega_l$ is called a phonon. So n_l is also the number of phonons for frequency ω_l. The average energy of each quantum harmonic oscillator of frequency ω (without considering the zero-point energy) in the body in thermal equilibrium at temperature T is

$$\langle E_l \rangle = \frac{\hbar\omega_l}{e^{\frac{\hbar\omega_l}{\kappa T}} - 1}. \tag{5.24}$$

Then the energy density is the average energy of each normal mode times the density of normal modes summed over all possible frequencies.

$$E = \sum_l \frac{\hbar\omega_l}{e^{\frac{\hbar\omega_l}{\kappa T}} - 1} = \int_0^{\omega_D} \frac{\hbar\omega}{e^{\frac{\hbar\omega}{\kappa T}} - 1} \times \frac{\omega^2 d\omega}{2\pi^2 v_D^3} = \frac{3}{2} \int_0^{\omega_D} \frac{\hbar\omega}{e^{\frac{\hbar\omega}{\kappa T}} - 1} \frac{\omega^2}{\pi^2 v_D^3} d\omega \tag{5.25}$$

where the only differences between the energy density for phonons and EM waves given in (3.41) are the upper bound on the frequency and the number of polarizations.

5.2 Numerical Solutions for Phonon Conduction

Computations of heat transfer by vibrational waves are similar to computations of heat radiation. The main difference is in the values of the reflection coefficients and other parameters, e.g. wave speeds. As opposed to EM waves which propagate in vacuum better than anywhere else, acoustic waves can propagate across only very narrow vacuum gaps. Thus, when the gap between materials is small, the van der Waals (vdW) forces to couple molecular vibrations of different bodies. The calculation of the reflection coefficient for vibrational waves in any layered structure is presented in [59]. The reflection coefficient of a narrow vacuum gap is estimated in [61].

Because of the short wavelength of acoustic waves in solids, thin plates of few microns or higher thickness can be treated as half-spaces. Assume two material plates, A and B, have the mass densities ρ_A and ρ_B, and the average speeds of vibrational waves in them are v_A and v_B, respectively. If A and B are separated by a vacuum gap of the width H, where H is much larger than the wavelength of the vibrational waves on surfaces of the half-spaces, the reflection coefficient of the wave with the incident angle θ_A is determined by the expression

$$|R_A| = |R_B| = \left| \frac{C(\rho_B c_B \cos\theta_A - \rho_A c_A \cos\theta_B) + i\omega H^4 \rho_A c_A \rho_B c_B}{C(\rho_B c_B \cos\theta_A + \rho_A c_A \cos\theta_B) + i\omega H^4 \rho_A c_A \rho_B c_B} \right|, \tag{5.26}$$

where

$$C \equiv C(\omega, H) = \frac{A^*}{2\pi}\left(1 - \nu\omega^2 H^2 \frac{\sin^2\theta_A}{c_A^2}\right), \tag{5.27}$$

where A^* is the Hamaker constant [62], the pairs of (ρ_A,c_A) and (ρ_B, c_B) are the density and averaged speeds of the waves in each medium respectively, [61].

Using this reflection coefficient along with the reflection coefficients of the other interfaces we obtain the reflection coefficient for a layered structure by the method discussed in [61].

The transmission coefficient W is defined by the reflection coefficient

$$|W_A|^2 = \frac{\rho_B c_B \cos\theta_A}{\rho_A c_A \cos\theta_B}(1 - |R_B|^2), \qquad |W_B|^2 = \frac{\rho_A c_A \cos\theta_B}{\rho_B c_B \cos\theta_A}(1 - |R_A|^2). \tag{5.28}$$

In the limiting case of $H = 0$ the reflection coefficient of a vacuum gap simplifies to the reflection coefficient for direct contact between A and B.

$$R_A = -R_B = \frac{\rho_B c_B \cos\theta_A - \rho_A c_A \cos\theta_B}{\rho_B c_B \cos\theta_A + \rho_A c_A \cos\theta_B}. \tag{5.29}$$

The equations for heat flux by phonons are similar to those for radiation in chapter 4

$$\begin{cases} Q = Q_{\Omega_A}(T_A, q_A), & \Omega_A \in [0, \omega_D] \times [0, \theta_A^c] \times [0, 2\pi], \\ Q = Q_{\Omega_B}(T_B, q_B), & \Omega_B \in [0, \omega_D] \times [0, \theta_B^c] \times [0, 2\pi], \\ Q = Q_{A\to B}(T_A, q_A) - Q_{B\to A}(T_B, q_B), \end{cases} \tag{5.30}$$

where ω_D is the smaller of the Debye frequencies of the media A and B; $\omega_D = \min\{\omega_{D,A}, \omega_{D,B}\}$. The Debye frequency for each medium can be determined using the Debye temperature T_D by $\omega_{D,\eta} = \dfrac{\kappa T_{D,\eta}}{\hbar}$ for $\eta = A, B$. Then (5.30) can be solved using an iterative algorithm as presented in section 4.2.1.

The graphs is Fig. 5.2 show HTC as a function of gap spacing for phonon conduction in a layered structure from reference [61]. At around 2nm the vdW forces start to become significant and we expect to see a decrease in the reflection coefficient as we go to smaller spacings as shown in Fig. 5.1 for identical Al half-spaces. Hence, it is expected that the HTC enhances as the gap spacing becomes smaller than 4nm since the dominant wavelength of the energy spectrum for vibrational waves, at room temperature, is around 2-4nm. This is also shown in Fig. 5.2 for half-spaces with and without thin coating layers. The coating layers of a few nanometers can reduce the HTC between layers.

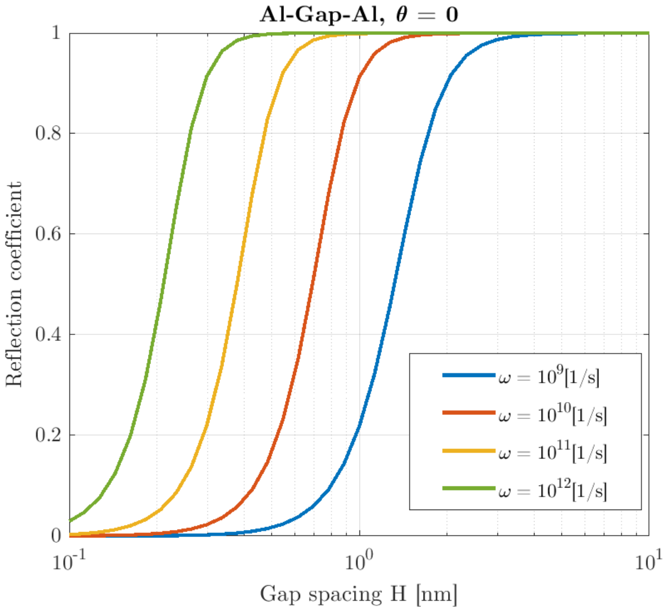

Figure 5.1: The reflection coefficient of phonons vs gap spacing between two identical Al half-spaces for four frequencies

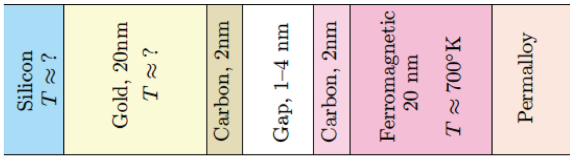

(a) Two multilayered half-spaces with a gap in between

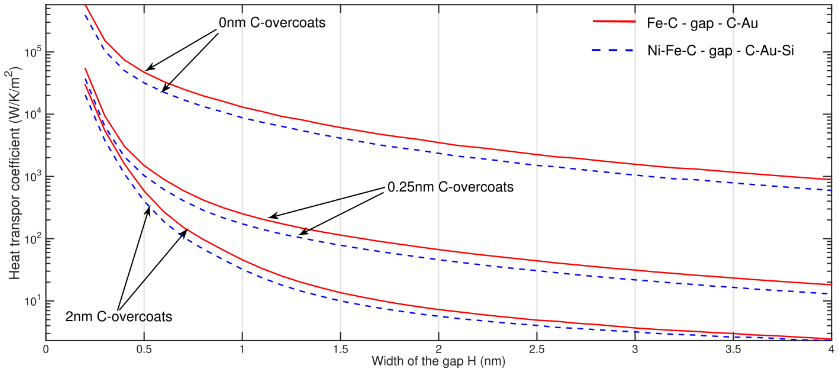

(b) Phonon conduction HTC vs gap spacing

Figure 5.2: Heat transfer by phonon conduction [61], figure (a) shows the multilayered half-spaces and the gap in between, figure (b) shows the heat transfer coefficient as a function of the gap spacing between the half-spaces for small heat fluxes, in these results the wave interference effect is neglected

Material	Si	Fe	Au	Al	AlMg	glass	Al_2O_3	C
Speed [m/s]	6354	3125	3240	3461	5105	4142	7133	11762
Density [kg/m^3]	2330	7850	19700	2700	2660	2220	3980	3500
ω_D [10^{12}/s]	845.34	61.53	22.25	60.69	60.69	37.96	117.9	291.9

Table 5.1: Material properties which are used in the calculations of phonon conduction heat transfer

Using our computational model from chapter 4, the phonon conduction between a silicon half-space (A) and iron half-space (B) with the material properties in Table 5.1 is calculated for the right half-space (B) at room temperature $T_B = 298$ K and the temperatures of A have values $\Delta T = 4, 40, 400K$ higher. The gap thickness varies from 10 nm to 0.1 nm. The results are shown in Fig. 5.3. The dashed lines are for the case with no coating layers on A and B while the solid lines are computed in the presence of 2 nm coating layers on A and B. The results show that the phonon conduction in the presence of a vacuum gap is only significant when the spacing between the materials is of the order of a few nanometers. Also the heat flux reaches a constant value for the spacing smaller than 0.3nm indicating the contact has occurred and the heat flux cannot increase further due to the resistance between the materials at contact. Fig. 5.3 also shows that the existence of the coating layers slightly decreases the heat flux.

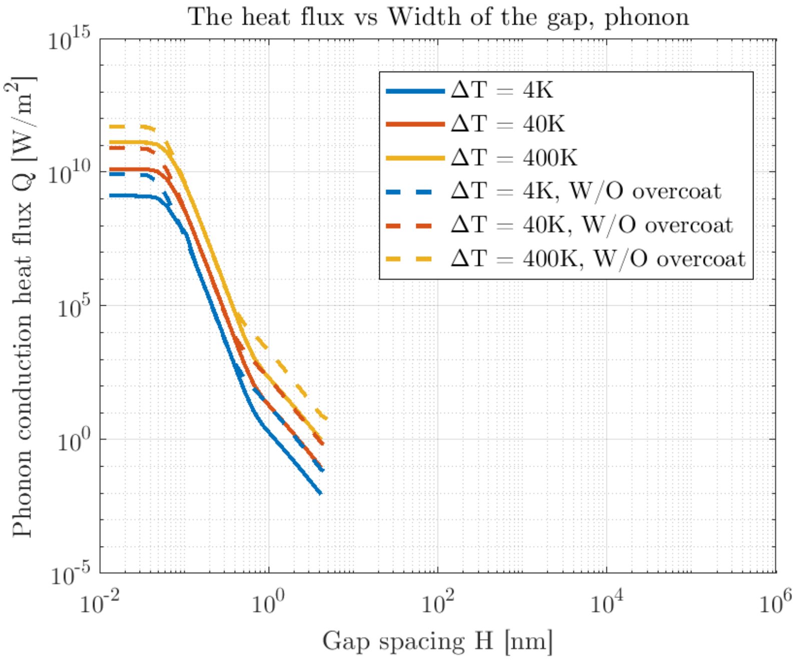

Figure 5.3: Phonon conduction heat flux between coated and uncoated silicon and iron half-spaces for small and large temperature differences, in these results the wave interference effect is neglected

5.3 Radiation and Phonon Conduction Combined

After calculation of heat transfer by radiation and by phonon conduction, it is informative to determine the total heat flux from radiation and phonon conduction combined. Assuming that these two modes of heat transfer are independent we conclude that the total heat flux appears as the sum of the heat fluxes from the radiation and conduction. Fig. 5.4 shows the total heat flux as a function of spacing for two half-spaces with and without coating layers. It can be seen that for H greater than about 10 μm the constant heat flux corresponds to the Stefan-Boltzmann law. As the spacing drops below 10 μm the heat flux increases due to radiation until the spacing is about 50 nm. At spacings below 50 nm most of the EM waves are not affected by the vacuum gap. Any further decrease in the spacing does not increase the radiative heat flux. So at the spacing larger than 10 nm and smaller that 10 μm the enhanced radiation is the dominant mode of heat transfer. As the spacing shrinks below 10 nm the heat flux from vibrational waves increases rapidly, which makes the phonon conduction the dominant mode of heat transfer.

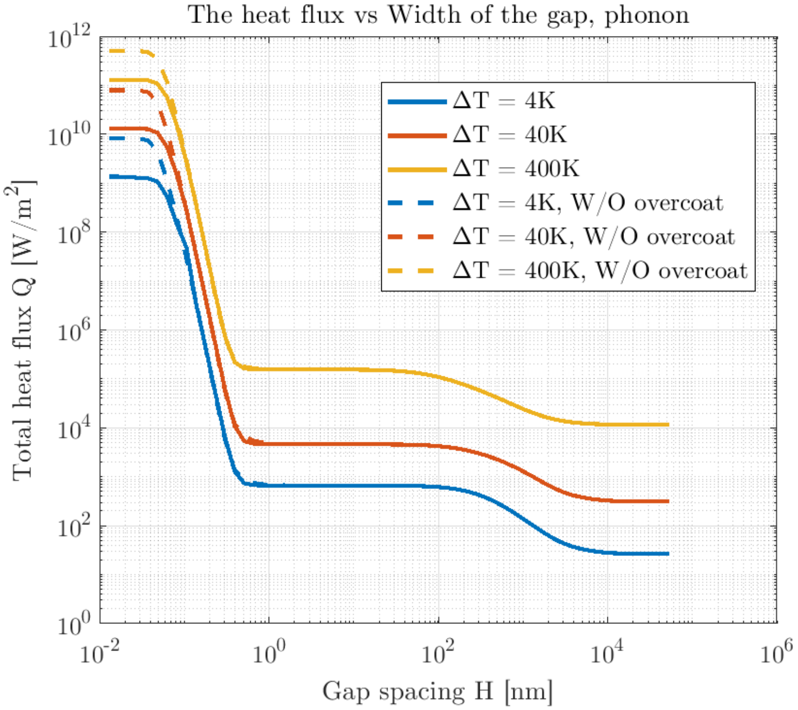

Figure 5.4: The overall heat flux due to the radiation and phonon conduction for coated and uncoated silicon and iron half-spaces for small and large temperatures differences, in these results the wave interference effect is neglected

5.4 Solution for Phonon Conduction with Interference

The interference of phonons in layered structures is described by compatibility conditions similar to those in (7.2) for radiation. We use the formula and algorithms presented for radiation in 4.3 and 4.4 to obtain the HTC due to phonon conduction for small gaps in multilayered structures are utilized in the HDD industry. The head component is typically made of alumina (Al_2O_3) while the disk substrate material can be glass, silicon (Si), or aluminum magnesium (AlMg). In addition the structures may have protective carbon coating layers.

The goal is to model an experiment that was performed using the thermal flyheight control feature of the head that can control the gap from 20 nm down to contact. The disk is assumed to be at room temperature (298 K) while the temperature of the head is assumed to be higher. We investigate the heat transfer under these conditions and determine how the HTC depends on the spacing, ΔT, coating layers and the disk's material.

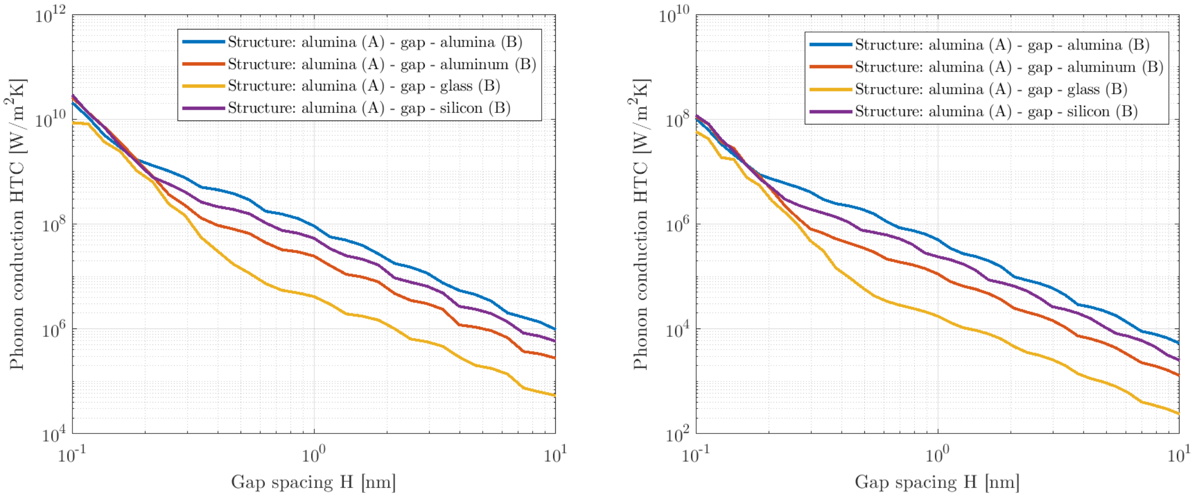

(a) $\Delta T = 0.1$ K (b) $\Delta T = 400$ K

Figure 5.5: The phonon conduction HTC between an alumina head (as half-space A) and various disk materials (as half-spaces B) vs H, the temperature of the head is $T_B = 298$ K, the wave interference is considered in these calculations

In Figs. 5.5 the HTC as a function of gap spacing is plotted for $\Delta T = 0.1$ K and $\Delta T = 400$ K for $T_B = 298$ K. We see that for identical half-spaces (Al_2O_3-Gap-Al_2O_3), the HTC is greater compared to the case with different half-spaces for the same temperature difference.

In Figs. 5.6, the heat flux between an alumina half-space and various materials (silicon, glass, and aluminum) are shown. These figures compare the heat flux for the cases with and without coating layers. According to the our model, the carbon coatings significantly reduce the heat flux for $\Delta T = 400$ K to the point that it is comparable to the heat flux for $\Delta T = 0.1$ K between half-spaces with no coating layers. These results were used in [63, 64] to compare the experiments with numerical simulations.

Figs. 5.7 show the computed values of HTC of the system of two half-spaces and a gap between them as a function of the spacing H, the temperature difference ΔT, and the temperature of the disk T_0. We see that the dependence of HTC on H, ΔT, and T_0 can be represented by

$$\text{HTC} = C \cdot H^{a_1} \cdot \Delta T^{a_2} \cdot T_0^{a_3}, \tag{5.31}$$

where parameters a_1, a_2, a_3, and C depend on the frequency and material properties of the head and the disk. Using this fitting for previously determined solutions we can promptly determine the HTC for any condition of the problem. In [65] the above results were compared with experimental results.

In summary, in this section we adopted the numerical model from section 4.4 of heat transfer by phonons. It was applied to various multilayered structures. The effects of material

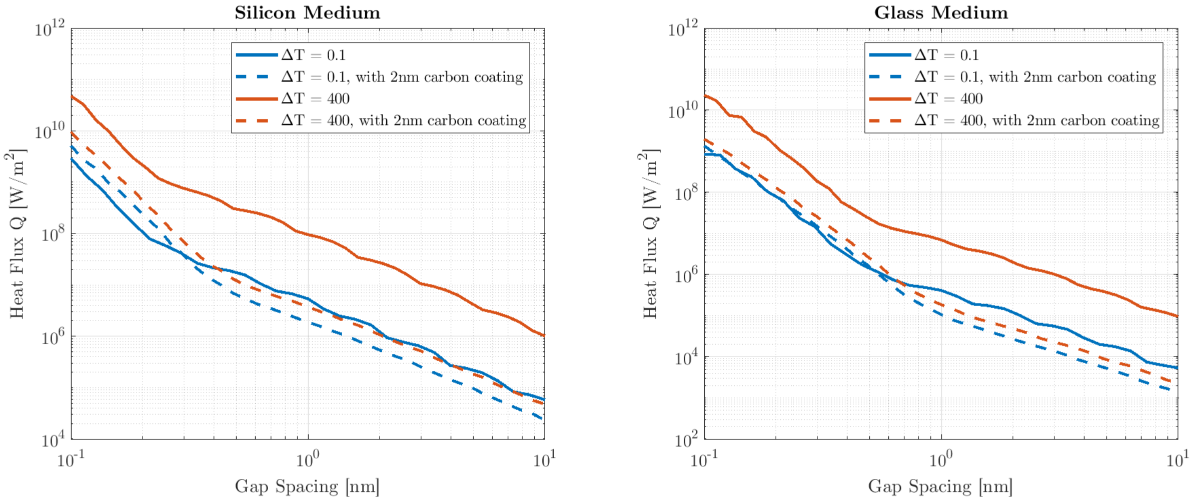

(a) The computed HTC vs H for a silicon disk and alumina head (half-space)

(b) The computed HTC vs H for a glass disk and alumina head (half-space)

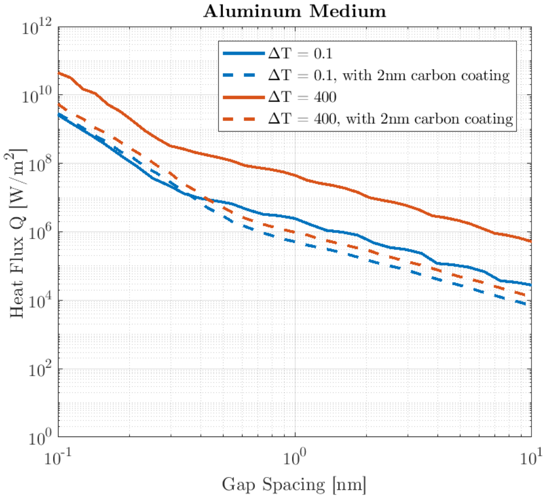

(c) The computed HTC vs H for an aluminum disk and alumina head (half-space)

Figure 5.6: The phonon conduction HTC between an alumina half-space (A) and various materials as the half-spaces B vs H and the comparison with the presence of carbon coating layers on the half-spaces, the wave interference is considered in these calculations

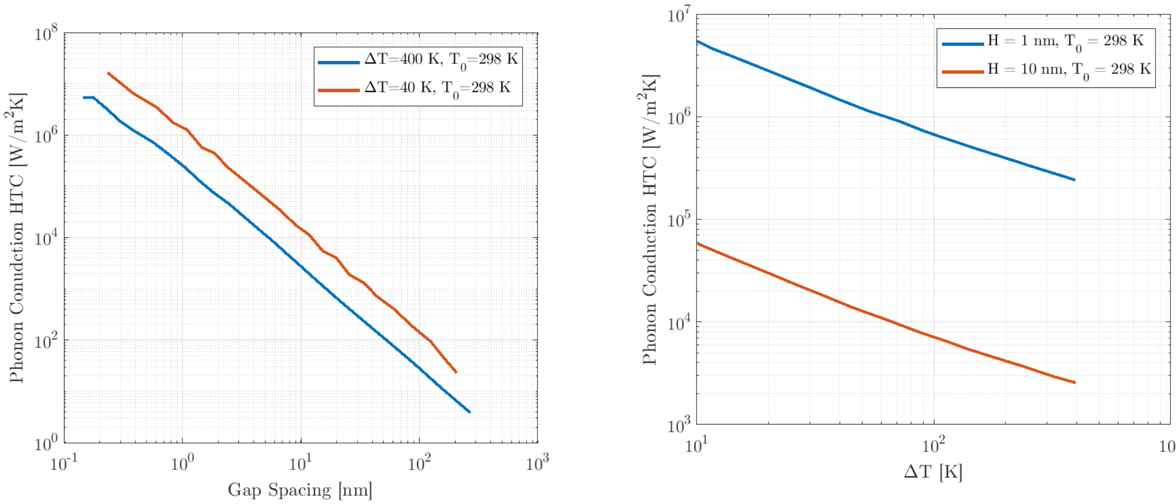

(a) The HTC vs H while ΔT and T_0 are constant

(b) The computed HTC vs ΔT while H and T_0 are constant

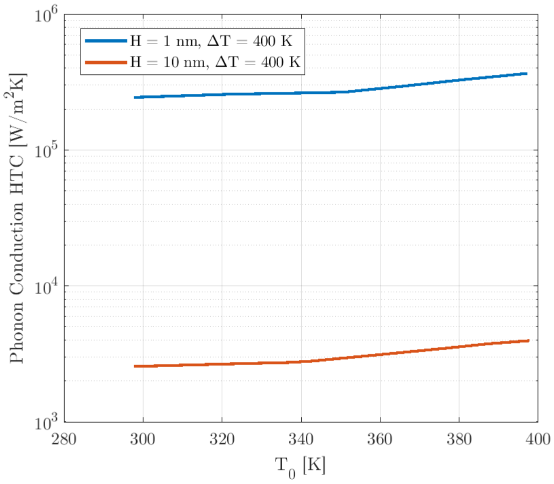

(c) HTC vs T_0 while ΔT and H are constant

Figure 5.7: The phonon conduction HTC between an alumina half-space and silicon half-space as a function of each of H, ΔT, and T_0 when the wave interference is considered. These curves are obtained to show a linear relation between the HTC and each of parameters H, ΔT, and T_0 while the other two parameters are fixed

properties of different coating were investigated.

Chapter 6

Radiation from Absorbing Materials

6.1 Wave Speed in Absorbing Materials

So far Planck's law has been used to describe the thermal radiation from a black body as well as from transparent materials with a constant wave speed. However, it is not straightforward to describe thermal radiation from absorbing materials. The derivation of Planck's law for transparent materials is based on the decomposition of EM fields into normal modes which are countable using the number density function $dn(\omega) = D(\omega)d\omega = \frac{k^2(\omega)dk(\omega)}{2\pi^2}$ which represent the number of normal modes within the interval $(\omega, \omega + d\omega)$. For transparent materials the wavenumber and the frequency are related by $k(\omega) = \omega/c$, where the speed of light c in the transparent medium is constant, which implies $dn(\omega) = \frac{\omega^2}{2\pi^2 c^3}d\omega$. In the case of a frequency dependent speed $c(\omega)$, the expression for $dn(\omega)$ is slightly more complex

$$dn(\omega) = \frac{\omega^2}{2\pi^2 c^2(\omega)} d\left(\frac{\omega}{c(\omega)}\right) = \frac{\omega^2 d\omega}{2\pi^2 c(\omega)^2 v(\omega)}, \tag{6.1}$$

where

$$v(\omega) = 1 \bigg/ \frac{d\left(\omega/c(\omega)\right)}{d\omega}, \tag{6.2}$$

is the group speed of EM waves in the medium.

The conventional expression for the phase speed of light in materials is

$$c(\omega) = \frac{c_0}{n(\omega)}, \tag{6.3}$$

where n is the refractive index of the medium. In real materials, the refractive index is a complex-valued function of the frequency $n(\omega) = n'(\omega) + in''(\omega)$, where n'' describes the rate of energy dissipation. For real materials, we cannot use (6.3) to calculate the Planck distribution function since $dn(\omega)$ becomes a complex number which does not have physical meaning of the number of states.

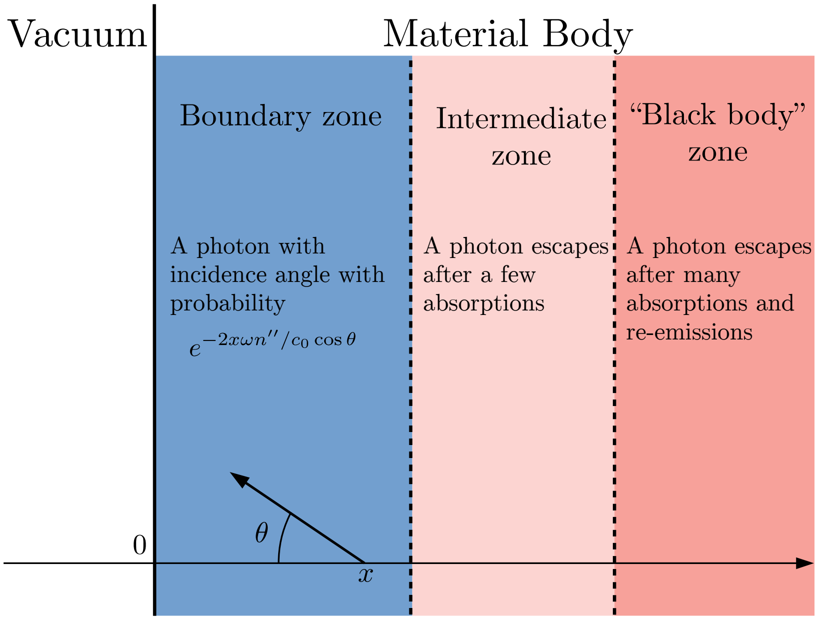

Figure 6.1: Different zones of speed for photons near the boundary of a half-space

As discussed in [66], the speed in (6.3) has a different physical meaning from the speed that is used in the computation of $dn(\omega)$ for Planck's law. The speed in (6.3) describes the propagation of EM signals inside a material, while (6.1) represent the number of normal modes which may include none propagating standing waves for materials. In [66] this problem is resolved by the introduction of a different expression for the speed of thermally radiated waves inside the material. It is proposed that the speed of thermally excited waves deep inside any absorbing materials is defined by the formula

$$c_*(\omega, T) = \frac{c_0}{e^{-\hbar\omega/\kappa T} + 1}. \tag{6.4}$$

which is independent of the material and is completely determined by the frequency and the temperature of the medium.

Furthermore, it is proposed that the speed of photons, close to the boundary of a half-space material facing vacuum, depends on the complex refractive index, frequency, temperature, direction of propagation and the distance from the material's surface. As shown in Fig. 6.1, for a photon at the distance x from the surface with the angle θ between the direction of the wave and the normal to the surface at x,

$$c(\omega, \theta, x, T, n', n'') = \frac{c_0}{n'} e^{-2\omega n'' x/c_0 \cos\theta} + c_* \left(1 - e^{-2\omega n'' x/c_0 \cos\theta}\right), \tag{6.5}$$

where $x/\cos\theta$ is the path needed for the ray to hit the boundary.

6.2 Radiation From the Surface of an Absorbing Material

Assume an absorbing half-space with a temperature T is exposed to a vacuum half-space. The thermally excited waves propagate in all directions inside the material. As the time passes, some waves with some arbitrary frequency ω reach the interface, after which they split into reflected waves and waves transmitted to vacuum. The propagation direction in the vacuum is specified by the angle θ_0, Fig. 6.2, where θ_0 is the angle of the transmitted waves and it can vary from 0 to $\pi/2$. These waves carry some of the energy from the half-space to the vacuum. The transmitted waves propagate in all directions in vacuum and they are identified by their frequency ω and their transmitted angle θ_0 with the pair (ω, θ_0).

Assuming that the energy loss of the half-space is getting replaced to keep the temperature of the half-space constant, we are interested in obtaining the heat flux from the half-space to the vacuum. We determine the distribution of thermally excited waves which are generated inside the material. We identify the emitted thermally excited waves which reach the interface in a time interval Δt using ray-tracing methods [67, 68]. There are many emitted waves inside the medium at different depth that when they reach the interface and pass to the vacuum they correspond to (ω, θ_0); we call this set of waves as the set $\mathbb{I}(\omega, \theta_0)$, we compute the heat flow during the time Δt to obtain the set $\mathbb{I}(\omega, \theta_0, \Delta t)$. Eventually, an integration over all (ω, θ_0) determines the total heat transfer to the vacuum.

Based on Snell's law $\mathbb{I}(\omega, \theta_0, \Delta t)$ have ω and θ_0 as frequency and incident angle on the interface. In order to determine $\mathbb{I}(\omega, \theta_0, \Delta t)$, let an EM wave with (ω, θ_0) travel in vacuum toward the interface. The waves in $\mathbb{I}(\omega, \theta_0, \Delta t)$ travel on the same path inside the material as the path traveled by an incident wave with (ω, θ_0). But the waves in $\mathbb{I}(\omega, \theta_0, \Delta t)$ have different origin points and arrival times to the interface.

In order to find the path which is traveled by the emitted waves, break the Δt into small time fractions of t_is with t_0 as the starting time.

$$\{t_0, t_1, \cdots, t_l\}, \qquad \Delta t = t_l - t_0, \quad t_0 = 0, \quad l \text{ is arbitrary.} \tag{6.6}$$

We assume that during each time block, i.e. $[t_i, t_{i+1}]$ in Fig. (6.2), the speed and angle of propagation are constant. We trace the waves arriving on the interface using ray-tracing to determine the angle of the waves θ_i and the depth x_i at each time steps as follows

$$\begin{cases} c_{i+1} = c\left(\omega, \theta_i, x_i, T, n', n''\right), \quad \text{from (6.5)} \\ \text{Find} \quad \theta_{i+1} \quad \text{from} \quad \dfrac{\sin\theta_{i+1}}{c_{i+1}} = \dfrac{\sin\theta_0}{c_0}, \\ x_{i+1}(\theta_0) = x_i + c_{i+1} \cdot (t_{i+1} - t_i) \cdot \cos\theta_{i+1}(\theta_0), \end{cases} , \qquad i = \{0, 1, ..., n\}, \tag{6.7}$$

where c_0 and θ_0 are known and $x_0 = 0$ and $t_0 = 0$. So for any t_i we have θ_i, c_i and x_i. Thus, we have $\mathbb{I}(\omega, \theta_0)$, where we know that for waves with frequency ω which are generated in depth x_i only waves with angle θ_i transfer energy to the vacuum with θ_0.

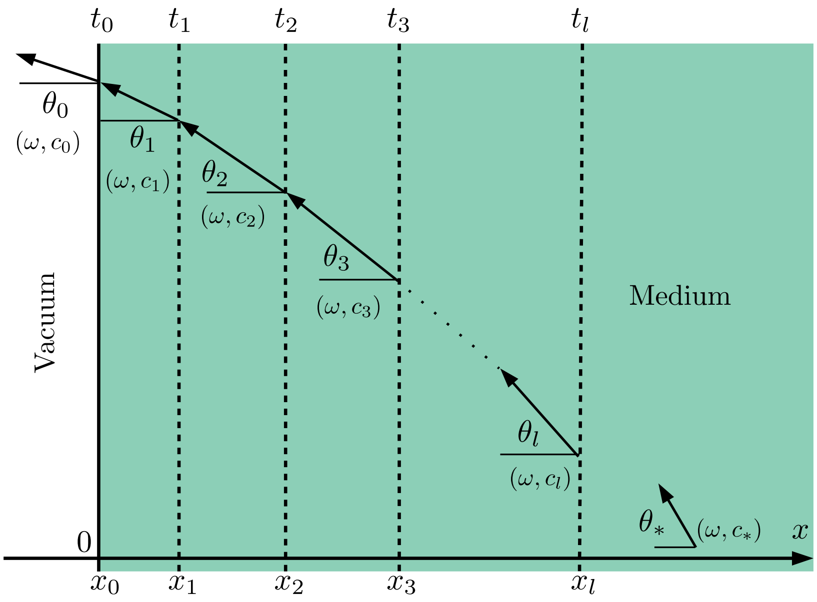

Figure 6.2: The path of a wave or photon in an absorbing material from the origin until exit

Since all the waves that exist inside the obtained depth reach to the surface in a time less than Δt they contribute to the heat transfer. So the total energy transfer is obtained from the summation of the energy of each hypothetical layer between x_i and x_{i+1} with constant properties. The total energy transfer from each layer with a constant speed is

$$E_i \cdot (1 - |R_i|^2) \cdot (\Delta x_i), \qquad \left[\frac{J}{m^2}\right], \tag{6.8}$$

where R_i is the reflection coefficient of a wave reaching the surface from the depth x_i with angle $\theta_i(\theta_0)$, and $\Delta x_i = x_i - x_{i-1}$. E_i is the energy density of waves with the angles in the range of $[\theta_i(\theta_0), \theta_i(\theta_0 + \Delta\theta_0)]$ and frequencies in the range of $[\omega, \omega + \Delta\omega]$ $(\Delta\theta_i(\theta_0) = \theta_i(\theta_0 + \Delta\theta_0) - \theta_i(\theta_0))$, which can be represented as the average energy of normal modes in temperature T from Planck's law times the number density of normal modes as we calculated in chapter 3,

$$E_i(\omega, \theta_0) = \frac{\hbar\omega}{e^{\hbar\omega/\kappa T} - 1} \times \frac{\omega^2}{4\pi^2 c_i^3} \sin\theta_i(\theta_0)\Delta\theta_i(\theta_0)\Delta\omega, \qquad \left[\frac{J}{m^3}\right]. \tag{6.9}$$

So the total heat flux in the direction of θ_0 with frequency ω is represented by the sum of the energies transferred from all the depths divided by Δt

$$Q(\omega, \theta_0) = \frac{1}{\Delta t} \sum_{i=1}^{n} E_i(\omega, \theta_0) \cdot (1 - |R_i(\omega, \theta_0)|^2) \cdot \Delta x_i(\omega, \theta_0), \qquad \left[\frac{W}{m^2}\right]. \tag{6.10}$$

Now we sum over ω and θ_0.

$$Q = \frac{1}{\Delta t} \sum_{i=1}^{n} \sum_{j=1}^{n_\theta} \sum_{k=1}^{n_\omega} E_i(\omega_k, \theta_{0j}) \cdot (1 - |R_i(\omega_k, \theta_{0j})|^2) \cdot \Delta x_i(\omega_k, \theta_{0j}), \qquad \left[\frac{W}{m^2}\right], \tag{6.11}$$

where n_θ and n_ω are the number of points which were chosen to discretize the angle and the frequency interval respectively. Hence, (6.11) determines the heat flux from the half-space.

6.3 Results

First we check the validity of the calculations by determining if the model retrieves the solution for a black body. A black body half-space follows the Stefan-Boltzmann law (σT^4) for radiation. Since a blackbody is a prefect absorber and the imaginary part of its refractive index would be infinite, the speed inside the black body is uniform and equal to the speed of photons from (6.4) deep inside any absorbing material

$$c_{\mathrm{BB}} = \frac{c_0}{e^{(-\hbar\omega/kT)} + 1}. \tag{6.12}$$

Using this speed, it is straightforward to compute the heat flux from (6.11) . In Fig. 6.3, we show a schematic of a black body half-space and the vacuum and the heat flux for black body radiation. The computational results closely matches the Stefan-Boltzmann law for radiation. As the temperature increases the difference between the solutions become more apparent.

For real materials the amount of radiation is less than a black body at the same temperature. The ratio of a real material radiation to black body radiation is defined as emissivity ϵ.

$$\epsilon = \frac{Q_{\text{real}}}{Q_{\text{black body}}} \tag{6.13}$$

The emissivities of various materials are available in the literature. Hence, we can compute the radiation of a particular material by its emissivity and the radiation for a black body at the same temperature. We are interested in determining the radiation from a real material provided by our model and comparing the results with that determined by emissivity of grey body.

For real materials the complex refractive indices and extinction coefficients are functions of frequency as shown in appendix B from [69]. Using these material properties we computed the radiative heat flux from the half-spaces as a function of temperature and plotted them along with the estimates from emissivity considerations for materials (Fig. 6.4). We start from low emissivity materials.

For liquid mercury the heat flux from simulation (solid blue curve) is larger than heat flux computed with the emissivity $\varepsilon = 0.1$ (dashed blue curve).

For gold the emissivity varies from 0.025 to 0.47 depending on the smoothness of the surface. For a polished surface $\varepsilon = 0.025$. We assume that for gold with unknown surface

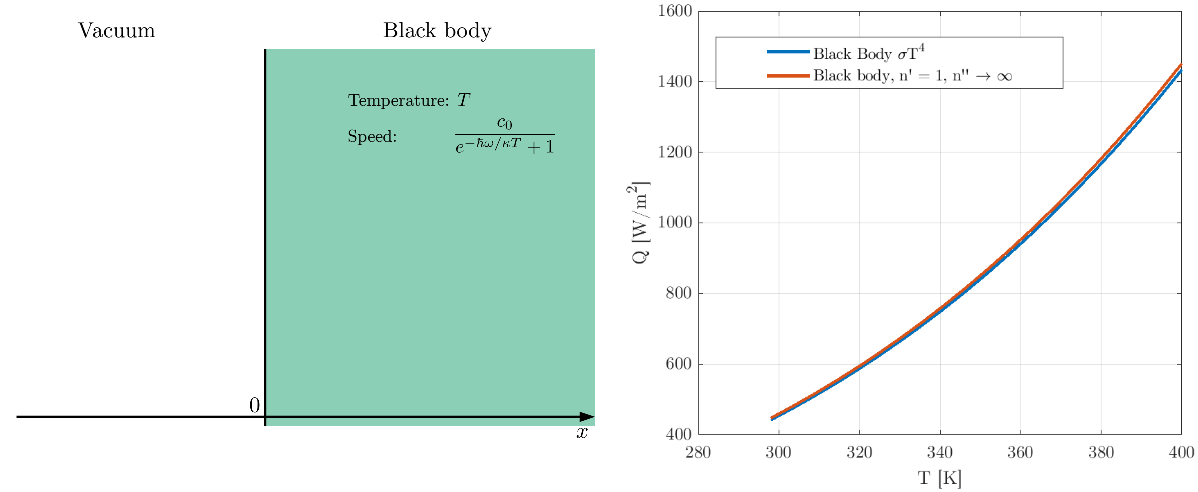

(a) A black body half-space with known temperature and properties

(b) The radiative heat flux from a black body by computations and the Stefan-Boltzmann law

Figure 6.3: Radiative heat flux for a black body half-space, (a) A black body half-space with known temperature and properties, (b) The radiative heat flux from a black body computed by the speed model from (6.5) with $n' = 1$ and $n'' \to \infty$ for the numerical computations and the radiative heat flux obtained from the Stefan-Boltzmann law

characteristics $\varepsilon = 0.2$. As we see in Fig. 6.4, the heat fluxes obtained by simulation and by direct computations using emissivity are in a good agreement (The solid yellow curve and the dashed yellow curve).

The next material is iron with an emissivity $\varepsilon = 0.44$. In this case, the curves do not perfectly match each other, but they are close (the solid red curve and the dashed red curve).

The radiation curves for silica are almost identical as the solid purple curve and the dashed purple curve are indistinguishable from each other. In this case the emissivity is $\varepsilon = 0.79$ which indicates we are getting closer to a black body.

In Fig. 6.4, we show the computations for materials ranging from small emissivity to high emissivity. It is clear that our model accurately predicts that the heat flux proportionally increases as we move from low emissivity materials to high emissivity materials.

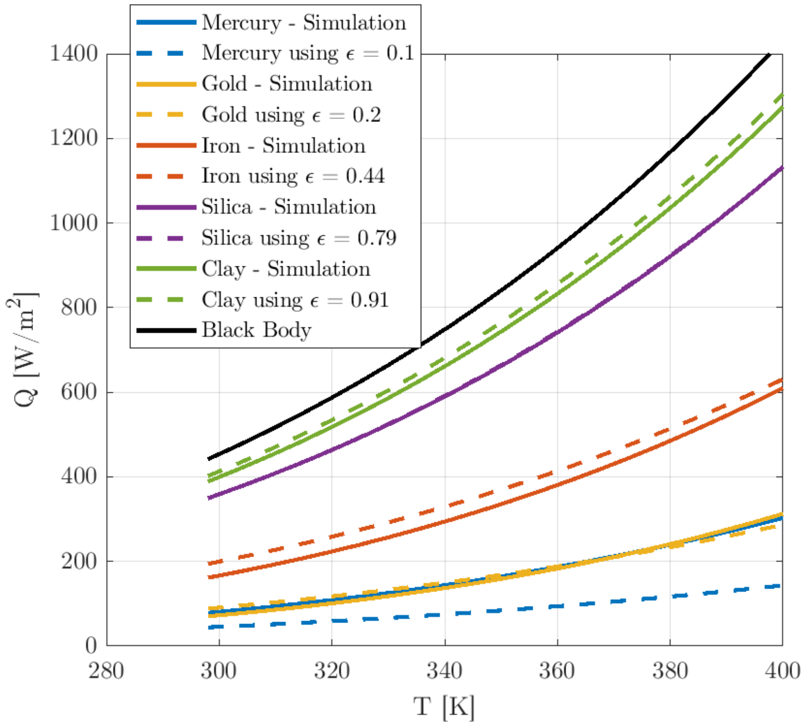

Figure 6.4: Radiative heat flux from a material half-space to the vacuum as a function of temperature, the numerical computations are shown by solid lines where the speed model from this chapter is used in the calculation of the speeds, the dashed lines are obtained from grey material assumption

Chapter 7

Unified Emission Fields

7.1 Introduction

In the previous chapters, we computed the radiative heat flux and phonon conduction between two bodies by considering distributions of the thermally excited waves for each body where the distributions of these fields depend on each other. These distributions in each domain (A and B) are functions of the temperatures (T_A, T_B), as well as of the coefficients q_A and q_B. Additionally, these two fields need to satisfy certain compatibility conditions.

In this chapter, we present a unified field that can describe the thermally excited waves in both domains by only one temperature T_f and one coefficient $\mu_f = q_f \cos\theta_A$ in the modified Planck distribution function. As opposed to T_A and T_B, T_f is not a measurable temperature, and it needs to be defined and determined such that the new distribution with the parameters of the field completely determines the distribution.

In what follows, we introduce the unified emission field concept and the conditions it needs to satisfy to determine its parameters. Then we present an algorithm to solve the heat transfer problem in layered structures. We apply this to both radiation and phonon conduction and show the results.

7.2 The Concept of Unified Field

Consider the two half-spaces A and B shown in Fig. 7.1. Let thermal radiation or phonon conduction be the only mechanisms of heat transfer between them. Assume that in a steady state condition, the field in both bodies has the distinctive parameters T_f and q_f. The temperature of the field is denoted by T_f which can be different than the actual measured temperature of either of the half-spaces. The coefficient $q_f \in [-1, 1]$ determines the deviation of the field from equilibrium. Then, parameters of the field (T_f, q_f) determine the net heat

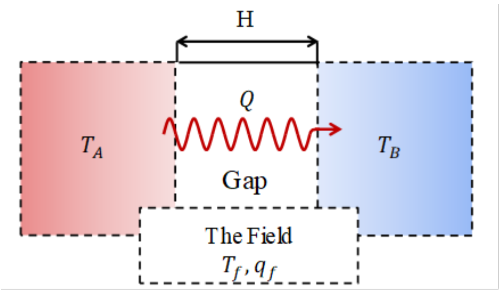

Figure 7.1: Two half-spaces with a unified emission field which is present in the entire media and describe the distribution of the emission in both half-spaces

flux between A and B,

$$Q(T_f,q_f) = \sum_{\text{pol}} \int_{I(\omega,\theta_A;T_f,q_f)} \hbar\omega \left[p^2(\omega[1-q_f\cos\theta_A],T_f) - p^2(\omega[1+q_f\cos\theta_A],T_f)\right] (c_A\cos\theta_A)d\Omega_A, \tag{7.1}$$

where $I(\omega,\theta_A;T_f,q_f)$ is the compatibility domain which is determined from

$$I: \begin{cases} F_-(T_f,q_f;\omega,\theta_A) & \leq f(T_f,q_f;\omega,\theta_A) \leq F_+(T_f,q_f;\omega,\theta_A), \\ F_-(T_f,-q_f;\omega,\theta_A) & \leq f(T_f,-q_f;\omega,\theta_A) \leq F_+(T_f,-q_f;\omega,\theta_A), \end{cases} \tag{7.2}$$

where

$$F_\pm(T,q;\omega,\theta) = |p(\omega[1+q\cos\theta],T) \pm R_A p(\omega[1-q\cos\theta],T)|, \tag{7.3}$$

and

$$f_\pm(T,q;\omega,\theta) = \sqrt{1-R_A^2}p(\omega[1+q\cos\theta],T). \tag{7.4}$$

In a steady state condition the controllable parameters are the temperatures of the half-spaces, (T_A,T_B), and the heat flux between them, Q. If we impose two of these three parameters we can determine the third one. We would like to devise an approach to obtain Q when (T_A,T_B) are given, and to obtain T_A when (Q,T_B) are given. For this purpose, we make some assumptions about the parameters and the evolution of the system from an equilibrium state to a steady state system.

7.2.1 Temperatures

Let $T_B \leq T_f \leq T_A$, and introduce T_f by

$$T_f = \frac{T_A+T_B}{2}. \tag{7.5}$$

Assume that at the beginning, i.e. in equilibrium, the temperatures of A and B are some base temperature $T_A^0 = T_B^0 = T_0$, where T_0 is not known at the moment. Accordingly, $T_f^0 = T_0$

and $q_f = 0$. After imposing the steady state condition, the initial values adjust themselves to satisfy this steady state conditions:

$$T_A^0 \to T_A, \qquad T_B^0 \to T_B. \tag{7.6}$$

We assume that the average temperature of the media $\dfrac{T_A + T_B}{2}$ remains the same. Hence, we have

$$T_0 = T_f^0 = \frac{T_A + T_B}{2} \Rightarrow T_f = T_f^0. \tag{7.7}$$

These assumptions lead to an important conclusion that the temperature of field is constant and equal to the base temperature of the system.

7.2.2 The Extra Energy

In a steady state condition, the imposed heat flux Q causes the field to adjust its parameter, q_f, according to (7.1) so that it transfers a net heat flux equal to Q in the given direction. Due to compatibility conditions (7.2) the field at its current state, $(T_f = T_0, q_f \neq 0)$, does not excite waves for all pairs of (ω, θ). Instead, this field is composed of excited waves with $(T_f = T_0, q_f \neq 0)$, which carry energy, and with incompatible waves with $(T_f = T_0, q_f = 0)$ which do not contribute to the energy transfer. The energy density of incompatible waves is

$$\overline{\mathcal{E}_A^0}(T_f, q_f) = \sum_{\text{pol}} \int_{\overline{I}(\theta_A, \omega_A, T_f, q_f)} \hbar\omega \left[2p^2(\omega, T_f)\right] d\Omega_A, \qquad \left[\frac{\text{J}}{\text{m}^3}\right], \tag{7.8}$$

while the energy density that is supposed to be stored in them is

$$\begin{aligned}\overline{\mathcal{E}_A}(T_f, q_f) = \sum_{\text{pol}} \int_{\overline{I}(\theta_A, \omega_A, T_f, q_f)} &\hbar\omega \left[p^2(\omega[1 - q_f \cos\theta_A], T_f) + p^2(\omega[1 + q_f \cos\theta_A], T_f)\right] \\ &\times d\Omega_A, \qquad \left[\frac{\text{J}}{\text{m}^3}\right].\end{aligned} \tag{7.9}$$

where

$$\Omega_0 = I(\theta_A, \omega_A, T_f, q_f) \cup \overline{I}(\theta_A, \omega_A, T_f, q_f), \tag{7.10}$$

and Ω_0 is the set of all possible pairs for (ω, θ). The difference between the terms in (7.8) and (7.8) is the extra energy density that the incompatible waves cannot store.

$$\overline{\Delta\mathcal{E}_A}(T_f, q_f) = \overline{\mathcal{E}_A}(T_f, q_f) - \overline{\mathcal{E}_A^0}(T_f, q_f). \tag{7.11}$$

This is also the case for B

$$\overline{\Delta\mathcal{E}_B}(T_f, q_f) = \overline{\mathcal{E}_B}(T_f, q_f) - \overline{\mathcal{E}_A^0}(T_f, q_f), \tag{7.12}$$

where

$$\overline{\mathcal{E}_B^0}(T_f,q_f)=\sum_{\text{pol}}\int_{\overline{I}}\hbar\omega\left[p^2(\omega,T_f)+p^2(\omega,T_f)\right]\frac{\omega^2}{4\pi^2c_B^3}\sin\theta_B d\theta_B d\omega,\qquad\left[\frac{\text{J}}{\text{m}^3}\right],\tag{7.13}$$

and

$$\begin{aligned}\overline{\mathcal{E}_B}(T_f,q_f)=\sum_{\text{pol}}\int_{\overline{I}}&\hbar\omega\left[p^2(\omega[1-q_f\cos\theta_A],T_f)+p^2(\omega[1+q_f\cos\theta_A],T_f)\right]\\&\times\frac{\omega^2}{4\pi^2c_B^3}\sin\theta_B d\theta_B d\omega,\qquad\left[\frac{\text{J}}{\text{m}^3}\right].\end{aligned}\tag{7.14}$$

7.3 The Non-propagating Waves

The extra energy may be stored as the energy of waves which are not transmitted to the other half-space, and therefore do not transfer energy. We call them non-propagating waves. For this to be the case, the corresponding reflection coefficient of waves has to be unity. Waves propagating parallel to the surface of half-spaces and waves with incident angles beyond the critical angle in both domains have $R = 1$. Since these waves do not transfer energy they are in equilibrium with their domains and must have the same temperature as the corresponding domain A or B. This means that increasing the temperature of these waves due to extra energy would increase the temperature of the domains too. Thus, it is enough to compute the temperature of non-propagating waves in A and B, and attribute to bodies A and B respectively.

Next, it is necessary to evaluate the equivalent amount of energy density of incompatible waves from B into A. But comparing the energy densities is equivalent to comparison of two equal volumes of the materials A and B which have different numbers of photons or phonons in them. In order to have a one-to-one correspondence we compare the energy in a volume of B which has the same number of photons or phonons as a unit volume in A. Using this we can define the equivalent energy density of B.

$$\overline{\Delta\mathcal{E}_{B,eq}}(T_f,q_f)=\frac{N_A}{N_B}\overline{\Delta\mathcal{E}_B}(T_f,q_f),\tag{7.15}$$

where N_A and N_B are density number of photons in each domain.

$$\begin{aligned}N_\eta=\sum_{\text{pol}}\int_{I(T_f,q_f)}&\left[p^2(\omega[1-q_f\cos\theta_A],T_f)+p^2(\omega[1+q_f\cos\theta_A],T_f)\right]\\&\times\frac{\omega^2}{4\pi^2c_\eta^3}\sin\theta_\eta d\theta_\eta d\omega,\qquad\left[\frac{1}{\text{m}^3}\right],\qquad\eta=A,B.\end{aligned}\tag{7.16}$$

Hence, we can use the expression $\overline{\Delta\mathcal{E}_{B,eq}}(T_f,q_f)$ in (7.15) as the equivalent amount of energy density added from the incompatible waves in B to non-propagating waves of either A or B.

As it is mentioned the non-propagating waves are waves parallel to the surface of the half-spaces or the waves beyond the critical angle. First we need to quantify the energy stored in these waves both in equilibrium state and steady state.

The energy stored in the parallel waves in domain A and B is computed on a 2D surface parallel to the surface of the half-spaces,

$$\mathcal{E}^{2D}_{\eta,\|}(T_\eta) = \sum_{\text{pol}} \int_{\bar{I}(T_f,q_f)} \hbar\omega \left[2p^2(\omega, T_\eta)\right] \frac{\omega}{4\pi^2 c_\eta^2} d\omega, \quad \left[\frac{\mathrm{J}}{\mathrm{m}^2}\right], \qquad \eta = A, B. \tag{7.17}$$

Note that the $\|$ sign is not related to the parallel polarization of the field here. This is the energy density per unit area. In order to compute the energy density $[\frac{J}{m^3}]$ from surface energy $[\frac{J}{m^2}]$, we divide the surface energy by a characteristic length parameter,

$$\mathcal{E}_{\eta,\|} = \frac{\mathcal{E}^{2D}_{\eta,\|}}{\gamma_\eta}, \qquad \eta = A, B. \tag{7.18}$$

The value of γ_η can be defined using an equivalent thickness. This equivalent thickness is determined that as:

$$\gamma_\eta N^{3D}_\eta = N^{2D}_\eta, \qquad \eta = A, B. \tag{7.19}$$

So

$$\gamma_\eta(T_\eta) = \frac{\sum_{\text{pol}} \int_{I(T_f,q_f)} \left[2p^2(\omega, T_\eta)\right] \frac{\omega}{4\pi^2 c_\eta^2} d\omega}{\sum_{\text{pol}} \int_{I(T_f,q_f)} \left[2p^2(\omega, T_\eta)\right] \frac{\omega^2}{4\pi^2 c_\eta^3} \sin\theta_\eta d\theta_\eta d\omega}, \qquad \eta = A, B. \tag{7.20}$$

Eventually

$$\mathcal{E}_{\eta,\|}(T_\eta) = \mathcal{E}^{2D}_{\eta,\|}(T_\eta)/\gamma_\eta(T_\eta), \qquad \eta = A, B. \tag{7.21}$$

This expression computes the energy density of parallel waves at any given temperature.

In the case where the critical angle exists in A or B, the energy density stored in the waves beyond critical angle, if any, is:

$$\mathcal{E}^{\theta_c}_\eta(T_\eta) = \sum_{\text{pol}} \int_0^\infty \int_{\theta^c_\eta}^{\pi/2} \hbar\omega \left[2p^2(\omega, T_\eta)\right] \frac{\omega^2}{4\pi^2 c_\eta^3} \sin\theta_\eta d\theta_\eta \omega, \quad \left[\frac{\mathrm{J}}{\mathrm{m}^3}\right], \qquad \eta = A, B. \tag{7.22}$$

Having (7.21) and (7.22) we compute the energy density of non-propagating waves at equilibrium:

$$\mathcal{E}^{\text{non}}_\eta(T_0) = \mathcal{E}^{\theta_c}_\eta(T_0) + \mathcal{E}_{\eta,\|}(T_0), \qquad \eta = A, B, \tag{7.23}$$

where the equivalent energy of B in A is

$$\mathcal{E}^{\text{non}}_{B,eq}(T_0) = \frac{N_A}{N_B} \left[\mathcal{E}^{\theta_c}_B(T_0) + \mathcal{E}_{B,\|}(T_0)\right]. \tag{7.24}$$

When the steady condition is imposed the energy stored in non-propagating waves increases by the amount from (7.9) and (7.14). Thus,

$$\mathcal{E}_A^{\text{non}}(T_A) + \mathcal{E}_{B,eq}^{\text{non}}(T_B) = \mathcal{E}_A^{\text{non}}(T_0) + \mathcal{E}_{B,eq}^{\text{non}}(T_0) + \overline{\Delta\mathcal{E}_A}(T_f, q_f) + \overline{\Delta\mathcal{E}_{B,eq}}(T_f, q_f). \tag{7.25}$$

Eventually by putting (7.1), (7.7) and (7.25) together we have

$$\begin{aligned} Q &= Q(T_f, q_f), \\ T_0 &= \frac{T_A + T_B}{2}, \\ T_f &= \frac{T_A + T_B}{2}, \\ \mathcal{E}_A^{\text{non}}(T_A) + \mathcal{E}_{B,eq}^{\text{non}}(T_B) &= \mathcal{E}_A^{\text{non}}(T_0) + \mathcal{E}_{B,eq}^{\text{non}}(T_0) + \overline{\Delta\mathcal{E}_A}(T_f, q_f) + \overline{\Delta\mathcal{E}_{B,eq}}(T_f, q_f), \end{aligned} \tag{7.26}$$

where $Q, T_A, T_B, T_0, T_f, q_f$ are the parameters. We have four equations and six unknowns at the moment. If we know two of the three measurable parameters, (Q, T_A, T_B), then we can determine the other unknown measurable parameter as well as T_f and q_f. Two typical scenarios that we encounter is the following: 1. the temperatures of both domains are known, (T_A, T_B). We are interested to determine the heat flux Q and HTC for a given distance between them, 2. the temperature of body B, T_B, and the heat flux, Q are known in steady state. We are interested to obtain the temperatures of T_A and the HTC for a given distance between them.

7.4 Results for Radiation

7.4.1 Identical Half-spaces and Known Temperatures

When T_A and T_B are known, then T_f and T_0 automatically are known from (7.26). We solve the forth equation (7.26) in for q_f using an iterative algorithm and then determine Q from the first equation (7.26). The results for identical material properties of the half-spaces are presented in Fig. 7.2. For comparison purposes, we assume that the speed of electromagnetic waves inside the half-spaces is $c_A = c_B = 0.45c_0$, as in [34]. In this simulation the temperature of the cooler domain is $T_B = 298$K. Simulations are repeated for three temperature differences; $\Delta T = 0.01\text{K}, 1\text{K}, 400\text{K}$.

Fig. 7.2a shows the heat flux computed as a function of spacing between the half-spaces. These curves correctly show the enhancement of heat flux between the half-spaces due to the decrease in the spacing. The resultant heat flux for far field radiation is following the general trend of the black body radiation calculations. It is obvious that the obtained heat flux for far field radiation is smaller than black body radiation. This is the case since the given material is a gray body rather than a black body, which does not take into account the emissivity of the material. Also, as expected, a larger temperature difference gives a larger heat flux.

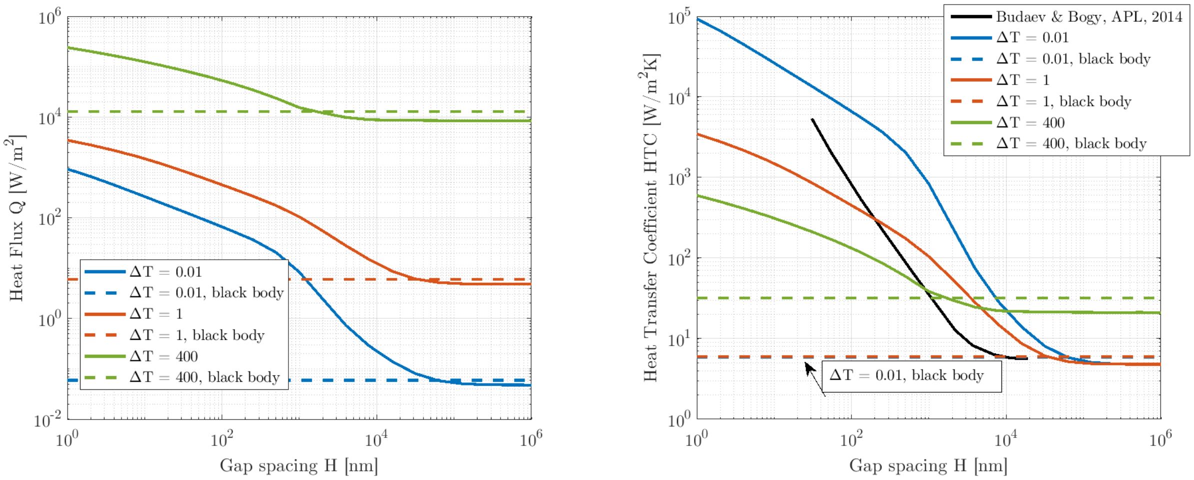

(a) The radiative heat flux Q vs spacing

(b) The radiative HTC vs spacing

Figure 7.2: The radiative heat flux between two half-spaces A and B with known T_A and T_B using the unified radiation field approach vs spacing in solid lines, identical material are used for A and B with speed $c_A = c_B = 0.45c_0$, the dotted lines show the black body radiation (BBR) results

The corresponding HTC for the simulations is plotted in Fig. 7.2b. For large spacings, the obtained HTC is larger for a larger ΔT, as it is the case for black body radiation while in near field radiation a larger ΔT leads to a smaller coefficient. In addition, the slope of the curves tends to decrease as ΔT increases.

We would like to compare the results for HTC with the previous calculations for the same structure in [34]. The black curve in Fig. 7.2b is the HTC computed for an infinitesimal temperature difference between materials. We were hoping to obtain a similar HTC curve as the ΔT decreases. The blue curve corresponding to a $\Delta T = 0.01$ resembles a similar slope as the reference curve; however; the enhancement starts occurring in $100\mu m$ as opposed to $10\mu m$ for the reference curve.

There are a few differences in the calculations that can justify this difference. First, the reference curve is obtained by combining the effect of the two polarizations of the field into one averaged reflection coefficient while the reflection coefficients for the waves with parallel and perpendicular polarizations are vastly different. In our calculations we consider the reflection coefficient of each polarization independently; and consequently, the contribution of each polarization to the heat flux separately. Moreover, the referenced paper solved the linearized equations of the problem while we solve the complete nonlinear equations. We expect these changes would make the results more accurate.

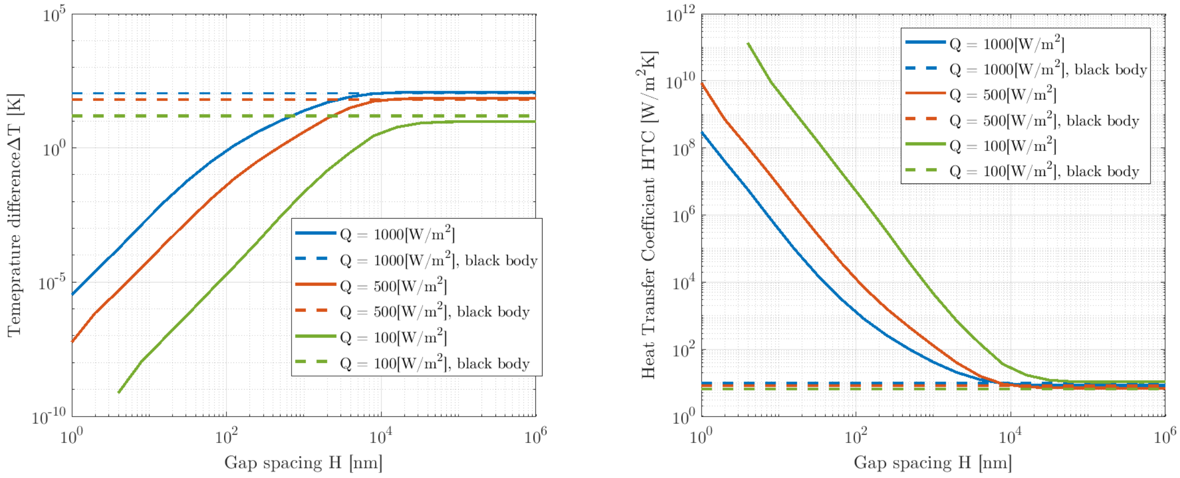

(a) The temperature difference vs spacing

(b) The radiative HTC vs spacing

Figure 7.3: The radiative heat flux between two half-spaces A and B with known Q and T_B using the unified radiation field approach vs spacing in solid lines, identical material are used for A and B with speed $c_A = c_B = 0.45c_0$, the dotted lines show the black body radiation (BBR) results

7.4.2 Identical Half-spaces with Known Heat Flux and One Known Temperature

In this case, T_0 and T_f are not determined explicitly. But we use an iterative algorithm to gradually converge to the solution for the following parameters: T_A, T_f, T_0, q_f.

Algorithm 1 $\Delta T(T_B, Q)$

```
Input: $T_B$, $Q$, Material properties
Set $T_f = T_B$, $T_0 = T_B$.
while True do
    Solve (7.1) to obtain $q_f$ using bisection root finding method in the interval $[0, 1]$
    Solve (7.25) to obtain $T_A$ using a root finding algorithm in appendix C.
    $T_f^0 = T_f$.
    $T_f = \frac{T_A + T_B}{2}$.
    $T_0 = T_f$.
    if $|T_f - T_f^0| \leq \varepsilon$ then
        break
    end if
end while
Output: $\Delta T = T_A - T_B$
```

Using this algorithm we obtained and analyzed the results for various materials for the half-spaces. The speed of electromagnetic waves inside the half-spaces is $c_A = c_B = 0.45c$. The temperature of the cooler half-space is $T_0 = 298K$. Then, various values of the heat flux, $Q = 100, 500, 1000$ $[\frac{\mathrm{W}}{\mathrm{m}^2}]$, are imposed and the corresponding temperature differences are computed as functions of the spacing between the half-spaces.

The computed ΔT in Fig. 7.3a has a decreasing trend from large spacing to smaller spacing because of the decrease of the reflection coefficient between the half-spaces. As the spacing becomes smaller the less amount of the waves gets reflected and the energy transfer gets easier. In another words, the resistance between the layers decreases and the half-spaces would have their temperature closer to each other. Also the results in both Fig. 7.3a and Fig. 7.3b in far field radiation agree with calculations from black body radiation.

Since the half-spaces are composed of identical material, for a spacing of zero between the media there is no thermal resistance; hence, the temperature of both media is the same and any given heat flux can pass through the media as long as the given heat flux is below the multiplication of the average energy density of the medium and the speed of waves in the medium. On the other hand, for a very large spacing between the media the interaction between photons of these media is very weak and the corresponding results should converge to a constant value close the value of the black body radiation.

7.4.3 Radiation from Absorbing Materials

In this section, we consider multilayered structures from absorbing materials and obtain heat transfer coefficient by the formulation presented above. For the absorbing materials the speed is a function of the depth in materials, however, in the following calculations we use a speed averaged over the depth so it is only a function of the frequency. We define the average wave speed using the weight function $w(x) = e^{-2\omega n'' x / c_0 \cos\theta}$ for the wave speed in chapter 6 since the probability of wave in depth x reaching the surface drops exponentially,

$$c(\omega, T) = \lim_{H \to \infty} \frac{\int_0^H c(\omega, \theta, x, T, n', n'') w(x) dx}{\int_0^H w(x) dx} = \frac{1}{2} \frac{c_0}{n'(\omega)} + \frac{1}{2} c_*(\omega, T). \tag{7.27}$$

In Fig. 7.4 the HTC for two half-spaces of $\mathrm{SiO_2}$ is plotted for 3 different calculation methods. The blue curve shows the results from [34] where the problem is linearized for small temperature differences and small heat fluxes between materials while assuming that the speed of EM wave is equal to $0.45c_0$. The blue curve has a slope proportional to $1/H^2$ or less when the radiation enhancements starts. The red curve is determined using the unified field introduced above for the wave speed $0.45c_0$ and a temperature difference $\Delta T = 0.1$ K. In these calculations the HTC enhancement starts in larger spacings ($\approx 40\mu$m). Also the curve has two slops; one proportional to $1/H^2$ and one for spacings less than 10nm with a smaller slop. For the yellow curve, we used the frequency dependent complex refractive index to determine the wave speed. The yellow curve follows the same trend as the red curve. The yellow curve is expected to give the most accurate result.

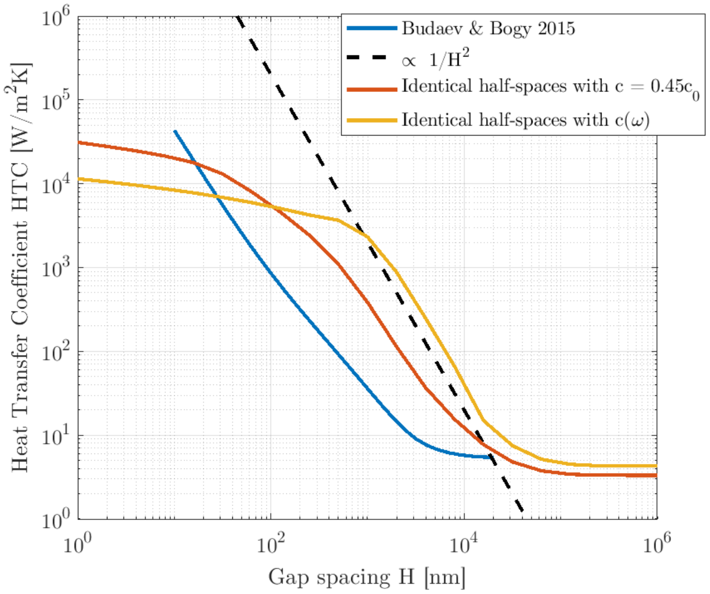

Figure 7.4: The radiative HTC vs gap spacing for three cases are compared to the $1/H^2$ slope, the blue curve from linearized radiation model, the red curve for constant wave speed in material, the yellow curve for absorbing material structures of silica with the wave speed model from chapter 6, $\Delta T = 0.1$ and $T_B = 298$ K

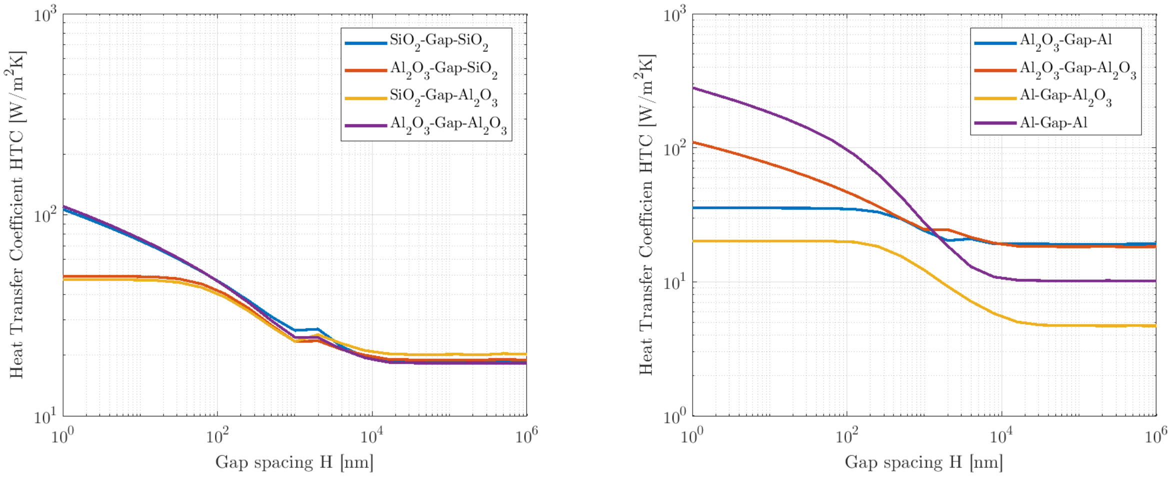

(a) The half-spaces are alumina and silica (b) The half-spaces are alumina and aluminum

Figure 7.5: The radiative HTC using unified field assumption vs gap spacing for various half-spaces and for large temperature differences in order to show the asymmetry of the HTC when the temperatures are swapped, $\Delta T = 400$ K and $T_B = 298$ K

In Fig. 7.5, we have HTC for half-spaces of different materials and $\Delta T = 400$. As we see, from the results for silica/alumina and aluminum/alumina, the HTC can be very different than when the hot and cold half-spaces are swapped which indicates the asymmetry in the HTC in the direction of net heat flux. In the case of silica/alumina, the HTC's in the opposite directions are not very different, indicating that thermal properties of the considered materials are similar. On the other hand, the asymmetry of HTC is obvious for aluminum/alumina half-spaces.

7.5 Solution for Phonon Conduction by a Unified Field

In this section, we apply the unified field to the calculations of HTC of phonon conduction in multilayered structures and compare obtained results with the calculations from section 5.4. We assume that the cooler half-space (B) always is alumina, while the substrate medium (A) is made of alumina, aluminum, glass or silicon. The results are shown for two temperature differences $\Delta T = 0.1$ K, $\Delta T = 400$ K and the difference between the results is discussed. We show that phonon conduction heat transfer is dominant for gap spacings of a few nanometers or less while the contribution of this heat transfer mode abruptly drops to very small values as the gap spacing become larger than 4nm as predicted [19, 20].

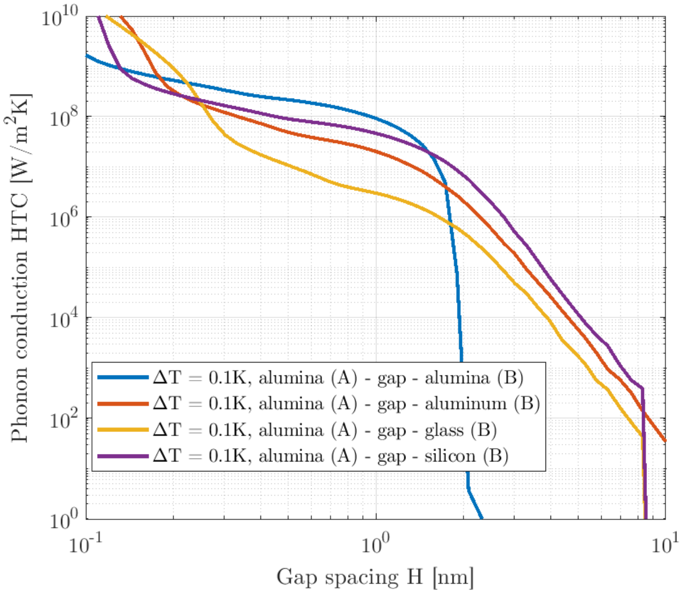

Figure 7.6: The phonon conduction HTC using the unified field model between an alumina half-space (A) and various half-spaces (B) vs gap spacing, hot half-space A is alumina, $\Delta T = 0.1$ K and $T_B = 298$ K

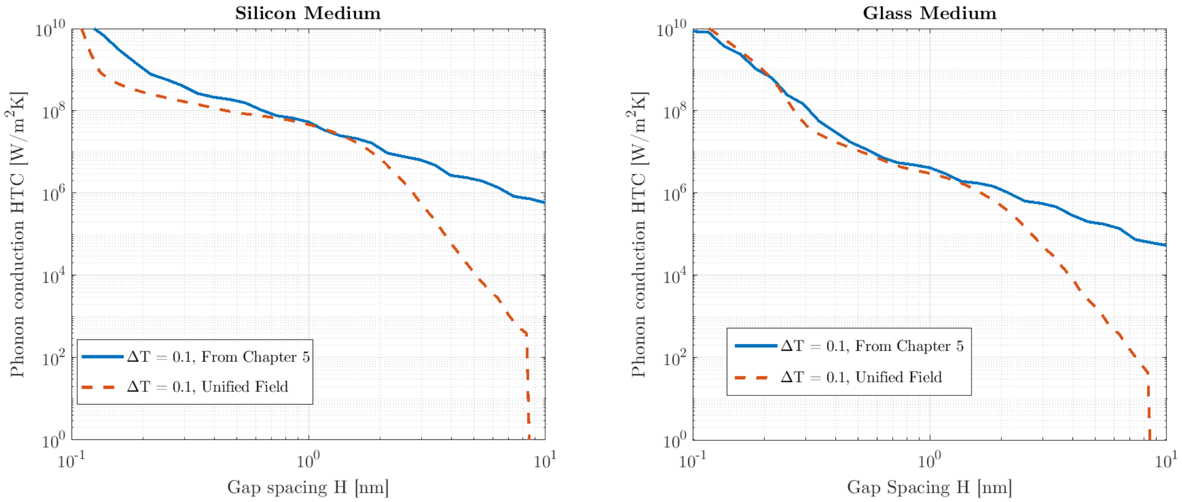

(a) The structure: silicon-gap-alumina (b) The structure: glass-gap-alumina

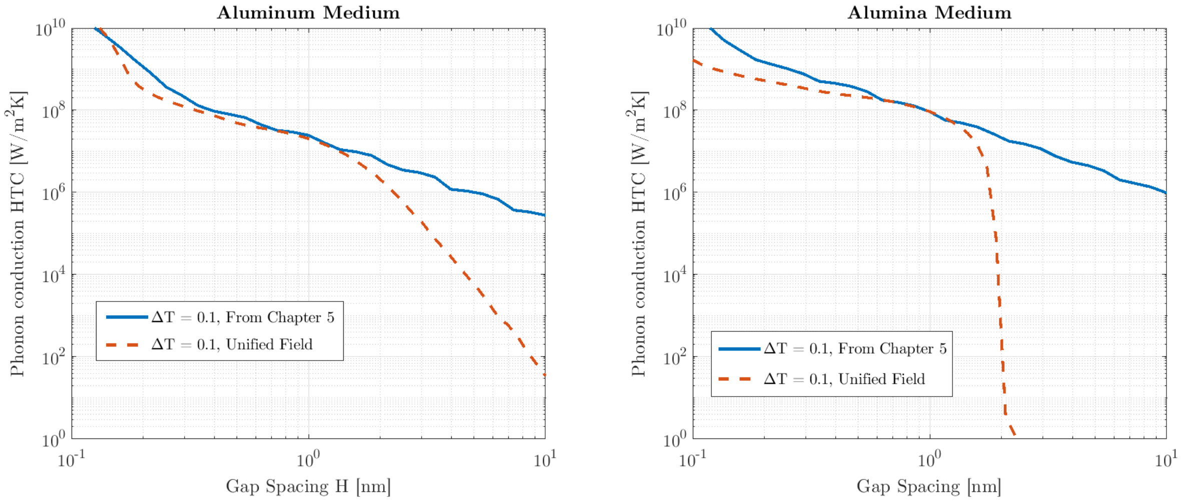

(c) The structure: aluminum-gap-alumina (d) The structure: alumina-gap-alumina

Figure 7.7: The phonon conduction HTC for phonons using the unified field between an alumina half-space (A) and various half-spaces are compared with the results from chapter 5, $\Delta T = 0.1$ K and $T_B = 298$ K

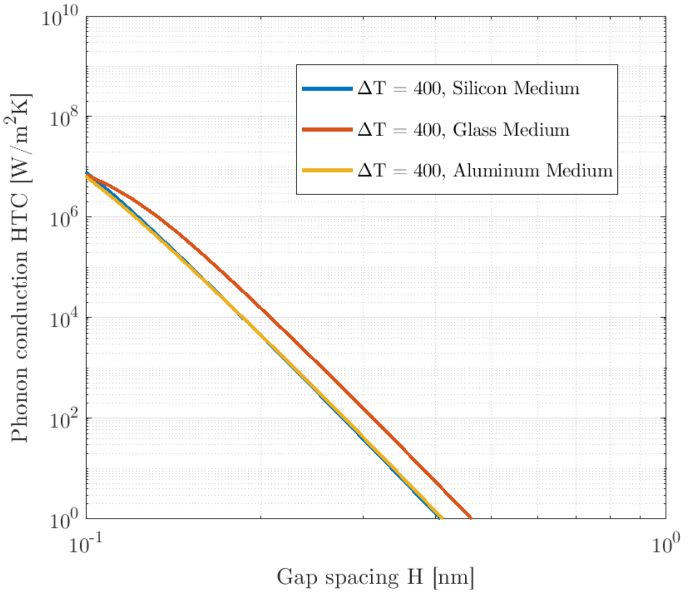

Figure 7.8: The phonon conduction HTC using the unified field model between an alumina half-space (A) and various half-spaces (B) vs gap spacing, the half-space A is alumina, $\Delta T = 400$ K and $T_B = 298$ K

In Fig. 7.6 the HTC vs H is shown for four structures with the temperature difference $\Delta T = 0.1$ K. As we see, in all cases the HTC remains relatively high for the spacings less than 4nm, but it drops very fast when the spacing increases further. This is expected because vdW forces are not effective beyond a few nanometers between two materials. It should be noted that, depending on the material properties of the half-spaces the HTC drops down in different gap spacings and with different slops.

In Fig. 7.7, we compare these results with the results obtained in section 5.4. The curves in all four structures are almost identical for gap spacings below 1nm, but for larger spacings deviate from each other. The results obtained from the unified field assumption drop faster for larger spacing and represent a more accurate representation of HTC of phonon conduction.

In Fig. 7.8, the HTC is shown for three structures where $\Delta T = 400$ K. The HTC compared by this method is significantly smaller than what we have in section 5.4. This is shown in Fig. 7.9. As we see, the slop of HTC for these results is larger and the HTC starts becoming insignificant even for spacings below 1nm. This indicates that the use of a unified field for defining the distribution of thermally excited waves in both half-spaces is not a reasonable assumption when the temperature difference between them is considerably large.

The results for phonon conduction at small temperature differences predict the abrupt drop in the phonon conduction HTC when the spacing is beyond a few nanometer which is

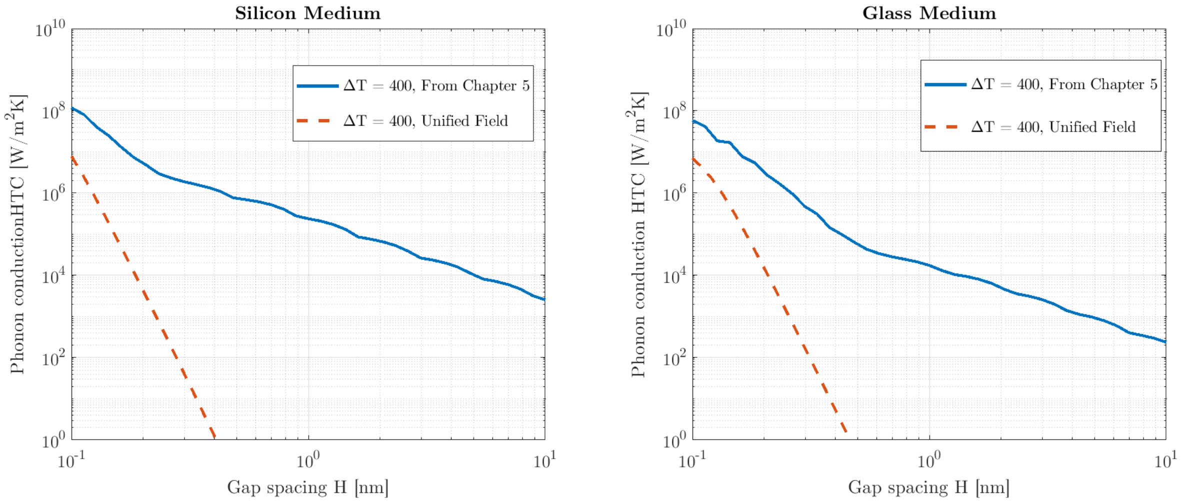

(a) The structure: silicon-gap-alumina

(b) The structure: glass-gap-alumina

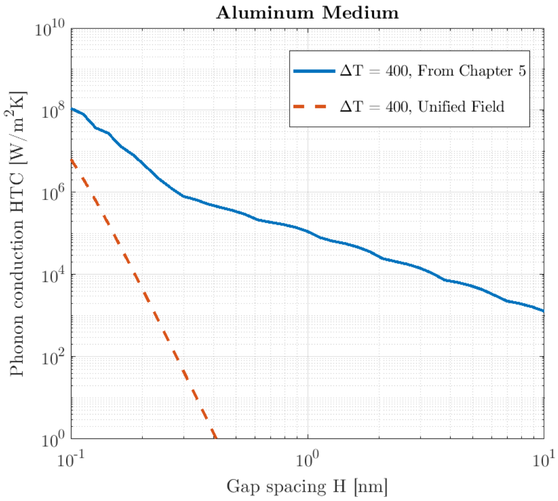

(c) The structure: aluminum-gap-alumina

Figure 7.9: The phonon conduction HTC for phonons using the unified field between an alumina half-space (A) and various half-spaces are compared with the results from chapter 5, $\Delta T = 400$ K and $T_B = 298$ K

more accurate than the result in section 5.4. The application of this method is limited to the case with small temperature difference between materials since when the temperature difference between materials is large the unified field cannot accurately represent the combination of the two separated field in each domain.

In this chapter we developed a method to solve the heat transfer problem in multilayered structures using a unified emission field in the entire structure once for radiation and once for phonon conduction. The results for radiation are along with our expectation from the theory and they also show the asymmetry effect due to the change of the direction of the heat flux. The model predicts the phonon conduction for small temperature differences more accurately than presented results in chapter 5.

Chapter 8

Summary and Conclusion

We studied the heat transfer mechanisms of radiation and phonon conduction in nanoscale and performed numerical calculations on the presented models. We also studied the classical models that are used for these heat transfer modes. We determined that the classical models do not apply to the nanoscale problems of interest in HAMR due to limiting assumptions contributing to their derivation, because models are based on Planck's law for equilibrium conditions that have no net heat transfer and do not consider the wave nature of the heat carriers. We studied the extension of Planck's law for nanoscale heat transfer in steady state conditions. This model has previously been numerically solved by linearization for small heat fluxes, as we reviewed.

We developed a model applicable to nanoscale structures with a large heat flux (Q). The presented model applies the special relativity theory concepts in transforming Planck's distribution for equilibrium into steady-state systems with a large heat flux. We then presented numerical calculations for this model and presented the HTC for various material structures with large heat fluxes and temperature differences in the system. We showed how the HTC rate changes as a function of the spacing between two layered structures with fixed temperatures, and showed that the results agree with the previous results for the linearized models when the Q and ΔT are small. Using these calculations, we showed that the radiative HTC between two layered structures enhances by two orders of magnitude as the spacing is below a few microns, which is the dominant wavelength of radiation at room temperature. Also, the phonon conduction HTC enhances for up to seven orders of magnitude for spacings around one nanometer.

Next, we presented the numerical solutions for a more advanced model, which considers the wave nature of the heat carriers by taking into account the interference of the heat carriers from the sources with different temperatures. This leads to compatibility conditions that correlate the generated heat carriers from both sides. The compatibility conditions determine which waves can pass through the structures and transfer heat. This provided a range of solutions for the heat flux. To obtain the solution we used the maximum entropy principle to determine the heat flux uniquely. The obtained numerical results indicate that phonon conduction is also significant for gap spacings larger than one nanometer, as predicted in the theoretical works. We used these results to predict the HTC in the thermo-mechanical simulations of the HDI of HAMR HDD.

Next we used the depth-dependent description of thermal radiation's speed to determine the radiation from the surface of absorbing materials. We showed that the absorbing materials are described as grey materials with an emissivity coefficient of ϵ. The radiative heat fluxes from absorbing materials, under the assumption for the speed model in chapter 6, quantitatively match those described from the grey body assumption.

We also introduced a unified emission field concept, which describes the emission of thermally excited waves at any point in the structure. Here certain conditions are needed to determine its parameters. Then we numerically solved the heat transfer problem in layered structures using the unified field for both radiation and phonon conduction. We used the unified field and the depth-dependent description of the wave speed to obtain the radiative heat flux in layered structures for real materials. The obtained results for phonon conduction show that this mode of heat transfer is dominant for gap spacings of a few nanometers or less, and the contribution of this heat transfer mode abruptly drops to negligible values when the gap spacing is larger than 4nm as has been predicted in some theoretical works.

As explained in chapter 7, the unified field model has a lack of accuracy when the half-spaces have very different temperatures. This model could be improved to apply it to systems with a large temperature difference. This can be done by directly modifying the unified field distribution to consider ΔT as another required parameter to determine the field entirely.

Bibliography

[1] T. Luo and G. Chen. "Nanoscale heat transfer–from computation to experiment". In: *Physical Chemistry Chemical Physics* 15.10 (2013), pp. 3389–3412.

[2] G. Chen. *Nanoscale energy transport and conversion: a parallel treatment of electrons, molecules, phonons, and photons.* Oxford University Press, 2005.

[3] B. Song et al. "Near-field radiative thermal transport: From theory to experiment". In: *AIP advances* 5.5 (2015), p. 053503.

[4] K. Kim et al. "Radiative heat transfer in the extreme near field". In: *Nature* 528.7582 (2015), pp. 387–391.

[5] C. M. Hargreaves. "Anomalous radiative transfer between closely-spaced bodies". In: *Physics Letters A* 30.9 (1969), pp. 491–492.

[6] C. L. Tien and G. Chen. "Challenges in microscale conductive and radiative heat transfer". In: *Journal of Heat Transfer* 116.4 (1994), pp. 799–807.

[7] G. A. Domoto, R. F. Boehm, and C. L. Tien. "Experimental investigation of radiative transfer between metallic surfaces at cryogenic temperatures". In: *Journal of Heat Transfer* 92.3 (1970), pp. 412–416.

[8] R. F. Boehm and C. L. Tien. "Small spacing analysis of radiative transfer between parallel metallic surfaces". In: *Journal of Heat Transfer* 92.3 (1970), pp. 405–411.

[9] E. G. Cravalho, C. L. Tien, and R. P. Caren. "Effect of small spacings on radiative transfer between two dielectrics". In: *Journal of Heat Transfer* 89.4 (1967), pp. 351–358.

[10] A. Kittel et al. "Near-field heat transfer in a scanning thermal microscope". In: *Physical review letters* 95.22 (2005), p. 224301.

[11] B. Song et al. "Enhancement of near-field radiative heat transfer using polar dielectric thin films". In: *Nature nanotechnology* 10.3 (2015), pp. 253–258.

[12] K. Kloppstech et al. "Giant heat transfer in the crossover regime between conduction and radiation". In: *Nature Communications* 8 (2017).

[13] E. Rousseau et al. "Radiative heat transfer at the nanoscale". In: *Nature Photonics* 3.9 (2009), pp. 514–517.

[14] E. Rousseau, M. Laroche, and J. J. Greffet. "Radiative heat transfer at nanoscale: Closed-form expression for silicon at different doping levels". In: *Journal of Quantitative Spectroscopy and Radiative Transfer* 111.7 (2010), pp. 1005–1014.

[15] R. S. Ottens et al. "Near-field radiative heat transfer between macroscopic planar surfaces". In: *Physical review letters* 107.1 (2011), p. 014301.

[16] D. V. H. M. Polder and M. Van Hove. "Theory of radiative heat transfer between closely spaced bodies". In: *Physical Review B* 4.10 (1971), p. 3303.

[17] S. M. Rytov. *Theory of electric fluctuations and thermal radiation.* Tech. rep. AIR FORCE CAMBRIDGE RESEARCH LABS HANSCOM AFB MA, 1959.

[18] J. B. Pendry. "Radiative exchange of heat between nanostructures". In: *Journal of Physics: Condensed Matter* 11.35 (1999), p. 6621.

[19] B. V. Budaev and D. B. Bogy. "On the mechanisms of heat transport across vacuum gaps". In: *Zeitschrift für angewandte Mathematik und Physik* 62.6 (2011), pp. 1143–1158.

[20] B. V. Budaev and D. B. Bogy. "On the role of acoustic waves (phonons) in equilibrium heat exchange across a vacuum gap". In: *Applied Physics Letters* 99.5 (2011), p. 053109.

[21] B. V. Budaev and D. B. Bogy. "On thermal radiation across nanoscale gaps". In: *Zeitschrift für angewandte Mathematik und Physik* 66.4 (2015), pp. 2061–2068.

[22] Z. M. Zhang. *Nano/microscale heat transfer.* Springer, 2007.

[23] K. Joulain et al. "Surface electromagnetic waves thermally excited: Radiative heat transfer, coherence properties and Casimir forces revisited in the near field". In: *Surface Science Reports* 57.3-4 (2005), pp. 59–112.

[24] A. Volokitin and B. N. Persson. "Near-field radiative heat transfer and noncontact friction". In: *Reviews of Modern Physics* 79.4 (2007), p. 1291.

[25] S. Basu, Z. Zhang, and C. Fu. "Review of near-field thermal radiation and its application to energy conversion". In: *International Journal of Energy Research* 33.13 (2009), pp. 1203–1232.

[26] D. G. Cahill et al. "Nanoscale thermal transport. II. 2003–2012". In: *Applied physics reviews* 1.1 (2014), p. 011305.

[27] Y. Xuan. "An overview of micro/nanoscaled thermal radiation and its applications". In: *Photonics and Nanostructures-Fundamentals and Applications* 12.2 (2014), pp. 93–113.

[28] J.-P. Mulet et al. "Nanoscale radiative heat transfer between a small particle and a plane surface". In: *Applied Physics Letters* 78.19 (2001), pp. 2931–2933.

[29] M. F. Modest. *Radiative heat transfer.* Academic press, 2013.

[30] M. Planck. *The theory of heat radiation.* Courier Corporation, 2013.

[31] B. R. Holstein. “Quantum mechanics in momentum space: The Coulomb system”. In: *American Journal of Physics* 63.8 (1995), pp. 710–716.

[32] H. Kragh. “Max Planck: the reluctant revolutionary”. In: *Physics World* 13.12 (2000), p. 31.

[33] C. Kittel and H. Kroemer. *Thermal physics*. 1998.

[34] B. V. Budaev and D. B. Bogy. “Computation of radiative heat transport across a nanoscale vacuum gap”. In: *Applied Physics Letters* 104.6 (2014), p. 061109.

[35] W. A. Challener et al. “Heat-assisted magnetic recording by a near-field transducer with efficient optical energy transfer”. In: *Nature photonics* 3.4 (2009), pp. 220–224.

[36] M. H. Kryder et al. “Heat assisted magnetic recording”. In: *Proceedings of the IEEE* 96.11 (2008), pp. 1810–1835.

[37] B. C. Stipe et al. “Magnetic recording at 1.5 Pb m- 2 using an integrated plasmonic antenna”. In: *Nature photonics* 4.7 (2010), pp. 484–488.

[38] D. Litvinov and S. Khizroev. “Perpendicular magnetic recording: playback”. In: *Journal of applied physics* 97.7 (2005), p. 6.

[39] M. H. Kryder. “Magnetic recording beyond the superparamagnetic limit”. In: *2000 IEEE International Magnetics Conference (INTERMAG)*. IEEE. 2000, pp. 575–575.

[40] L. Pan and D. B. Bogy. “Heat-assisted magnetic recording”. In: *Nature Photonics* 3.4 (2009), pp. 189–190.

[41] B. Marchon et al. “Head–disk interface materials issues in heat-assisted magnetic recording”. In: *IEEE transactions on magnetics* 50.3 (2014), pp. 137–143.

[42] R. P. Feynman. “Feynman lectures on physics. Volume 2: Mainly electromagnetism and matter”. In: *flp* (1964).

[43] J. D. Jackson. *Classical electrodynamics*. John Wiley & Sons, 2007.

[44] D. J. Griffiths. *Introduction to electrodynamics*. 2005.

[45] L. Rayleigh. “LIII. Remarks upon the law of complete radiation”. In: *The London, Edinburgh, and Dublin Philosophical Magazine and Journal of Science* 49.301 (1900), pp. 539–540. DOI: `10.1080/14786440009463878`.

[46] G. B. Rybicki and A. P. Lightman. *Radiative processes in astrophysics*. John Wiley & Sons, 2008.

[47] *SI-Brochure-9.pdf*. `https://www.bipm.org/utils/common/pdf/si-brochure/SI-Brochure-9.pdf`. (Accessed on 04/19/2020).

[48] L. D. Landau, E. M. Lifshitz, and L. P. Pitaevskii. *Statistical physics: theory of the condensed state*. Vol. 9. Butterworth-Heinemann, 1980.

[49] F. Reif. “Berkeley physics course”. In: (1967).

[50] H. Weyl. “Das asymptotische Verteilungsgesetz der Eigenwerte linearer partieller Differentialgleichungen (mit einer Anwendung auf die Theorie der Hohlraumstrahlung)”. In: *Mathematische Annalen* 71.4 (1912), pp. 441–479.

[51] R. Courant and D. Hilbert. *Methods of Mathematical Physics: Partial Differential Equations*. John Wiley & Sons, 2008.

[52] D. P. Bertsekas. *Constrained optimization and Lagrange multiplier methods*. Academic press, 2014.

[53] B. V. Budaev and D. B. Bogy. “Systems with a constant heat flux with applications to radiative heat transport across nanoscale gaps and layers”. In: *Zeitschrift für angewandte Mathematik und Physik* 69.3 (2018), p. 71.

[54] B. V. Budaev and D. B. Bogy. “Extension of Planck’s law of thermal radiation to systems with a steady heat flux”. In: *Annalen der Physik* 523.10 (2011), pp. 791–804.

[55] M. Planck. “Zur dynamik bewegter systeme”. In: *Annalen der Physik* 331.6 (1908), pp. 1–34.

[56] H. Ott. “Lorentz-transformation der wärme und der temperatur”. In: *Zeitschrift für Physik* 175.1 (1963), pp. 70–104.

[57] I. Avramov. “Relativity and temperature”. In: *RUSSIAN JOURNAL OF PHYSICAL CHEMISTRY C/C OF ZHURNAL FIZICHESKOI KHIMII* 77.SUP (2003), S179–S182.

[58] D. Ferry and S. M. Goodnick. *Transport in nanostructures*. 6. Cambridge university press, 1999.

[59] L. Brekhovskikh. *Waves in layered media*. Vol. 16. Elsevier, 2012.

[60] P. Agarwal, M. Jleli, and B. Samet. “Banach Contraction Principle and Applications”. In: *Fixed Point Theory in Metric Spaces*. Springer, 2018, pp. 1–23.

[61] B. V. Budaev and D. B. Bogy. “Heat transport by phonon tunneling across layered structures used in heat assisted magnetic recording”. In: *Journal of Applied Physics* 117.10 (2015), p. 104512.

[62] J. N. Israelachvili. *Intermolecular and surface forces*. Academic press, 2011.

[63] Y. Ma et al. “Controlled heat flux measurement across a closing nanoscale gap and its comparison to theory”. In: *Applied Physics Letters* 108.21 (2016), p. 213105.

[64] Y. Ma et al. “Measurement and Simulation of Nanoscale Gap Heat Transfer Using a Read/Write Head With a Contact Sensor”. In: *IEEE Transactions on Magnetics* 53.2 (2017), pp. 1–5.

[65] S. Sakhalkar et al. “Numerical and experimental investigation of heat transfer across a nanoscale gap between a magnetic recording head and various media”. In: *Applied Physics Letters* 115.22 (2019), p. 223102.

[66] B. V. Budaev and D. B. Bogy. “On the Wave Speed of Thermal Radiation Inside and Near the Boundary of an Absorbing Material”. In: *Journal of Heat Transfer* 142.3 (2020).

[67] A. Lipson, S. G. Lipson, and H. Lipson. *Optical physics*. Cambridge University Press, 2010.

[68] O. Stavroudis. *The optics of rays, wavefronts, and caustics*. Vol. 38. Elsevier, 2012.

[69] *RefractiveIndex.INFO*. URL: `https://refractiveindex.info/`.

Appendices

Appendix A: Fixed Point Iteration Method

Algorithm 2 Fixed Point Iteration Method

```
Convergence Error: $(\epsilon_1, \epsilon_2, \epsilon_3)$
Initialize: $q_{A_0} \in (0,1)$, $q_{B_0} \in (0,1)$, $Q_0 \in (0,\infty)$
$q_A = G_1(q_{A_0}, Q_0)$
$q_B = G_2(q_{B_0}, Q_0)$
$Q = G_3(Q_0)$
while $|q_A - q_{A_0}| \geq \epsilon_1$ & $|q_B - q_{B_0}| \geq \epsilon_2$ & $|Q - Q_0| \geq \epsilon_3$ do
    $q_{A_0} = q_A$
    $q_{B_0} = q_B$
    $Q_0 = Q$
    $q_A = G_1(q_{A_0}, Q_0)$
    $q_B = G_2(q_{B_0}, Q_0)$
    $Q = G_3(Q_0)$
end while
Output: $Q$
```

Appendix B: Refractive Index of Some Materials

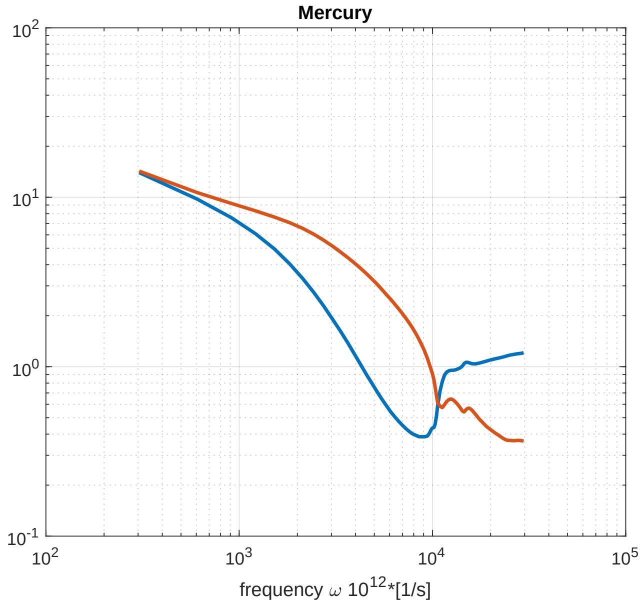

Figure 8.1: The complex refractive (n') index and extinction coefficient (n'') as a function of frequency for mercury (blue curve: n', red curve: n'') [69]

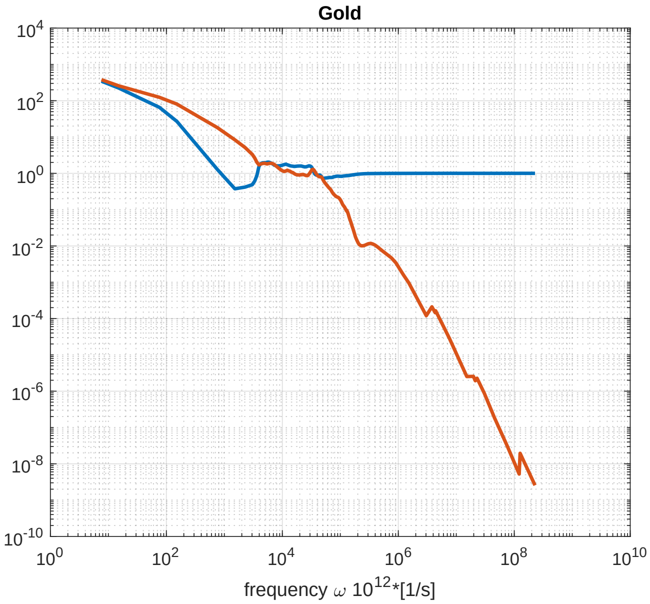

Figure 8.2: The complex refractive (n') index and extinction coefficient (n'') as a function of frequency for gold (blue curve: n', red curve: n'') [69]

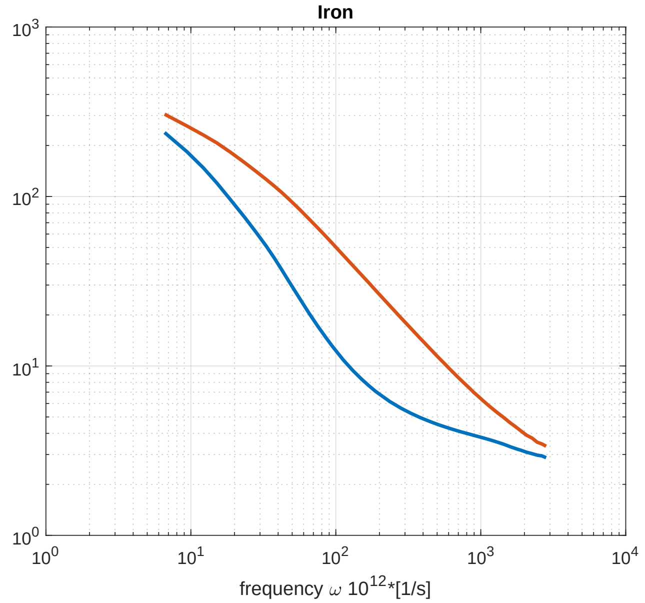

Figure 8.3: The complex refractive (n') index and extinction coefficient (n'') as a function of frequency for iron (blue curve: n', red curve: n'') [69]

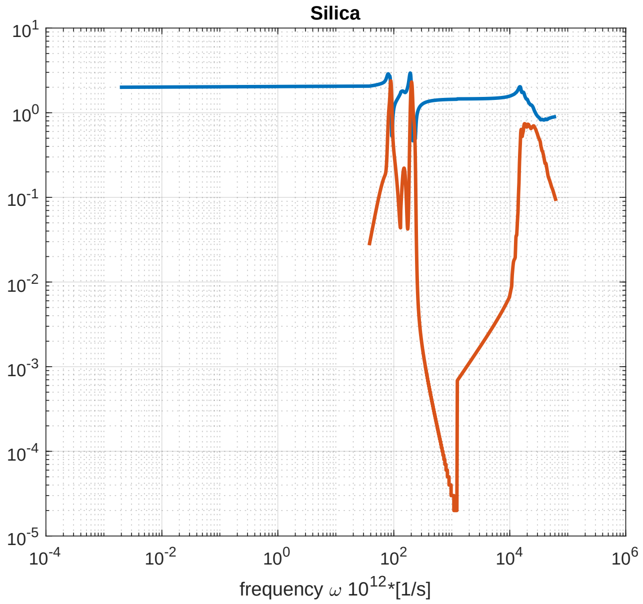

Figure 8.4: The complex refractive (n') index and extinction coefficient (n'') as a function of frequency for silica (blue curve: n', red curve: n'') [69]

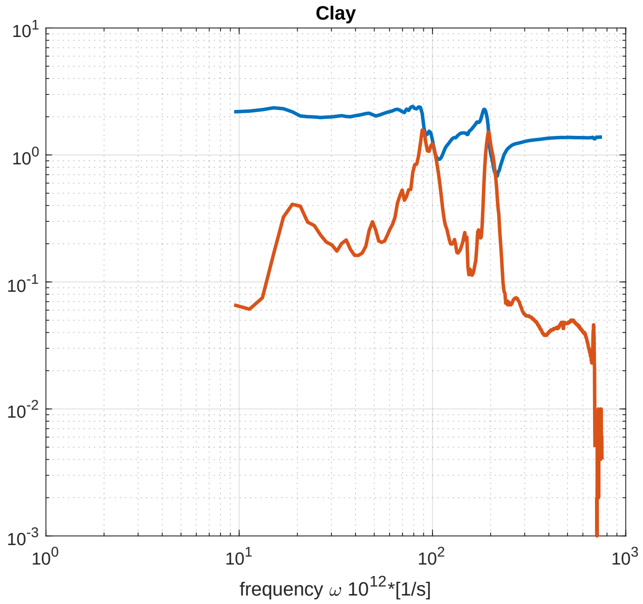

Figure 8.5: The complex refractive (n') index and extinction coefficient (n'') as a function of frequency for clay (blue curve: n', red curve: n'') [69]

Appendix C: Root Finding Algorithm

Algorithm 3 Root finding for $f(x)$ in $X = [a, b]$

```
Roots are stored in empty variable $x$
Set the accuracy of calculations to be $\varepsilon$
Define the list $H$ to store the possible intervals of solutions; $H = \{[a, b]\}$
Set $n \geq \frac{b-a}{\sqrt{\varepsilon}}$; the number of points on which to determine $f'(x)$ in each interval
% For midpoint derivative of $f'(x)$; accuracy $O(\delta^2) = O\left(\left(\frac{b-a}{n}\right)^2\right) \leq \varepsilon \Rightarrow n \geq \frac{b-a}{\sqrt{\varepsilon}}$
**root** = False; this determines if there is any possible root in an interval based on $(f, f')$
**while** the list $H$ is not empty **do**
  Choose the last interval in H as the current interval, $X_i = [a_i, b_i] = H\{\text{end}\}$
  Obtain the midpoint of the current interval; $x_m = \frac{a_i + b_i}{2}$
  Set the uniform mesh size $\delta = \frac{b_i - a_i}{n}$
  Store the interior points of the corresponding grid into $X_r = \{a_i + \delta, a_i + 2\delta, ..., b_i - \delta\}$
  Obtain $f'(x)$ for $X_r$: $f'(X_r) = \frac{f(X_r + \delta/2) - f(X_r - \delta/2)}{\delta}$
  Find the max and min of $f'(X_r)$; $f'_{\max}$,$f'_{\min}$
  % We have a root when $f(a_i)f(b_i) <= 0$ and may have two roots when $f'(a_i+\delta)f'(a_i-\delta) < 0$
  **if** $(f(a_i)f(b_i) <= 0$ or $f'(a_i + \delta)f'(a_i - \delta) < 0)$ **then**
    **root**=True
  **end if**
  **if** $f'_{\max}f'_{\min} < 0$ **then**
    $0 \in f'(X_r)$; we get two new intervals
    $N_1(X_i) = [-\infty, x_m - \max(\frac{f(x_m)}{f'_{\max}}, \frac{f(x_m)}{f'_{\min}})]$
    $N_2(X_i) = [x_m - \min(\frac{f(x_m)}{f'_{\max}}, \frac{f(x_m)}{f'_{\min}}), \infty]$
    $N(X_i) = \{N_1(X_i), N_2(X_i)\}$
  **else**
    $0 \notin f'(X_r)$; we get one new interval
    $N(X_i) = [x_m - \max(\frac{f(x_m)}{f'_{\max}}, \frac{f(x_m)}{f'_{\min}}), x_m - \min(\frac{f(x_m)}{f'_{\max}}, \frac{f(x_m)}{f'_{\min}})]$;
  **end if**
  % Find the intersection of the intervals and store them in the new list $H_l$
  $[H_l, n_l] = \text{intersection}(X_i, N(X_i))$
  % $n_l$ indicates the number of new intervals
  % Remove the old interval from the end of list $H$ and replace it with new ones
```

```
    $H\{\text{end}\} = \varnothing$
    for $i \in \{1, ..., n_l\}$ do
        $H\{\text{end} + 1\} = H_l\{i\}$
    end for
    if $n_l \neq 1$; there is zero or more than one new interval then
        No root is detected yet, root = False;
    else if width of $H_l\{1\} \leq \varepsilon$ and $f(\text{mean}(H_l\{1\}) \leq \varepsilon$ then
        % When there is one interval
        % When the width of the interval is smaller than the tolerance
        % When the function at the middle point is small enough
        if root = True then
            Add the midpoint of the interval $H_l.X$ to the end of $x$
        end if
        % Remove this interval; $H\{end\} = \varnothing$
        % This interval is eliminated, root = False
    else if $\text{abs}(x_m - \text{mean}(H_l\{1\})) < \varepsilon$ then
        % When there is one interval
        % When the width of the interval is NOT smaller than the tolerance
        % When the midpoint of the interval is changing less than the tolerance
        % Divide the interval in halves and add them to $H$
        $[a_j, b_j] = H_l\{1\}$
        $H\{\text{end}\} = [a_j, (a_j + b_j)/2]$
        $H\{\textbf{end} + 1\} = [(a_j + b_j)/2, b_j]$
        No root in this case is detected yet
    end if
end while
$x = \text{sort}(x)$
if The distance between two roots in $x$ is smaller than the tolerance then
    Keep only one of the similar roots in $x$
end if
Output: $x$
```